Chapter 4

Structure and Property Correlations of Lithium and Ionic Liquid Containing Silica-Gel Composites Prepared via Sol-Gel Process

4.1 Introduction*

Li^+ ion-based ionic solids have been widely investigated in view of their potential applications in batteries and other solid-state devices. These solids have been prepared in a wide variety of compositions, in crystalline as well as in amorphous states with moderate ionic transport near room temperature. Various attempts have been made to enhance the ionic conductivity of such systems [1]. Fast ion conductors typically have large number of mobile ions and relatively low activation energy. This is mainly due to their free volume and connected pathways with moderate energy barriers. Borso *et al.*, have studied a fast Li^+ ionic conductor system viz., Li_2S+SiS_2 glasses and explained the conductivity ($10^{-4}\ \Omega^{-1}cm^{-1}$ at room temperature) in terms of co-operative ion dynamics [2]. Adachi *et al.*, in a comparative study of fast Li^+ ion conducting ceramic electrolytes, report that enhanced conductivity of aluminum doped $LiTi_2(PO_4)_3$ is due to decrease in the activation energy at grain boundaries by high densification [3]. These systems have ionic conductivity (bulk) in the range of $10^{-4}\ \Omega^{-1}cm^{-1}$ at around 298 K.

Ionic liquids (ILs) are salts of cations (mostly organic) and anions with the melting point below or near room temperature and have received significant attention recently owing to their applications in solid/gel polymer electrolytes and ionogels. Particularly, imidazolium based ILs are interesting and a large number of electrochemical studies are available, due to their interesting properties such as high thermal stability, wide electrochemical stability window, low vapor pressure, non-volatility, wide liquidus range and good capability of dissolving materials [4-8]. ILs can be easily tuned, tailored and made task specific. These extraordinary physical and chemical properties of ILs are appealing to the electrochemists, and there are attempts to use these in some form, for example, as electrolytes, in advanced energy storage devices in order to improve the performance of the device [9-12]. Even though there are many advantages of the liquid nature of ILs, one of the major disadvantages is their suitability for electrochemical applications in solid-state devices.

** Part of this work is published in (i) Materials Research Express, 6 (2019) 105202 and (ii) Electrochimica Acta, 323 (2019) 134841.*

So, to overcome this fluidic problem of ILs, these have been confined into nano-pores of the solid matrices with improved electrochemical properties [13-16]. Immobilization of ILs in solid matrices provides more stability and makes them compatible for solid state device applications. Confinement of IL into different solid matrices has been attempted by many groups [17-21].

Of the many methods of immobilization of ILs in a solid network some of the popular techniques are i) *in-situ* introduction by sol-gel method, ii) soaking a previously prepared network in IL, and iii) "ship in bottle" method specific to zeolites/MOFs [13]. Sol-gel method helps in the confinement of IL and other additives within the oxide matrix through one-step, one-pot process [17, 18].

Using the silicate glass network as a basic framework there are several electrical transport studies in which varying quantities of ionic liquids and small ions such as Li^+ are added to the basic framework. We can classify these studies into three categories viz., where (i) only Li^+ ions are added [22, 23] or (ii) only pure ionic liquid is added [18-20] or (iii) both Li^+ ions and ionic liquids are added to the frame work [17, 21]. In this work we focus on IL and lithium salt confined silica-gels obtained through sol-gel process; in these systems, where high ionic conductivity can be achieved in the solid state due to the possibility of the host providing space for liquid electrolytes and small ions and consequently ionic transport taking place through connected pathways between the pores.

Rao *et al.* studied Li^+ ion transport in hydrolytic sol-gel derived lithium silicophosphate glasses and explored the ionic motion in the glassy matrix [22]. The conductivity for $10Li_2O$-$70SiO_2$-$20P_2O_5$ composition at 150 °C was reported to be ~10^{-7} $\Omega^{-1}cm^{-1}$. According to their study, P-Si-P-Si- forms a "noodle pipe" like structure through which the Li^+ ions are transferred via P-P centered bridges. Muralidharan *et al.*, have investigated lithium phosphoborosilicate glasses prepared by sol-gel method [23]. In this case, the samples were found to be conductive above 150 °C and exhibit a linear dependence with temperature. Sample with composition of $10Li_2O$-$9P_2O_5$-$16.2B_2O_3$-$64.8SiO_2$ was reported with a conductivity of ~10^{-8} $\Omega^{-1}cm^{-1}$ at 150 °C.

Néouze *et al.* reported for ionogels prepared through a non – aqueous sol-gel route, good thermal and mechanical stabilities and electrical conductivity of ~10^{-2} $\Omega^{-1}cm^{-1}$at 227 ^{o}C [18]. Later, the same group reported ionogels where the IL: host molar ratio was up to 1:1, and the IL is confined in the host matrix with good thermal and solvent stability with a conductivity value of ~10^{-3} $\Omega^{-1}cm^{-1}$ at room temperature similar to that of pure IL. These compositions do not have any small ions such as Li^{+}. This high ionic conductivity was attributed to interconnected porosity present in the ionogels. In another neutron scattering study the authors have indicated in IL confined matrices the dynamics of ions of IL slowed down compared to bulk IL [21].

Echelmeyer *et al.* attempted the confinement of IL: [BMIM] BF_4 (1-Butyl-3-methylimidazolium tetrafluoroborate), in lithium-silicate network by sol-gel process and explored its electrochemical properties; they have reported significant conductivity enhancement (~10^{-2} $\Omega^{-1}cm^{-1}$ at room temperature). In such matrices, dynamics of IL cation (here $[BMIM]^{+}$) is slowed down compared to bulk solution, and the presence of Li^{+} ion influences the ion dynamics [17]. Here contribution of IL in conduction is justified based on diffusion coefficient of cations and anions. However, different preparations of the same compositions gave different absolute values for ionic conductivity and diffusion coefficients. Dalvi and co-workers reported, on external dispersion of another IL – [BMIM] BF_4 on the Li_2SO_4-Li_2O-P_2O_5 glass matrix resulted in increase in conductivity. In these systems, the immobilization of ionic liquid happens in between the tiny glass grains followed by an enhancement in conductivity of ~2-6 orders of magnitude [24]. According to Karout and Pierre, ionic liquids act as condensation catalysts of silica in gel to glass condensation and as a moderator of the condensation rate due to limitation of the dissolved species by diffusion [25]. These materials are of much interest as electrolytes in smart materials and various battery applications [26-27].

We find in most of the cases the amorphous silicate network is obtained through aqueous or non-aqueous sol-gel route; mostly low temperature or room temperature conductivity is reported. We report here a set of novel silica-IL-Li salt-based systems which shows stable high temperature conductivity. With an idea that IL in small amounts can possibly be confined in the gel matrix more homogeneously in the form of narrow channels and will promote charge transfer without compromising the solid state of the system, the present

work is planned. Interesting properties are reported wherein we find the presence of the IL in the composite enhances the conductivity, however, the relation between the composition and conductivity is complex. Structural and applicative properties of the prepared composites have been discussed thoroughly. We have also modified the system in one or two cases by incorporating an additional component, PbO, and studied the effects on room temperature conductivity [28]. Incorporation of Pb^{+2} ions into the glass matrix by sol-gel process has been reported by others [29], and such composites did have thermal stability issues beyond a particular mol% value. The composites prepared with additional component Pb^{2+} showed good ionic conductivity at room temperature ~10^{-4} $\Omega^{-1}cm^{-1}$.

System 4A

[EMIM] BF_4 Confined Lithium Silicate Gel Composites Prepared by Hydrolytic Sol-Gel Process

4A.1 Composition

System 4A comprises of silica gel composites (xerogels) prepared through hydrolytic sol-gel process with confinement of ionic liquid (IL) [EMIM] BF_4, $LiNO_3$ and $CuCl_2$. This IL has been used due to its wider thermal stability window. The IL is liquid at room temperature (melting point 15 ^oC) and has a boiling point above 350 ^oC (may decompose). Two series of compositions have been prepared for present study viz., series-1 with increasing Li^+ concentration and series-2 with increasing IL concentration. Some other compositions as required for experimental comparison needs are also prepared (Details are in Table-4.1).

Table 4.1 – Composition, density (error limit ±0.05 gm cm^{-3}) and molar volume of the samples.

Sample Code	Composition (mol %)				Density (gm/cm^3)	Molar Volume (cm^3/mol)	
	$LiNO_3$	[EMIM] BF_4	$CuCl_2$	SiO_2	Experimental	Calculated*	Experimental
Series-1: Increasing $LiNO_3$ concentration							
L18	18.2	0	0.9	80.9	1.655	23.89	37.68
L18E	18.2	0.9	0.9	80	1.755	24.46	36.24
L26E	26.1	0.9	0.9	72.1	1.595	25.02	40.31
L33E	33.3	0.8	0.8	65.1	1.465	25.29	44.18
L40E	40	0.8	0.8	58.4	1.456	25.72	44.86
L46E	46.2	0.8	0.8	52.2	1.599	26.14	41.19
Series-2: Increasing IL concentration with $LiNO_3$ fixed at 18.2 mol%							
L18E2	18.2	1.8	0.9	79.1	1.683	25.13	38.53
L18E4	18.2	3.6	0.9	77.3	1.502	26.30	44.83
L18E7	18.2	7.3	0.9	73.6	1.341	28.86	54.01
Series-3: Increasing IL concentration with $LiNO_3$ fixed at 33.3 mol%							
L33E2	33.3	1.7	0.8	64.2	2.175	25.97	30.33
L33E3	33.3	3.3	0.8	62.6	1.836	27.06	37.14
L33E7	33.3	6.7	0.8	59.2	1.863	29.38	39.11
Series-4: Increasing IL concentration with no $LiNO_3$							
E4	0	4	1	95	1.689	25.52	39.28
E8	0	8	1	91	1.975	28.18	36.38

*Sample code has been used as abbreviation for the particular composition in the text. Superscript * denotes – 'based on the densities of the pure components for a compact mixture'*

A note on the fractional mol% values given in Table-4.1 is due. The samples were prepared initially assuming that, in the final product the precursor $LiNO_3$ will be converted to Li_2O. It is reported [30], the process of lithium incorporation in the glass network as modifier

takes place at a temperature that is dependent on the decomposition temperature of the precursor used. For those precursors of lithium where the anion is organic species such as citrate, this process happens at around 400 ^{o}C. For lithium nitrate, the decomposition process starts at 475 ^{o}C and ends at 650 ^{o}C [31]. In order to retain the IL in the system, this high-temperature step was not performed during the present work and hence most of the lithium along with nitrate may be present in the liquids at the pores of the solid. Therefore, lithium as lithium nitrate has been reported and the whole number integer values of mol% planned for Li_2O based compositions stand corrected. In addition, as these composites are not treated through the high temperature process the gel to glass transformation is not completed.

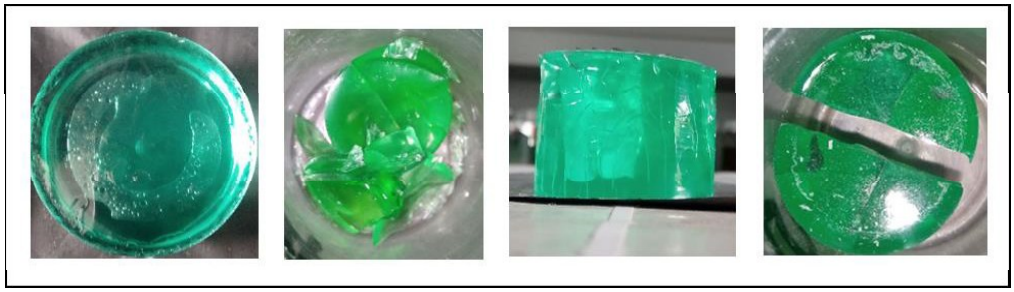

Fig. 4A.1 The photographic image at 1x magnification for densified gel obtained after room temperature drying the sol (before heating the composites).

Acid catalyzed hydrolysis of TEOS is done in an acidic medium (HCl at 0.01 equivalent of TEOS) using ethanol as a co-solvent (TEOS: H_2O: EtOH – 1: 4: 10) followed by condensation. After formation of homogeneous sol, $LiNO_3$, $CuCl_2$ and IL were added subsequently. Homogeneous sol obtained from the reaction mixture was kept at ambient conditions to obtain solidified gel (after stiffening of the network). Obtained gel was heat treated initially at 50 °C and further at 150 °C for 15-20 days to form the final composite. The prepared samples are stable at room temperature and are found to be water soluble, and samples having higher concentrations of lithium salt are also hygroscopic.

The IL selected for this work has been a component in many studies on similar systems as mentioned in the introduction. Literature findings show interesting conductivity [32] and electrochemical [33] studies in this regard. However, it is possible that the anion of the IL is partially hydrolyzed and HF and anions such as $[BF_{(4-x)}(OH)_x]^-$ may be present. It is reported at room temperature of 13.7% of BF_4^- ions are hydrolyzed in HBF_4 [34]. Since

the preparation and gel-forming times are not very long, it is assumed that this hydrolysis is minimized.

4A.2 Structural Studies

4A.2.1 Density and Molar Volume

At the outset, molar volume variation can be seen in this plot with a change in concentration of IL as well $LiNO_3$ (Fig. 4A.2). Molar volumes are higher than the calculated values indicating the expansion of the network during the amorphous composite formation. This may also mean that there is substantial void space in the material which can hold the solvents and the IL. As is evident from the plot, with the increase in IL concentration there is a gradual rise in the molar volume of the composites. However, any definite trend could not be observed with respect to the changes in $LiNO_3$ concentration.

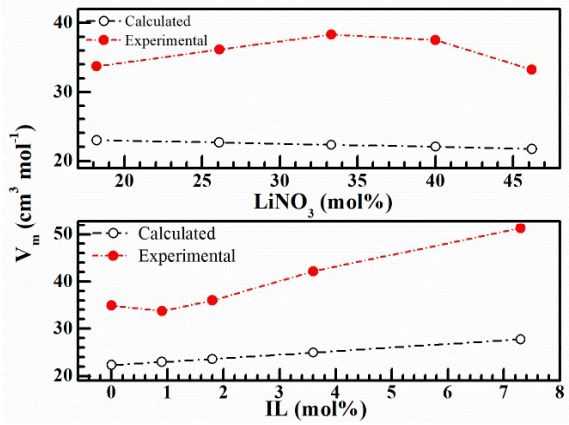

Fig. 4A.2 Molar Volume of the composites of series-1(a) and series-2(b).

4A.2.2 Powder X-ray Diffraction

Halo patterns (Fig. 4A.3 and Fig. 4A.4) as apparent for most of the samples confirm their amorphous nature in a wider range of compositions. The patterns corresponding to the variation of Li^+ ion concentration and variation of IL concentration are shown separately. The patterns also suggest in most of the cases that incorporation of IL does not lead to the formation of a new compound or crystallization of the gel. Hence, it is possible to incorporate IL homogeneously in these composites without disturbing the amorphous structure of the samples.

Powder X-ray diffraction results also suggest that it is possible to incorporate IL homogeneously in the composite in a wide range of composition, at least up to 4 mol%. Further, the addition of $CuCl_2$ and $LiNO_3$ into the matrix does not lead to any crystallization. However, for L18E7, PXRD is subtle but significant peaks at $2\theta = 38.63$, 44.87 and 65.51 are observed. Similar presence of tiny peaks is noticed for L33E3 and L33E7 as well. This may be due to the formation of some unknown phase at these concentrations.

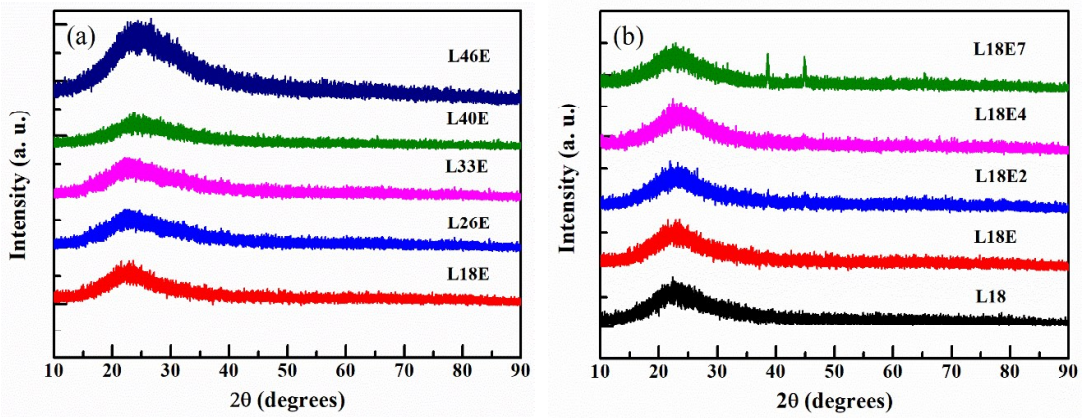

Fig.4A.3 PXRD patterns of the prepared samples (a) series-1 and (b) series-2.

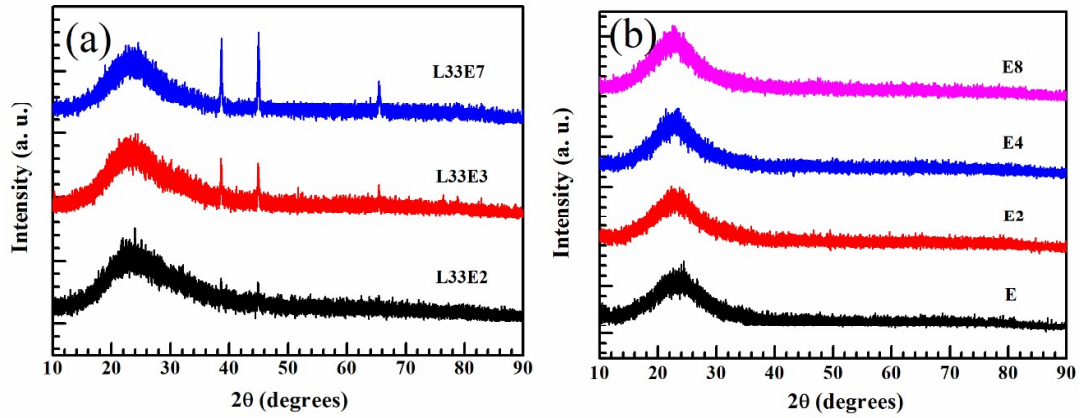

Fig.4A.4 PXRD pattern of the prepared samples (a) series-3 and (b) series-4.

4A.2.3 Electron Paramagnetic Resonance Spectroscopy

From the EPR spectra of the composites the following points may be concluded: (i) Cu^{2+} ion is in axial symmetry and not having any fast-dynamic movement as the spectrum is anisotropic and well separated hyperfine splitting are seen in parallel and perpendicular

regions. (ii) The spectral lines are broadened with increasing concentrations of both lithium ion and IL. Even though the cupric ion concentration is maintained the same in all these composites, when the sites available for cupric ion attachment are getting reduced these are forced to occupy the nearby sites thus increasing the dipolar broadening. (iii) In general, in magnetic resonance the resolution increases with increase in frequency of recording. However, it is a well-established that if the resonance parameters such as g , A are distributed (minor variation from site to site and the overall population following a probability distribution function) then, the inhomogeneous broadening arising due to this distribution will increase at higher frequency recording[35-37]. This happens mostly in amorphous systems. In our case also we find (Fig 4A.6a and 4A.6b) well resolved X-band (~9 GHz) spectrum and broadened Q-band (~32 GHz) spectrum for samples L18 and L18E (this has been found true for the other samples also). A computer simulation based on the model described in Chapter 2 gives the distribution parameters and shows cupric ion exists in a wide variety of mildly varying geometries. By inference we can extend the conclusion that lithium ion may also have distributed bonding parameters. (iv) We could record only the room temperature (RT) or lower temperature (LNT) EPR spectra of the samples. Thus, we cannot correlate this distribution to the high temperature conductivity variation with respect to composition in our samples.

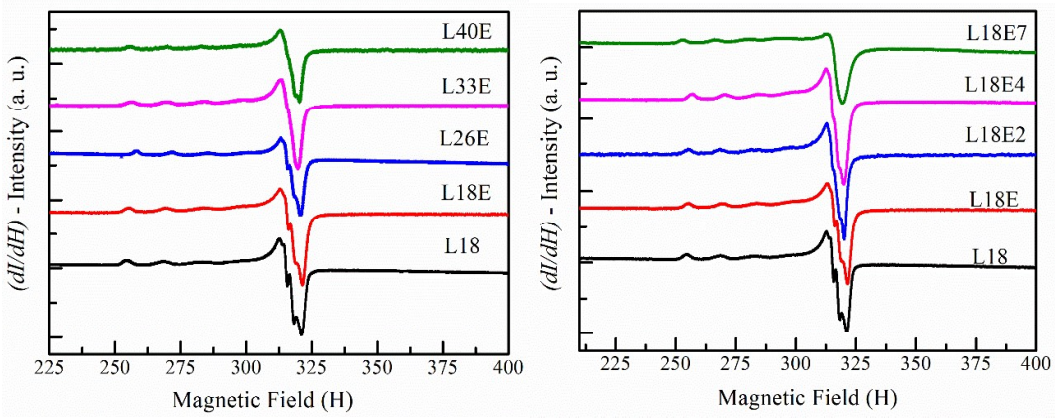

Fig. 4A.5 EPR: RT-X-band spectrum for (a) increasing $LiNO_3$ concentration, and (b) increasing IL concentration. Magnetic Field (H) values are in mT.

Fig 4A.6 (c) and (d) show the simulated X- and Q- band EPR spectra for the sample L18E; the spectra are simulated with the parameters:

$mean\ g_{\parallel} = 2.5000\ ; mean\ g_{\perp} = 2.0600;\ \sigma_{g_{\parallel}} = 0.0250; \sigma_{g_{\perp}} = 0.0060; correlation\ coefficient\ \rho\ between\ g_{\parallel}\ and\ g_{\perp} = 0.99;\ \ A_{\parallel} = 144\ G\ and\ A_{\perp} = 20\ G; no\ distribution\ of\ hyperfine\ parameters.$

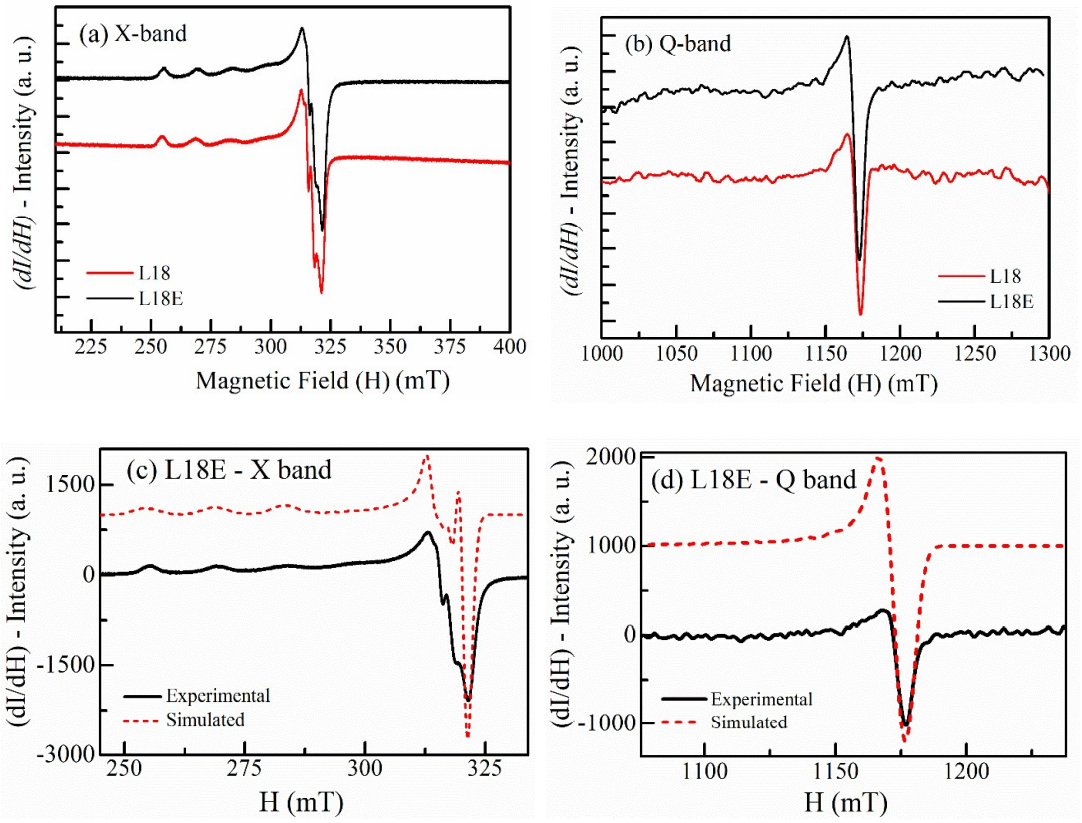

Fig. 4A.6 EPR: RT (a) X-band and (b) the corresponding Q-band spectrum for L18 and L18E composites; L18E (c) X-band (d) Q-band computer simulated spectra

The procedure of simulation is explained in Chapter 2. The same parameters are used in both the spectra and only the frequency and field values are changed to get the spectra. As expected, we see the hyperfine splitting resolution is lost in high frequency spectrum which is unusual in magnetic resonance spectra. The simulations match very well with the actual spectra and we find Cu(II) ion is having a variation in chemical binding with the $g_{\parallel}$ varying in the range 2.4071- 2.5929 and $g_{\perp}$in the range of 2.0377-2.0823 with perfect positive correlation between $g_{\parallel}\ and\ g_{\perp}$. These values indicate copper ion is present in a wide variety of geometries, from elongated octahedral and pseudo tetrahedral. The high values of $g_{\parallel}$ indicate mostly the preferred geometry is pseudo tetrahedral [36]. Copper ion may

be surrounded by chlorine or oxygen atoms and we can assume similar conditions will be there for the conducting ion lithium also.

4A.2.4 FTIR Spectroscopy

Fig. 4A.7 shows the FTIR spectra of the composite without IL recorded in ATR and transmission modes, respectively of the sample L18. Since this sample does not have IL, the absorptions seen in this case are only due to the silica network and water-ethanol mixture. Even though the sample has been treated at 150 ^{o}C only the unbound water and ethanol will be eliminated by this process. The physisorbed water/ethanol in the ultra porous gel structure and the chemisorbed water/ethanol at the surface of the composite will not be completely eliminated by this process; heat treatment beyond 400 ^{o}C is required to irreversibly eliminate the entire hydroxyl group-containing components and only beyond 800 ^{o}C, complete elimination of hydroxyl and ethoxy(-OC_2H_5) groups are expected [38]. Porous structures have been identified in such amorphous systems [39].

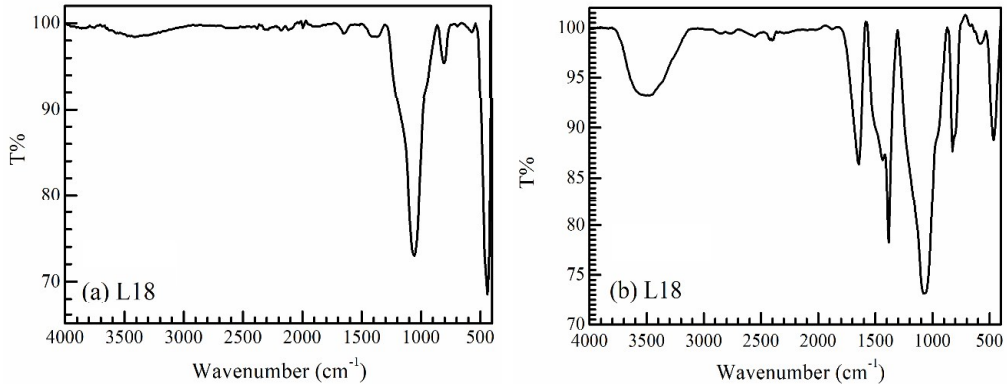

Fig. 4A.7 L18 FTIR in (a) ATR mode and (b) in Transmission mode.

The peaks corresponding to water, nitrate and ethanol emerging strongly in the transmission mode; Stretching vibration of hydrogen-bonded -OH (ν_{OH}) broad peak at 3500 cm^{-1}, bending vibrations of -CH_2-(δ_{CH2}) at 1400 cm^{-1} and bending vibrations of water (δ_{OH}) at 1600 cm^{-1}, indicating the major amount of water, ethanol mixture is present in the physisorbed form in the porous gel structure. The peak at 1400 cm^{-1} is also due to the antisymmetric stretching mode of the nitrate anion. Other absorptions are (identified as) 463 cm^{-1}(O-Si-O bending), 825 cm^{-1} (Si-O-Si symmetric stretching), and 1072 cm^{-1} broad peak with a shoulder at 1188 cm^{-1} (Si-O-Si asymmetric stretching). There are reports in

the literature where amorphous silica is prepared starting from water glass (sodium silicate) through a precipitation route in aqueous media [40]. The IR spectrum reported in such cases is similar to Fig. 4A.7b except for the CH_2 bending modes of ethanol (and/or the nitrate antisymmetric stretching) at 1400 cm^{-1} are missing.

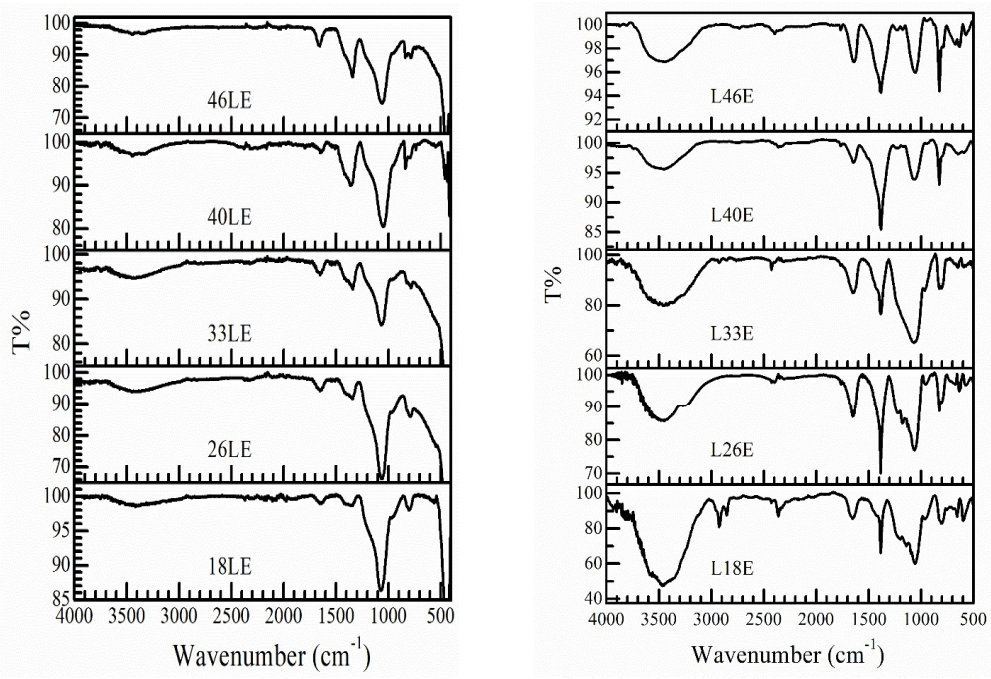

Fig. 4A.8 FTIR of the composites in (a) ATR mode (left) and (b) in Transmission mode (right).

Figs. 4A.8(a) and 4A.8(b) are the FTIR spectra of the composites with IL and varying composition of lithium ion, recorded in ATR and transmission modes respectively. These spectra are similar to that of the composites made without IL and no specific peak exclusively for the IL was identified. However, the presence of IL is confirmed by SEM-EDS low-temperature DSC and XPS experiments (vide infra).

For the IL ([EMIM] BF_4), some of the important absorptions expected are: 3161 and 3121 cm^{-1} (ring C-H stretching), weak 2984 -2970 cm^{-1} (antisymmetric stretching of $–CH_3$, -CH_2 and symmetric stretching of $–CH_2$), sharp peak 1576 cm^{-1} (ring C=C stretching vibrations), 1286 cm^{-1} (stretching of B-F) and 1172 cm^{-1} (stretching vibrations of N-Et and N-Me) [41]. We see around these regions we have other peaks also and the mol % of IL being low compared to silica, these peaks are possibly not observed. As mentioned earlier it is also possible that BF_4^- may get hydrolyzed partially and anions such as $[BF_3OH]^–$,

$[BF_2(OH)_2]^-$, $[BF(OH)_3]^-$, and $[B(OH)_4]^-$ may be present [34]. Such hydroxyl groups will also show stretching and bending vibrations.

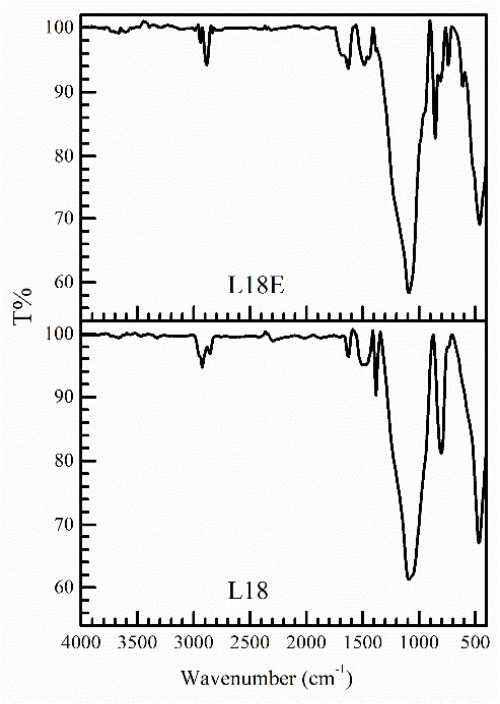

Fig. 4A.9 Transmission mode FTIR spectra after heat treatment at 500 °C for L18 and L18E.

In Fig. 4A.9, the transmission mode FTIR spectrum of both L18 and L18E samples, after heat treatment at 500 °C for 24 hours, are shown. As mentioned in literature [38] most of the water and ethanol components are removed from the system, however, some ethoxy (-OC_2H_5) groups are still sticking to the silica network as indicated by the –CH stretching (ν_{CH}) at 2900 cm^{-1} and –CH_2 bending (δ_{CH_2}) at 1400 cm^{-1}. The nitrates are also considerably reduced as seen by the reduction in the intensity at 1400 cm^{-1}.

In summary, within the range of temperature chosen for conductivity measurements, the water-ethanol mixture is present in the composites and that too more in ultra-porous inner cavities than on the surface. However, it is possible that after repeated cycles of conductivity measurements the ethanol component is reduced more compared to water.

4A.2.5 Field Emission Scanning Electron Microscopy

Morphology of the samples has been analyzed at 500 nm (for L18 and L18E) and at 300 nm (for L18E4 and L26E) scale to understand the effect of IL on the gel matrix (Fig.

4A.10). From the figures, it can be seen clearly that with the addition of IL into the solid matrix does not bring in any morphological changes. To confirm the presence of IL into the matrix, elemental mapping of these composites has been done.

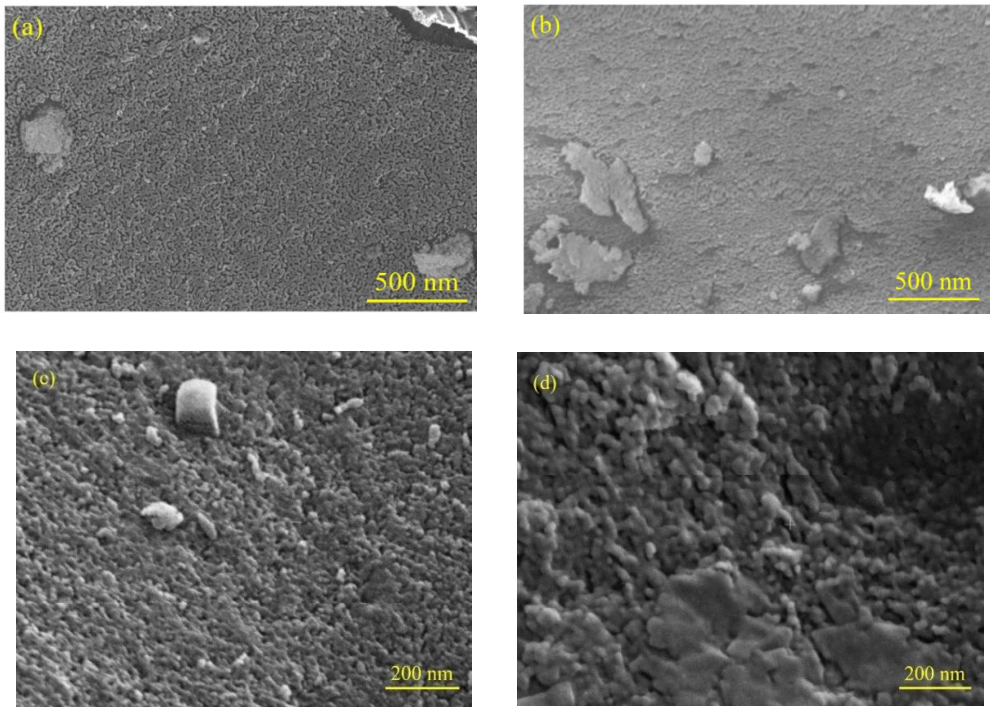

Fig. 4A.10 FESEM images of (a) L18, (b) L18E, (c) L18E4 and (d) L26E samples.

EDS mapping of these composites shows that the elements corresponding to IL (B and F) are evenly distributed throughout the matrix (Fig. 4A.11 – 4A.13 (before and after high temperature conductivity measurements)).

Fig. 4A.11 EDS mapping over FESEM image for L18E composite.

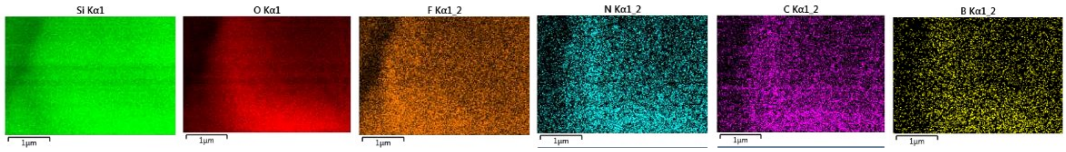

Fig. 4A.12 EDS mapping of L18E Composite for various elements (a-f Left to Right- Si, O, F, N, C, and B)

EDS mapping of the sample has also been recorded after performing 3-4 conductivity measurement cycles and these samples exhibit the presence of IL's elements into the matrix (Figs. 4A.13 and 4A.14). Thus, it is concluded that on heating these samples up to 350 ^{o}C, IL remains intact in these composites.

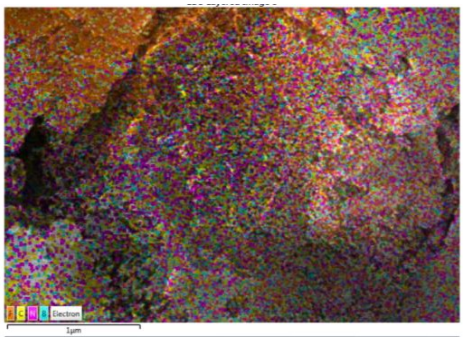

Fig. 4A.13 EDS mapping over FESEM image of L18E composite after conductivity.

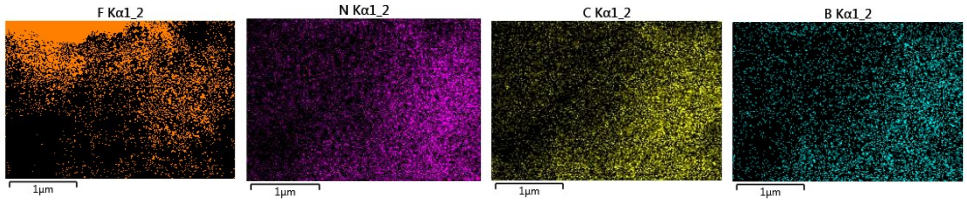

Fig. 4A.14 EDS mapping of L18E Composite after conductivity (a-d Left to Right-F, N, C, and B)

Morphology of the samples has been analyzed at 300-200 nm scales to understand the effect of IL on the gel matrix. In FESEM images of a sample without IL (L18), small grains of ~ 30-80 nm sizes are clearly visible (Fig. 4A.15a). At this nm level size of the grains has been determined randomly through the inbuilt software at the time of SEM analysis. Size of several different sized particles has been determined and then an average size of these particles has been reported. These grains are agglomerated in some regions of the gel matrix. On the other hand, IL containing sample (Fig. 4A.15b - L18E) shows growth of smaller grains and the sample is more homogeneous and uniform with connected grains.

It can be inferred that (i) the distribution of IL in the matrix is uniform and (ii) its presence facilitates new structural changes.

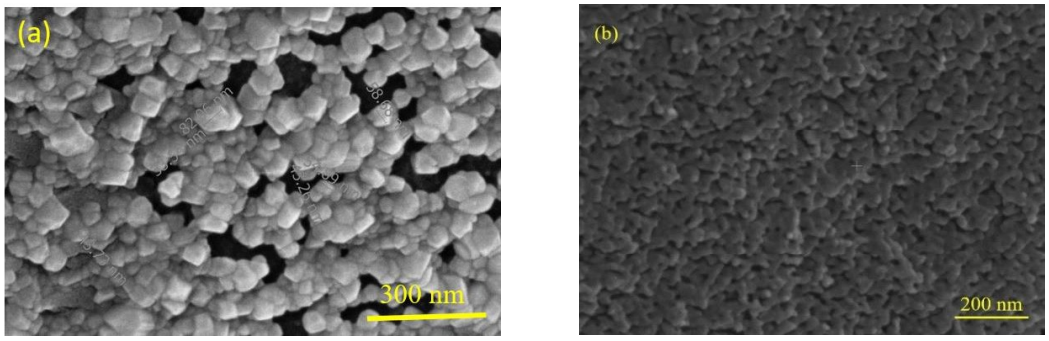

Fig. 4A.15 FE-SEM images of (a) L18, (b) L18E at 300nm and 200nm scale, respectively.

To understand the thermal stability of these solid substances, a sample (L26E) has been exposed to a fast heating process monitored by SEM (Fig. 4A.16). The melting of the entire sample starts around 990 °C and below this temperature, the overall solid-state structure of this sample is stable.

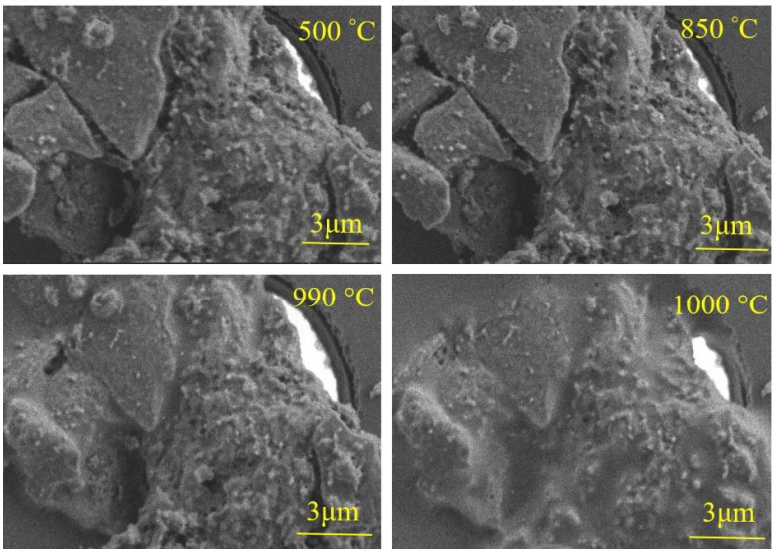

Fig. 4A.16 SEM pictures of a sample (L26E) at different temperatures.

4A.3 Thermal Analysis

4A.3.1 Differential Thermal Analysis (DTA)

DTA scans of the samples were taken in the temperature range of 35 to 500 °C with a heating rate of 10 °C/minute (Fig. 4A.17) in nitrogen atmosphere. As explained in the

FTIR section in such amorphous silicate systems prepared through sol-gel route, the water is adsorbed in two forms; physisorbed on the ultra-porous gel structure and chemisorbed at the surface.

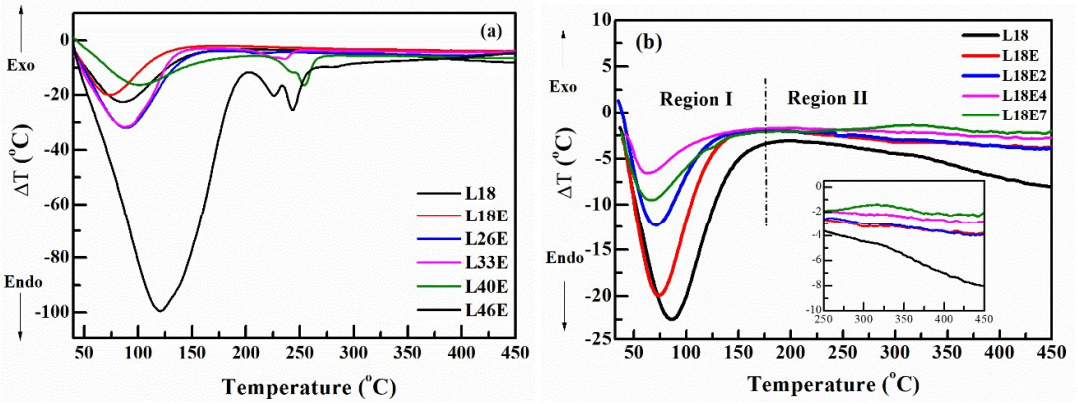

Fig. 4A.17 DTA scan of the prepared composites (a) increasing $LiNO_3$ concentration (Series-1) and (b) increasing IL concentration (Series-2). Inset: An exothermic peak corresponding to the boiling point of IL is evident (Clearly for higher IL containing (L18E7) composites).

The DTA scan is broadly divided into two regions. Region-I corresponds to the first endothermic dip in the temperature range of 75 to 170 °C that relates to the loss of adsorbed ethanol and water from the system. At about 170 °C the physisorbed water is eliminated and also part of the chemisorbed surface water gets eliminated due to silanol condensation. This process is completely reversible up to about 400 °C [38]. The endothermic dip shows its minimum ~78 °C (Fig. 4A.17), corresponding to the boiling point of ethanol and is associated to the loss of ethanol along with water from capillaries or from the surface of the composite. There are a few cases where Li concentration is high, an endothermic peak around 250 °C corresponding to the melting of $LiNO_3$ appears (in Fig. 4A.17a for L33E-L46E) indicating the presence of dried up $LiNO_3$ in the pores of the composite. If $LiNO_3$ is present on the surface or elsewhere in solid form, then crystalline peaks are expected in PXRD recordings, which are not observed. It has also been observed that as the concentration of IL increases, the endothermic peak position moves towards the boiling point of ethanol indicating IL facilitates ethanol confinement more than water (Fig. 4A.17b).

Many groups have performed differential scanning calorimetry on sol-gel derived lithium silicophosphate glasses [22] and lithium phosphoborosilicate glasses [23] to validate that water loss occurs around 100 °C and it was suggested that this loss is from sample surface

or gel capillaries. Since our preparatory procedure involves more ethanol in forming the gel, the solvent elimination starts around ethanol boiling point and continues up to 150 °C where both ethanol and water are eliminated; however, the surface water is very slowly eliminated up to 400 °C.

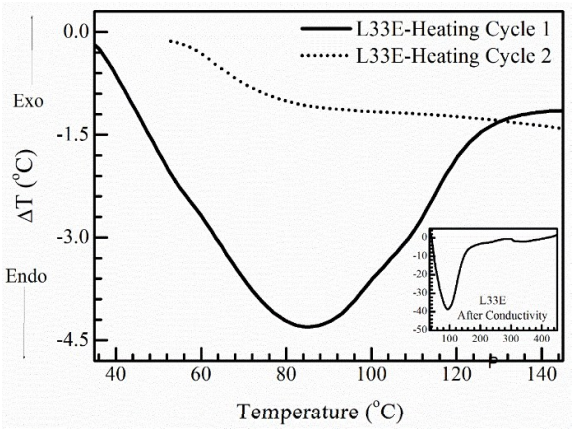

Fig. 4A.18 DTA Plots of L33E normal run and repetition after cooling without much time gap. Inset: DTA plot of L33E sample after three consecutive cycles of conductivity measurements and after ~1 year (inset with same coordinates).

In order to check the re-absorption of atmospheric water in place of ethanol after the heating-cooling cycle an immediate rescan of DTA is done which shows that water re-absorption is not immediate (Fig. 4A.18). The scanning in these cases was done only up to 150 °C. Further recordings after an elapsed period show re-absorption of water in the samples. Thus, the samples after high-temperature measurements left over a period of time may have more water than ethanol. Inset of Fig. 4A.18 shows after a sufficiently long time (~1 year), for the sample L33E the endothermic dip has moved towards 100 °C.

As it can be seen from the DTA scans that in the region II – in range of 150 – 450 °C (Fig. 4A.17a and 4A.17b) the samples have good thermal stability. The electrical transport measurements are reported for a major portion in this range.

If these systems are considered as glasses, the question of the glass transition temperature arises. The glass transition temperature of pure silica glass is around 1100 °C [42]. For the alkali metal silicate glasses the glass transition temperature is around 450 °C and with more Si content higher transition temperatures are observed [43]. For systems similar to the present system, in some reports [44] a glass transition temperature is identified below 0 °C

(around -70 °C) and these are considered to be the glass transition of the ionic liquids confined to the nanopores of the silicate network and not the glass transition of the entire network. We have also identified such glass transition temperature of IL and this result is presented in a later section as the evidence for the presence of IL in our systems. The present work focuses on thermal studies in the temperature range of RT - 450 °C corresponding to a temperature range in which the electrical conductivity measurements were undertaken. Thus, with an interest in understanding conductivity structure correlation, this temperature range was decided. It has also been reported previously [22-23, 45], that in sol-gel derived silica as well as in borate glasses there is less possibility of apparent crystallization and glass transitions. These thermal events do exist but difficult to identify. Therefore, the present amorphous systems can also be considered as amorphous gel/glassy in nature. However, the adsorbed hydroxyl groups will be eliminated only by a heat treatment above 800 °C to produce the glass which resembles the silicate glass prepared by melt-quench method. Since this step is not executed in the sample preparation, we prefer to call the prepared composites as gels. Pure silicate glasses as well as our samples treated at high temperature will not show the electrolytic properties reported here.

4A.3.2 Thermogravimetric Analysis (TGA)

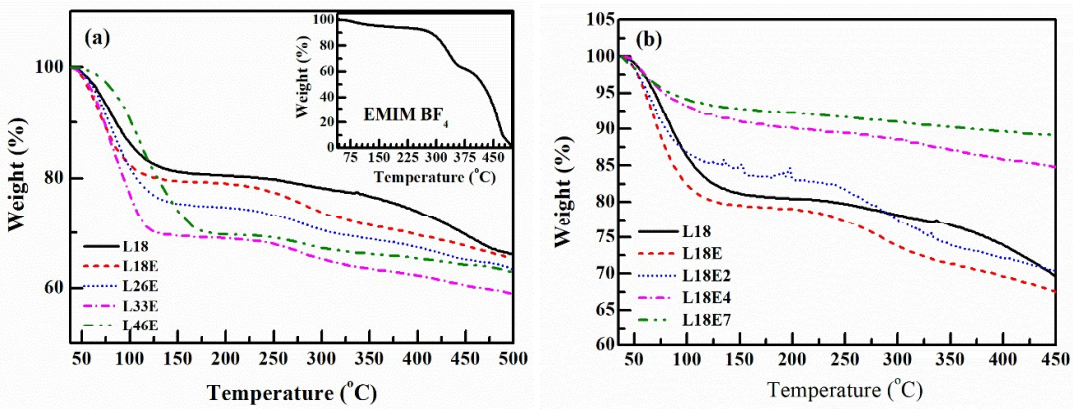

Fig. 4A.19 TGA scan of the prepared composites (a) increasing $LiNO_3$ concentration (Series-1) and (b) increasing IL concentration (Series-2). Inset: TGA profile for neat IL.

TGA scans (Fig. 4A.19) were obtained for the prepared IL-composite samples as well as the pristine ionic liquid. The weight loss of up to 30% in the temperature range 75 to 170 °C corresponds to the elimination of solvents from surface and inner pores as explained in

the DTA section. This loss in weight % cannot be correlated to any starting material, and is purely due to the solvent adsorbed, and the amount of solvent adsorbed is unknown.

As is evident from the inset of Fig. 4A.19(a), pure IL is stable at least up to 250 °C beyond which it starts evaporating followed by decomposition. By comparison of the curves of L18 (the sample without any IL) and L18E (the sample which has 1 mol% of IL) we note that the final weight loss at around 475 °C is same for the both compositions. Thus, the weight loss is not due to IL evaporation. This loss is due to the continuous solvent elimination from the pores of the sample. However, in case of samples having IL the solvent removal is faster at 300 °C and then slows down. Even though in the pure IL from 250 to 475 °C thermal events of evaporation and decomposition lead to weight loss the IL confined in the composite does not follow the same pattern. SEM-EDS results prove (*vide infra*) the presence of IL even after high temperature conductivity measurements.

Similar to DTA, TGA plots of the composites with a high concentration of IL or $LiNO_3$ also showed their thermal stability in the wide temperature range (150 - 450 °C). For composites with 18 mol% $LiNO_3$ and variable IL concentration (Fig. 4A.19(b)), the weight loss seen up to ~350 °C can be explained as due to the continuous solvent elimination from the pores of the sample, and the IL remains intact in the gel matrix. Based on DTA and TGA results the stable region of 150 - 350 °C has been chosen for the electrical conductivity studies.

4A.4 Electrical Transport

4A.4.1 Impedance Spectroscopy

Temperature and frequency dependence of electrical transport was thoroughly investigated using impedance spectroscopy, dc polarization, and ionic mobility measurements. Firstly let us focus our attention on the Nyquist plots. Nyquist plots (42Hz -5MHz) in blocking electrode configuration for these samples are shown in Fig. 4A.20 and 4A.21. As apparent in Fig. 4A.20a and 4A.20b, the samples with 18 mol% of $LiNO_3$ with no IL show depressed semicircles.

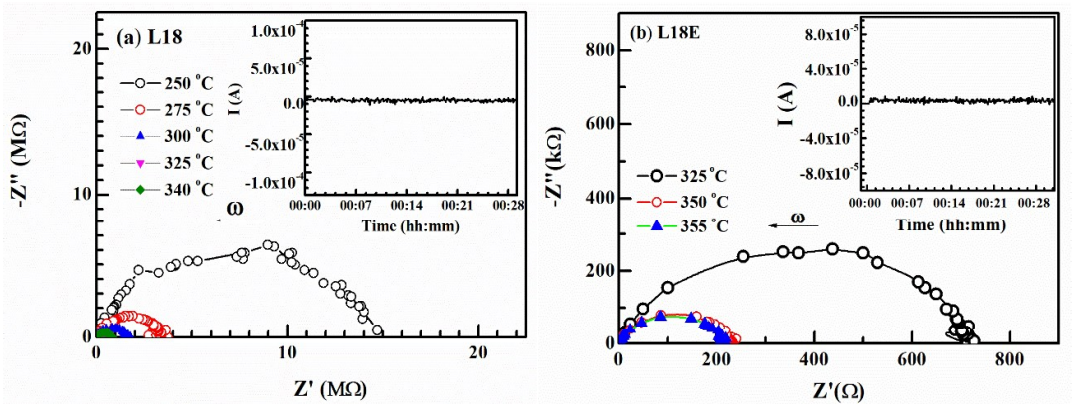

Fig. 4A.20 Nyquist plots for best-conducting samples (a) L18 and (b) L18E. Inset in both shows time dependence of the dc-current. For comparison, dimensions of the samples were kept almost the same.

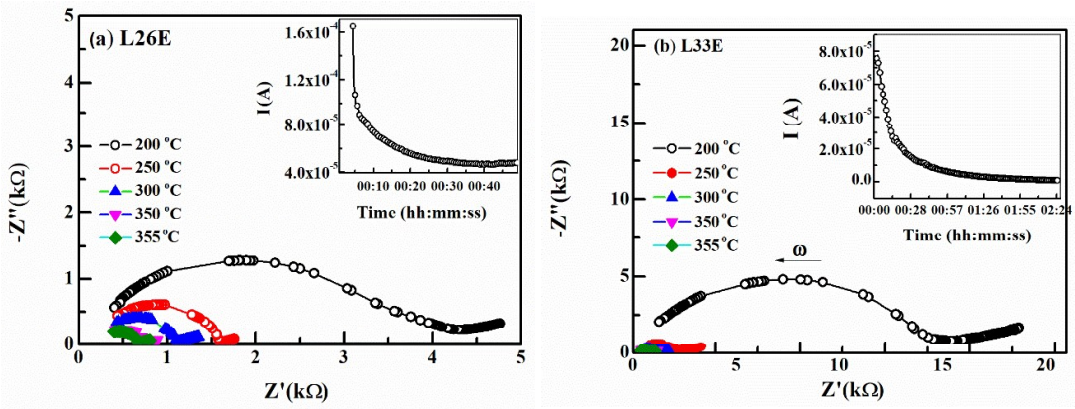

Fig. 4A.21 Nyquist plots for best conducting samples with increasing salt content. Inset of both figures shows the time dependence of dc-current.

No tail/spur is evident at low frequencies that further suggests electronic contribution. When IL in a small amount (1 mol%) is added, there is no apparent change in the nature of Nyquist plot. At low frequencies, there is no evidence of polarization event and this may suggest that electronic contribution dominates in electrical transport. To confirm the same, dc polarization technique is used where the dc voltage of 1V is applied across the sample and time dependence of the transient current is measured. The behavior of dc current for these samples is shown in the inset of Fig. 4A.20a and 4A.20b. It exhibits almost a constant voltage and current with time (Recorded at 250 ^{o}C). This, in turn, suggests no significant ionic contribution to conductivity. These results are consistent with the Nyquist plot and suggest that there is significant electronic transport in these two samples. However, the

increase of conductivity with temperature certainly suggests non-metallic behavior of the composites as well.

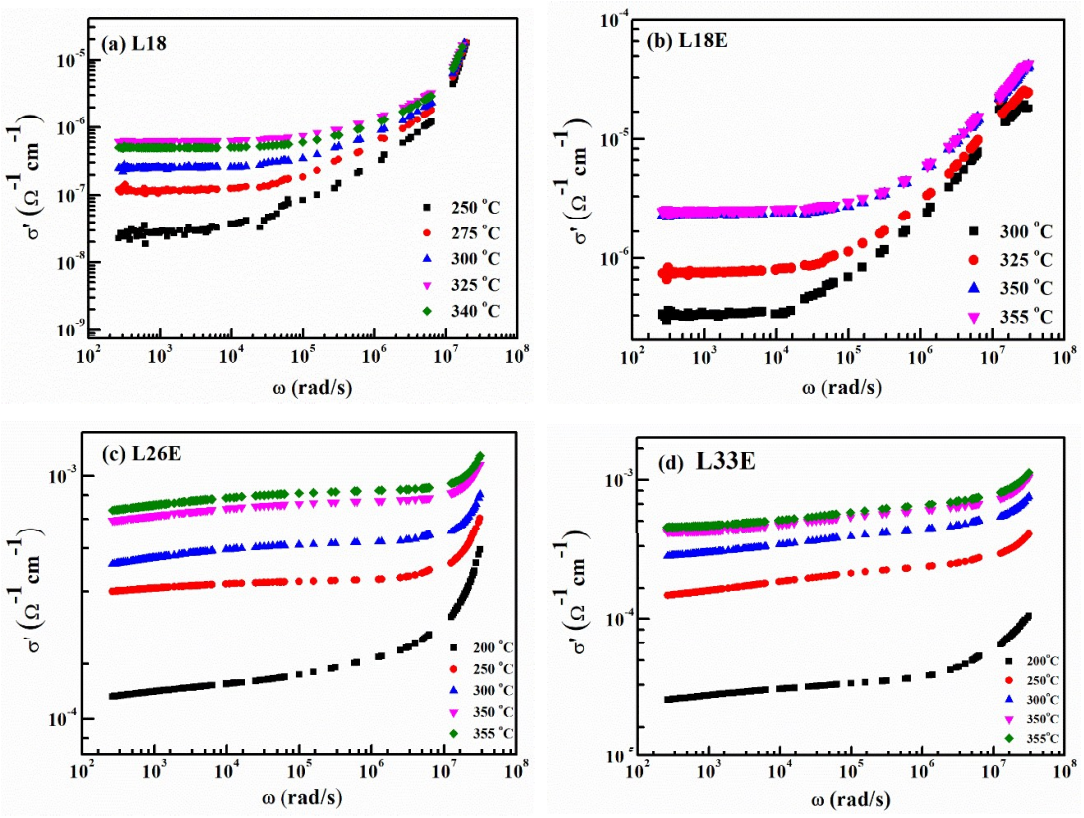

Fig. 4A.22 Electrical conductivity (σ′) as a function of frequency (ω) from 200 – 300 °C (a) L18, (b) L18E, (c) L26E and (d) L33E .

Addition of IL into the system does not change the basic nature of conductivity. Henceforth, it may be suggested that there is no contribution of IL cations and anions in the conduction process. To further understand the conductivity, IL is fixed to 1 mol% and salt content is increased in the samples. A significant change is observed in the nature of Nyquist plots. Fig. 4A.21, shows these plots for 1% IL and subsequently increase in salt concentration (26 mol% (L26E) and 33 mol% (L33E)). In these cases, a depressed semi-circle is observed followed by the apparent inclined line at a lower frequency. The spur at low frequencies suggests polarization of ions at the interface and therefore is the first-hand evidence of initiation of ionic transport with salt addition. As shown in the inset Fig. 4A.21a and 4A.21b, unlike low salt samples (L18)/ IL sample (L18E), the dc-current behavior is not constant with time. Interestingly, the transient current shows a notable fall

initially followed by saturation subsequently, that compliments the polarization effect due to ionic transport. When the salt content has increased this behavior is more significantly seen, that suggest the increasing ionic nature of the samples. Therefore, it may be suggested that the IL confinement leads to the formation of pathways for the Li^+ ions and with an increase in salt content, these pathways are significantly used by the mobile ions.

Besides, the IL incorporated samples showed good stability in 150 to 300 °C. Electrical conductivity measurements have been carried out in this region, essentially to understand the role of confined IL in electrical transport. At the outset, the electrical conductivity (σ′) is plotted as a function of frequency for different samples (Fig. 4A.22). Apparently, conductivity exhibits a plateau in a wide frequency range followed by dispersion in the high frequency region. From the plateau region, the dc conductivity (σ_{dc}) was obtained.

4A.4.2 Temperature Dependance of Conductivity

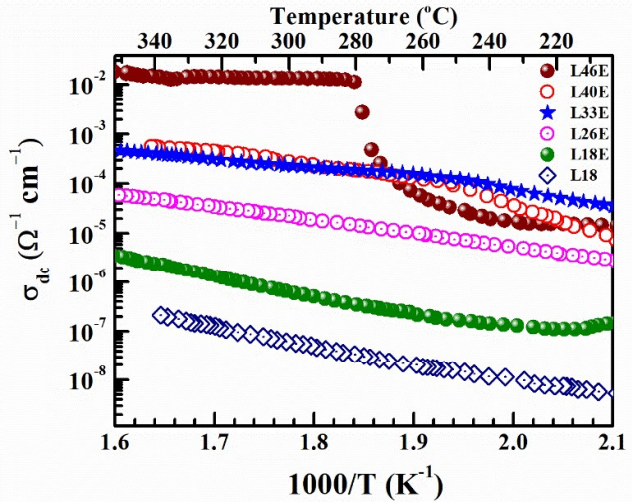

Fig. 4A.23 σ_{dc}–T cycle for composites with increasing $LiNO_3$ concentration (Series 1).

Fig. 4A.23 and Fig. 4A.24 shows the temperature dependence of σ_{dc} with variation in compositions. As apparent, σ-T cycle for the sample with 0% IL (L18) shows a linear rise. Interestingly incorporation of a small amount of IL (1 mol%) in the sample (for L18E), increases the conductivity significantly. In IL confined samples if Li^+ content is further increased; the conductivity further shows a notable rise (Fig. 4A.23). Thus, the L26E composite exhibits conductivity, which is more than four orders of magnitude higher than that of the 0% IL sample. It is evident that 1 mol% of IL is sufficient enough to promote

ion conduction in the system by at least an order of magnitude. Some experimental findings other than our work have also confirmed that IL incorporation in glass enhances the ionic transport [46-48]. The case of L46E is special. Initially the conductivity is low compared to other composites such as L33E and it increases from 260 ^{o}C to show highest conductivity among all samples. Due to time constraints we could not examine the structural changes in the range of 260-280 ^{o}C. We do find in DTA additional endothermic peak below 250 ^{o}C for L33E, L40E and L46E corresponding to $LiNO_3$ melting. However, the conductivity trends of L33E and L40E are same as other composites while L40E is different. Further studies are required here.

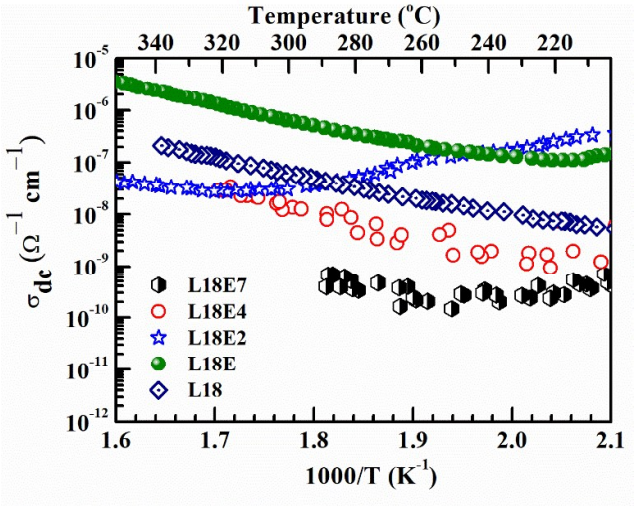

Fig. 4A.24 σ_{dc}–T cycle for composites with increasing IL concentration (Series 2).

The effect of increasing IL content in the composite and its influence on conductivity was also determined by keeping lithium salt concentration constant to 18 mol% (See Table 4.2, samples: L18E2, L18E3, L18E7). A huge decrease in conductivity of the composites with further 2, 4, and 7 mol% IL substitution in IL content was observed (Fig. 4A.24). The decrease in conductivity in cases of high IL content may be due to the possibility of Li^+ ions forming a complex with IL anion. Same is also reported for IL based electrolytes [49]. Such complex formation may lead to decrease in mobile Li^+ ion concentration responsible for electrical conductivity. This however needs further investigations. The chemical binding of the IL with the wall (the silica surfaces inside the pores) as well lithium ions are studied and reported by other groups. These studies are both computational (DFT based calculations) and experimental. The interaction between ionic liquid and the silica surface

happens through a bond between one of the imidazolium ring hydrogen and the oxygen atom of Si-O bond [44]. In another study [50] it is found that the interaction of the ionic liquid and the lithium ion is through the anion. Lithium ion is four-coordinated with four BF_4^- anions. At higher concentration of lithium ion, lithium ion clusters are formed. Lithium ion has the highest ionic conductivity in [EMIM]BF_4 compared to many other ionic liquids mentioned in that study.

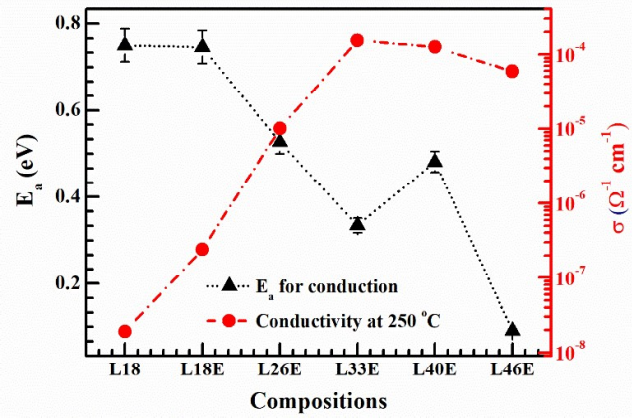

Fig. 4A.25 Variations of conductivity and activation energy with composition for series 1.

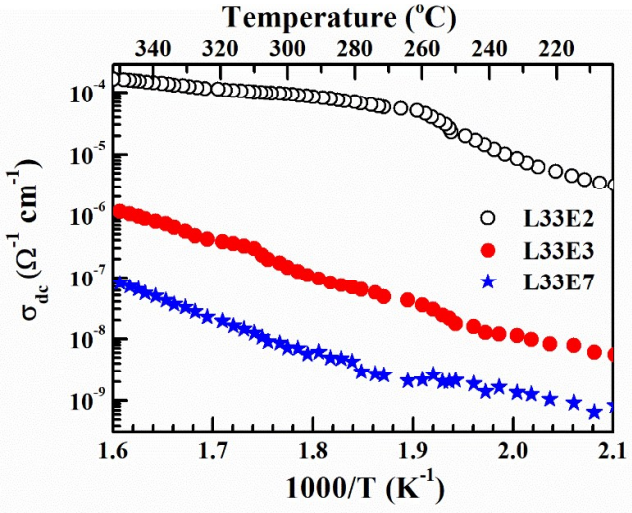

Fig. 4A.26 σ_{dc}–T cycle for Series-3 composites. IL variation leads to a significant fall in conductivity.

Correlation between activation energy and conductivity for the $LiNO_3$ increasing composites with constant 1 mol% IL concentration has been plotted in Fig. 4A.25. From the plot, it is evident, that incorporation of IL into the system results into a slight decrease

in activation energy required by the ions for conduction. The observation that the L18 sample exhibits almost comparable activation energy to that of L18E sample, may be attributed to (i) poor thermally activated behavior for ionic motion, or (ii) predominant electronic nature of both samples as revealed by Nyquist plots and dc polarization.

Fig. 4A.26 shows the temperature-dependent conductivity phenomenon on series-3 to further understand the contribution of IL in the conduction process. Compositions with fixed Li^+ content (33 mol%) with subsequent increase in IL concentration (2, 3 and 7 mol%) has been analyzed. The decrease in conductivity with increasing IL content for the gel composites can be clearly seen from the σ-T plots. A steep rise in conductivity of L33E2 composite can be noticed, that could be due to well-populated conduction channels which facilitate ion transfer. As explained above, with an increase in the concentration of IL again the possibility of Li^+ ions forming a complex with IL anion increases and consequently a decrease in the conductivity of the gel composites is observed.

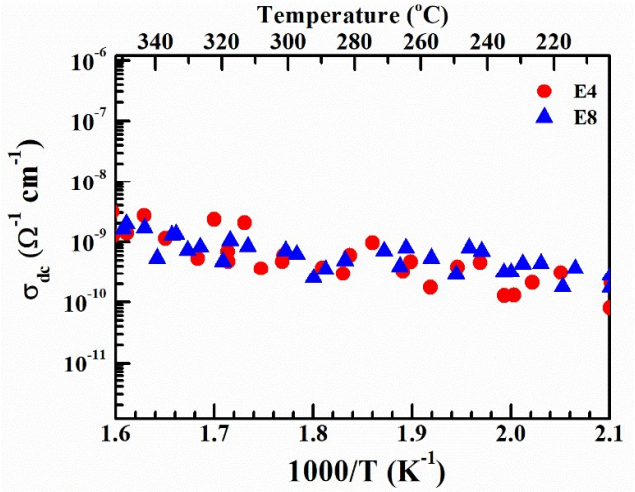

Fig. 4A.27 σ_{dc}–T cycle for Series 4 composites.

Alternatively, for only IL bearing composites (series-4), no significant rise/change in conductivity has been noticed (Fig. 4A.27) and these composites remain poorly conducting in nature. These results help in concluding that IL in itself hardly plays any role in ion transfer/conduction process. It only/majorly helps in creating the conduction pathways through which ion transfer is facilitated. Absence of Li^+ ions in these composites and their low conductivity in the measured temperature range helps in verifying the concept.

Table 4.2: For various series of samples (i) Electrical conductivity at two different temperatures and (ii) The open-circuit voltage (OCV) of the Li/$LiCoO_2$ cells fabricated using samples as an electrolyte.

Sample Code	Conductivity at 523K (Ω^{-1} cm^{-1})	Activation Energy (eV)	Conductivity at 548 K (Ω^{-1} cm^{-1})	OCV (V)
Series-1				
L18	$1.9x10^{-08}$	0.75	$4.1x10^{-08}$	2.98
L18E	$2.3x10^{-07}$	0.74	$4.6x10^{-07}$	3.05
L26E	$1.0x10^{-05}$	0.53	$1.7x10^{-05}$	3.05
L33E	$1.5\ x10^{-04}$	0.33	$2.1x10^{-04}$	2.99
L40E	$2.0x10^{-04}$	0.48	$2.1x10^{-04}$	2.91
L46E	$6.5x10^{-05}$	0.09	0.013	3.10
Series-2				
L18E	$2.3x10^{-07}$	0.74	$4.6x10^{-07}$	3.05
L18E2	$9.9x10^{-08}$	0.46	$3.9x10^{-08}$	2.66
L18E4	$2.9x10^{-09}$	0.65	$9.6x10^{-09}$	2.44
L18E7	$2.6x10^{-10}$	0.48	$5.4x10^{-10}$	1.35
Series-3				
L33E2	$5.3x10^{-05}$	0.33	$8.2x10^{-05}$	3.17
L33E3	$3.9x10^{-08}$	1.05	$8.7x10^{-08}$	3.03
L33E7	$2.3x10^{-09}$	1.06	$5.1x10^{-09}$	2.96
Series-4				
E4	$2.8x10^{-10}$	0.33	$3.9x10^{-10}$	0.07
E8	$2.1x10^{-09}$	0.41	$3.9x10^{-10}$	0.00

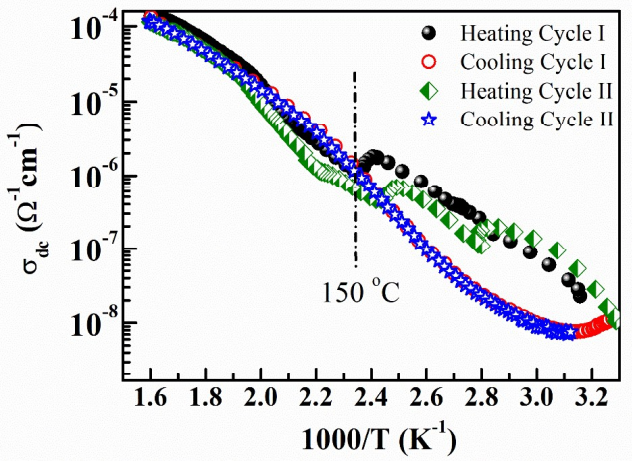

Fig. 4A.28 L33E sample repetitive conductivity cycles in both heating and cooling pathways (30 °C to 300 °C).

Another important observation is, conductivity at low-temperature range does not show stable values. Conductivity vs. temperature plot expanded at the low-temperature range is shown in Fig. 4A.28. While heating the sample from the lowest to the highest temperature, in the low-temperature region there is a kink in σ-T value at ambient temperature and subsequent fall in the conductivity values. This has been explained by Muralidharan et. al. [23], as arising due to the protonic conductivity of ethanol-water mixture along with that of Li^+ ion conduction. As the temperature is raised further the conductivity decreases as the ethanol-water mixture is evaporating. In the cooling cycle in this region conductivity is low as substantial portion of the water-ethanol mixture is out of the system. After allowing to exposure in an open atmosphere for some time slowly it picks up water molecules and ethanol concentration decreases. Again, while heating we find the same trend of higher conductivity due to the reversible nature of dehydration [38].

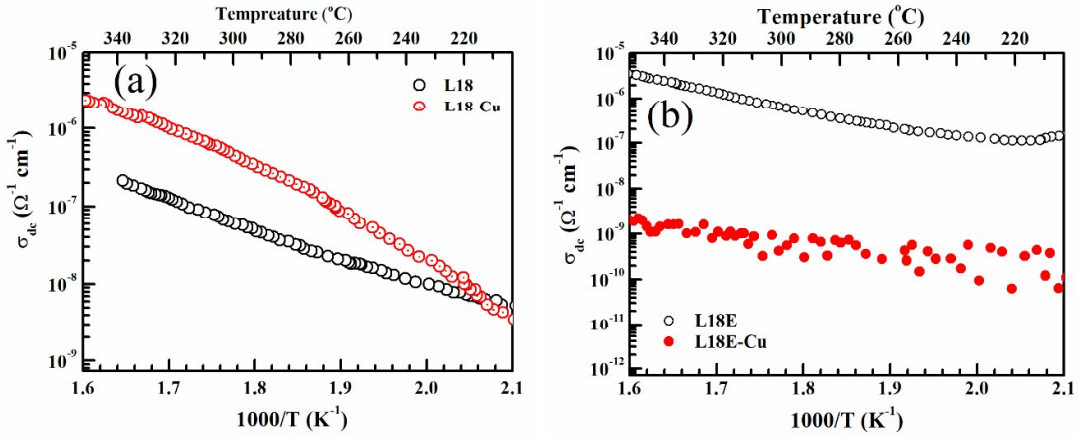

Fig. 4A.29 σ–T cycle for (left) L18 and (right) L18E composites without copper L18-Cu and L18E-Cu.

As it has been explained before that, Cu^{2+} ion has been added into these silica gel systems with the aim of understanding the microenvironment in terms of EPR Spectroscopy. We also notice, in preliminary findings that there is a difference in conductivity of the composites when prepared without copper. For L18 and L18E composite when prepared without copper (labeled as L18-Cu, and L18E-Cu), the changes in conductivity are shown in Fig. 4A.29. From the σ-T cycles of L18 and L18-Cu, a marginal variation in conductivity can be observed at high temperature (at 250 °C, both show similar conductivity of 10^{-8} Ω^{-1} cm^{-1}). On the other hand, the presence of Copper in L18E composites shows a remarkable increase in conductivity by ~3 orders of magnitude when compared with the sample

prepared without copper (L18E-Cu). The role of cupric ion in conductivity has to be explored further in future.

4A.4.3 DC polarization and Ionic Mobility

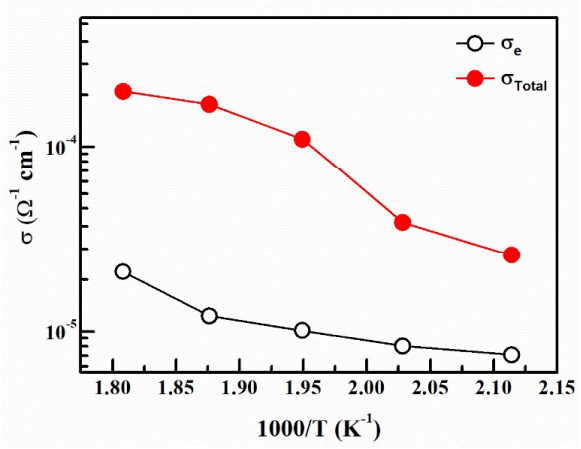

Fig. 4A.30 Temperature dependence of electronic conductivity and total conductivity for L33E composite. Total conductivity is the dc conductivity (also reported in Fig. 4A.23) as measured using impedance spectroscopy.

The significant conductivity enhancement was further examined by using various techniques, so that the electronic contribution to total electrical transport can be evaluated. The transient current was measured as a function of time. The current was allowed to saturate at every temperature for almost one hour. The conductivity corresponding to the saturated current was considered as electronic conductivity, whereas, the total conductivity points were taken from σ_{dc}-T cycles on pristine samples. Electronic conductivity (σ_e) thus investigated separately is shown in Fig. 4A.30 for L33E sample. From the plot, it is apparent that the electronic conductivity also increases with temperature. However, its value is found to be smaller at least by ~2 orders of magnitude than the total conductivity. This, in turn, suggests that sample L33E is predominantly ionic in nature. For all the samples the conductivity experiments were conducted in a temperature range starting from RT to 350 ^{o}C. These were repeated three or four times for each sample. We do not find any change in the high temperature conductivity values in these repeat experiments. However, when we cross the limit of 350 ^{o}C and go even up to 375 ^{o}C, the repetition experiments show lower conductivity values than that has been observed earlier. As we have stated

earlier the IL's confinement in the sample is assured only up to 350 ^{o}C and further increasing temperature will eliminate IL from the sample.

Further ionic mobility was measured using transient ion current (TIC) technique as described elsewhere [51]. In this technique, the sample is polarized with a potential of 0.5V for 1 hour and then the polarity is reversed. The time taken by the current to achieve its maximum value is obtained. Using the following formula, ionic mobility is measured as $\mu=D^2/V\tau$. As shown in Fig. 4A.31, when polarization is reversed, a peak in the transient is observed. The time of flight is considered as the time taken by the current to reach maximum value. As also shown in Fig. 4A.31 (inset) that the ionic mobility value does not change much with salt addition in comparison to the conductivity. Thus, the rise in conductivity with salt addition readily suggests that salt does provide mobile ions for ionic transport. Further, IL possibly acts as a plasticizer in the matrix and provides channels to salt ions. This may also be the reason for predominantly ionic nature in higher salt concentration samples.

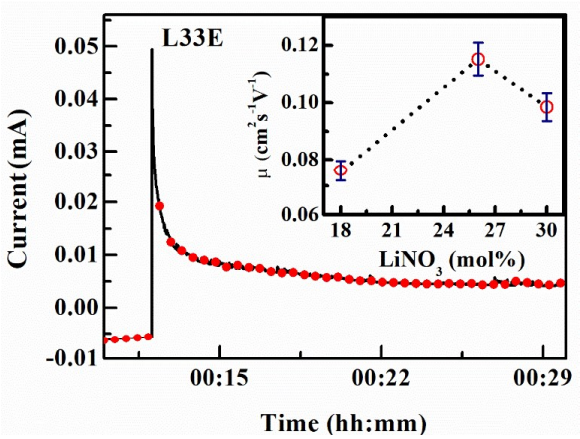

Fig. 4A.31 Switching of the transient current of L33E sample and Ionic mobility (with 10 % error) of prepared samples (inset).

The open-circuit voltage (OCV) of the cells of the type Li/Sample/$LiCoO_2$ as observed are thus reported in Table 4.2, for various series of samples. Interestingly, the OCV almost remains constant when the sample contains IL in a constant amount (fixed to 1 mol%) and salt content is raised. However, when the IL content is increased the OCV shows an apparently decreasing trend. Thus, Li^+ ion activity is seen to be affected by an increase of IL content. This finding complements the electrical transport data (Table 4.2). On the other

hand samples with no salt content and having 4 and 8 mol% of IL exhibit no OCV for this cell. The same samples also exhibit poor conductivity almost 4 orders of magnitude smaller than the samples with salt content.

4A.4.4 Mechanism of electrical transport

The effect of compositional alterations and temperature on electrical transport is again examined using conductivity relaxation. Electrical transport mechanism of the prepared IL-based gel composites can also be understood via well known Jonscher Power Law (JPL) behavior described in many studies on ionic systems [52-53] as well as disordered non-metals [53-55]. The JPL behavior, also known as the universal dynamic response (UDR) deals with frequency dependence of conductivity. The conductivity relaxation process helps in understanding the mobile ion dynamics in solids. The scaling behavior [23, 51-57] can be examined using the characteristic frequency (ω_c) and conductivity (σ_{dc}), according to the following relation:

$$\frac{\sigma}{\sigma_{dc}} = F\left(\frac{\omega}{\omega_c}\right)$$

where, ω_c is the characteristic crossover frequency obtained from the onset point of dc to dispersion region of σ-ω plot. Frequency axis is scaled using the hopping frequency (ω_c) and dc-conductivity as a scaling parameter for the conductivity axis. If the conductivity data scales up on a single master curve, it indicates similar type of ion-relaxation process, whereas, failing indicates a drastic change in conductivity mechanism with composition/temperature change.

Mechanism of electrical transport can be understood using the scaling behavior of the conductivity. σ/σ_{dc} versus ω/ω_c for the prepared samples have been plotted with different temperatures. The plot gives two different types of regions within the measured frequency, (1) plateau region of low frequencies (2) dispersion region of high frequencies. Plateau region gives information about frequency-independent conductivity (σ_{dc}) due to the long-range diffusive motion of ions. Whereas dispersion region informs about the short-range motions of ions within the matrix. At the onset of dc to dispersion the crossover frequency i.e. ω_c was obtained and used for JPL fitting.

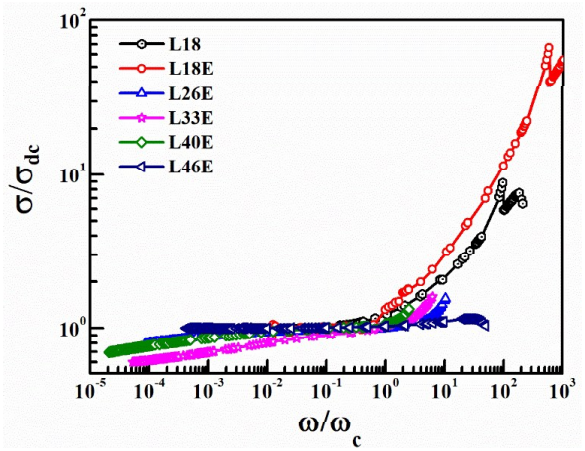

Fig. 4A.32 Scaling behavior of conductivity for Series 1 at 250 °C.

Fig. 4A.32 shows σ/σ_{dc} versus ω/ω_c plot s for series 1 samples at 250 °C. Two different types of regions are witnessed within the measured frequency, (i) plateau region of low frequencies (ii) dispersion region of high frequencies. Apparently scaling is not seen with the variation of composition. Thus, from the figure, it may be suggested that ionic transport mechanism changes with change in composition. This may be due to the fact that salt addition leads to a gradual change of mechanism from predominantly electronic to ionic transport as also supported by dc polarization studies. On the other hand, in Fig. 4A.33 for 33.3% $LiNO_3$ + 1% IL (L33E) has been plotted for a wide temperature range and a good scaling behavior is observed. It supports for a similar type of mechanism in ion transport in the system at different temperatures.

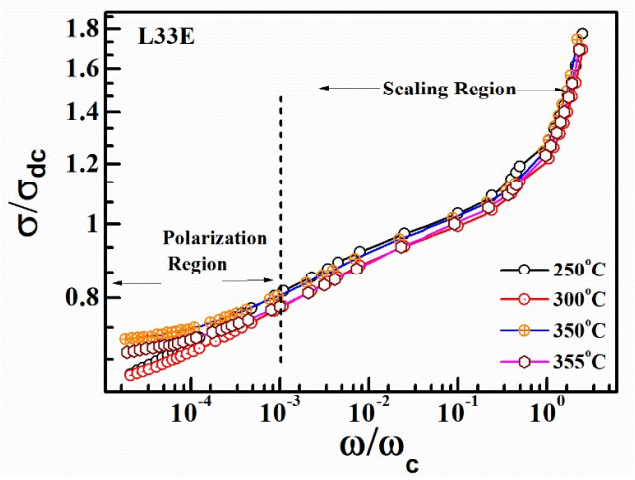

Fig. 4A.33 Scaling behavior of conductivity for L33E with temperature.

4A.5 Conclusions

Ionic liquid ([EMIM] BF_4) confined lithium silica gel composites, found to show appreciable electrical conductivity in the temperature range 150-300 ^oC. The system is thermally stable at this temperature range and measurements are repeatable.

These results reveal interesting results. The samples with no IL content or low salt content are essentially electronic in nature. Addition of IL enhances the overall conductivity by an order of magnitude. Further addition of salt ($LiNO_3$) enhances ionic transport. This is further supported by electrical conductivity and ionic mobility measurements.

Addition of IL to IL-free system increases the electrical conductivity; however, further increasing the content of IL in the composition while keeping the salt ion concentration same, does not improve conductivity, rather reduces it. On the other hand, as mentioned above, keeping IL concentration the same and increasing the salt concentration increases the conductivity. This complex behavior may be due to the possibility of Li^+ ions forming a complex with IL anion.

Silica gels containing only the IL and no salt show no appreciable electrical conductivity, indicating IL on its own is not contributing much to the conduction, but when present in small amounts (1 mol%) enhance the conductivity of salt ions.

System 4B

[EMIM] BF_4 Confined Lithium-Potassium Silicate Gel Composites Prepared by Hydrolytic Sol-Gel Process

4B.1 Composition

System 4B is similar to system 4A except for the fact $LiNO_3$ is partly or fully replaced by KNO_3. KNO_3 was introduced into the matrix of System 4B by hydrolytic sol-gel process exactly in the same way $LiNO_3$ was introduced. The purpose is to understand the effects of K^+ ions introduction on the structure and electrical properties of these composites. If the properties are improved or unchanged by potassium substitution, then potassium can act as a good substitute for lithium. For the prepared composites the compositions are detailed in Table 4.3.

Table 4.3: Composition, Density (error limits ±0.05 gm cm^{-3}) and Molar volume of KNO_3 containing composites.

Sample Code	KNO_3	$LiNO_3$	EMIM BF_4	$CuCl_2$	SiO_2	Density (gm/cm^3)	Molar Volume ($cm^3\ mol^{-1}$)	
	(mol%)					Experimental	Calculat-ed*	Experiment-al
Series-K1								
L9K9	9.1	9.1	0	0.9	80.9	1.232	25.81	52.99
L9K9E	9.1	9.1	0.9	0.9	80	1.153	25.88	57.70
L16K16E	16.6	16.6	0.8	0.8	65	1.206	27.51	57.26
L23K23E	23.1	23.1	0.8	0.8	52.2	1.334	29.76	54.89
Series-K2								
L9K9E	9.1	9.1	0.9	0.9	80	1.153	25.88	57.70
L9K17E	17.4	8.7	0.8	0.8	65	1.116	27.65	62.68
L8K25E	25	8.3	0.8	0.8	65	1.314	29.34	55.38
Series-K3								
L0K18	18.2	0	0	0.9	80.9	1.313	26.65	51.95
L0K18E	18.2	0	0.9	0.9	80	1.226	27.34	56.65

4B.2 Structural Studies

4B.2.1 Density and Molar Volume

Molar volume of the prepared composites is higher than the calculated values indicating for the expansion of the network during the formation of the amorphous compositions

(Table 4.3). However, there is no trend for change in molar volume of the composites with respect to compositional changes as was observed for system 4A.

4B.2.2 Powder X-Ray Diffraction

Halo PXRD pattern of L9K9 and L9K9E composites exhibit their amorphous/glassy nature (Fig. 4B.1). However, PXRD scans for rest all other composites are found to be partially crystalline in nature. Detailed analysis of these plots indicates that these peaks correspond to KNO_3, resulting in the formation of ceramic composites. It is evident from the PXRD plots, that the addition/substitution of KNO_3 beyond a certain limit into the lithium-silicate matrix is not possible, and the expelled KNO_3 gets distributed as microcrystalline particles outside the amorphous network of the composites. The presence of only KNO_3 peaks in PXRD pattern indicates for (in L0K18 and L0K18E composites) expelling of KNO_3 from the silica network, making it partially crystalline in nature.

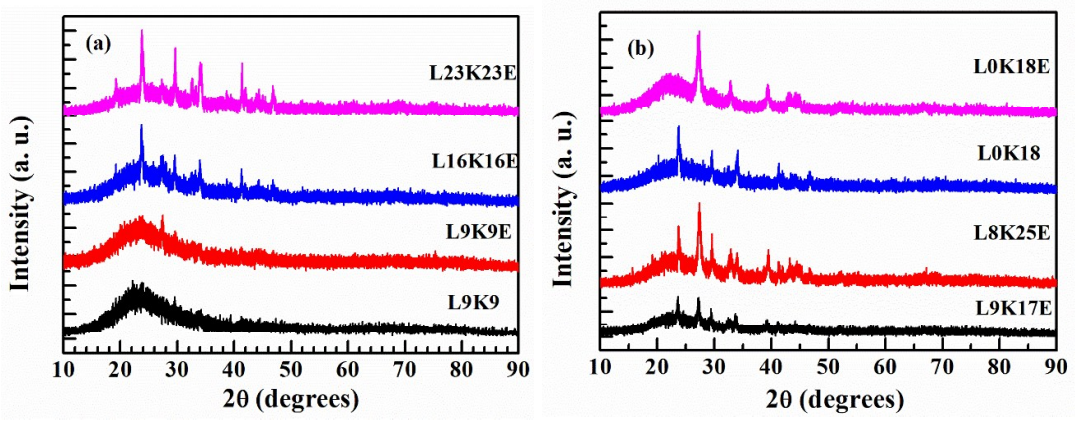

Fig. 4B.1 XRD pattern of the prepared composites with KNO_3 substitution in a lithium silicate matrix

4B.2.3 Fourier Transform Infrared Spectroscopy

The FT-IR spectra are similar to that of system 4A; the hydroxyl groups and hence water in the system is strongly indicated by peaks at 3500 cm^{-1}.

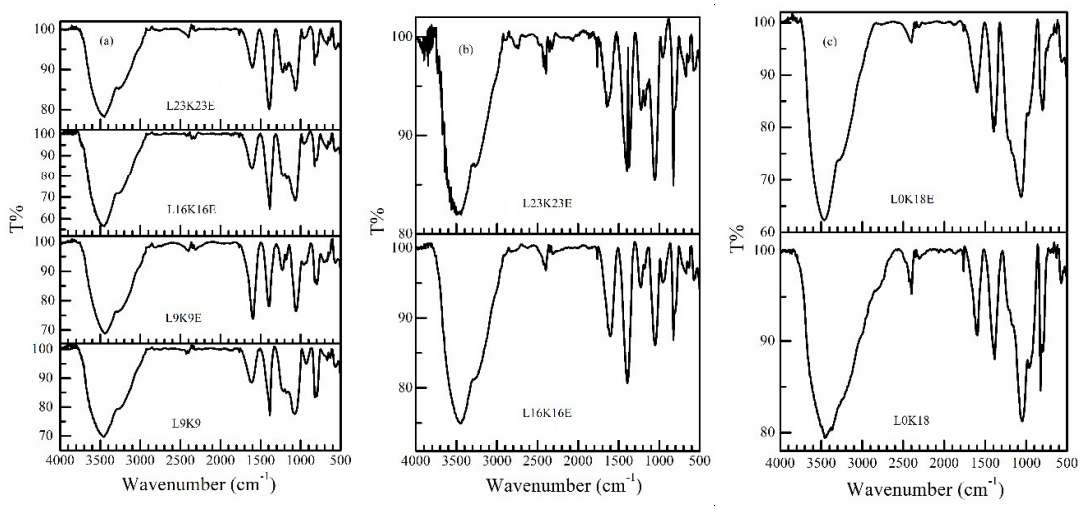

Fig. 4B.2 FTIR in transmission mode (a) Series K1, (b) Series K2 and (c) Series K3.

4B.2.4 Field Emission Scanning Electron Microscopy

Surface morphology of the prepared composites and their corresponding elemental mapping has been analyzed to understand the surface structure and distribution of elements on the matrix. Surface morphology of these composites at 500 nm scale is found to be homogeneous in nature (Fig. 4B.3 and Fig. 4B.4). However, no specific crystalline deposition or precipitation of crystallites has been observed on the surface of these composites, although their PXRD exhibits partial crystalline nature.

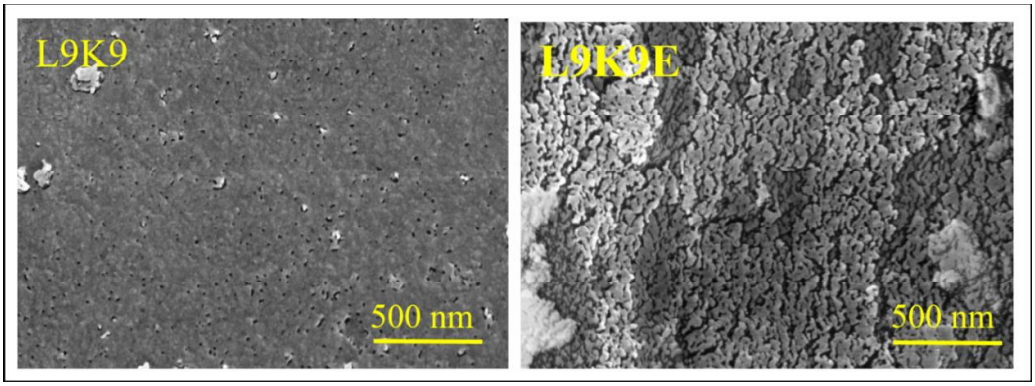

Fig. 4B.3 FESEM images of L9K9 and L9K9E composites.

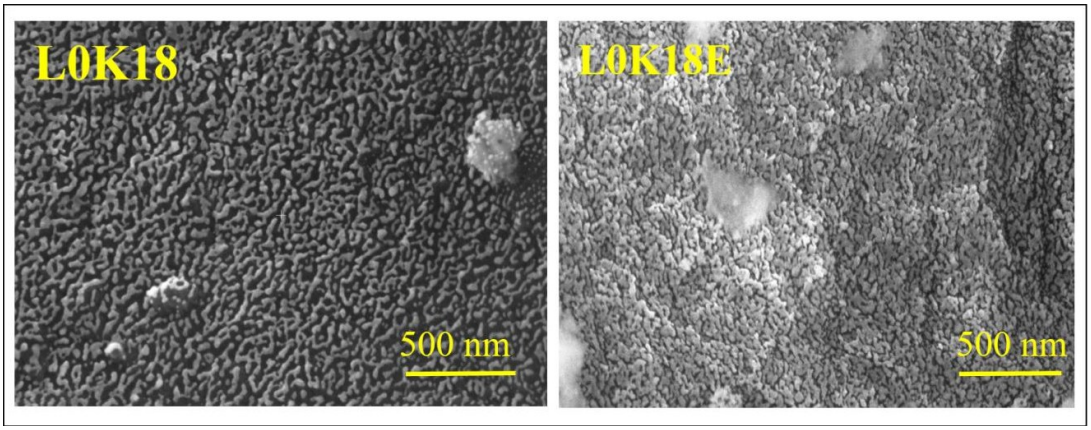

Fig. 4B.4 FESEM images of L0K18 and L0K18E composites.

Homogeneous distribution of the elements within the prepared matrix is evident from the elemental mapping (Fig. 4B.5). On introduction of IL, we find IL is spread everywhere on the surface, but we also see certain aggregation of IL in some areas.

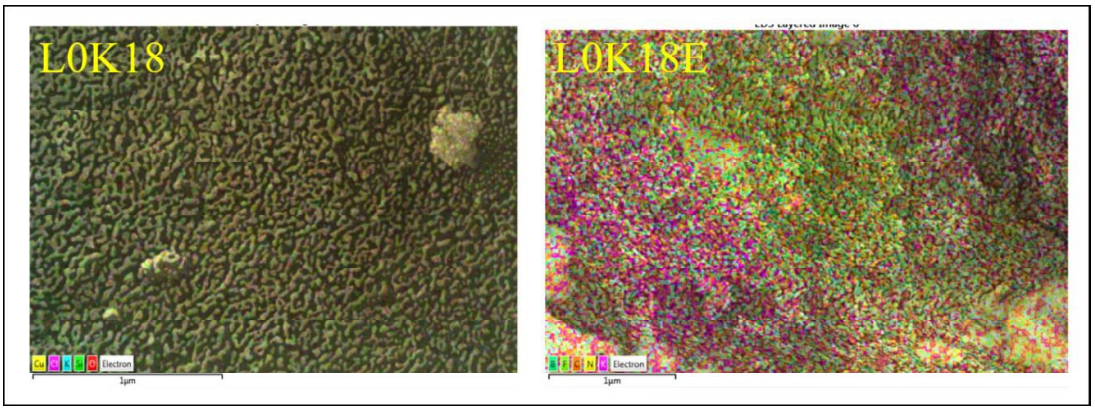

Fig. 4B.5 Elemental mapping images of K18 and K18E composites.

4B.3 Thermal Analysis

4B.3.1 Differential Thermal Analysis

DTA scans of the samples were taken in the temperature range of 35 to 500 °C with a heating rate of 10 °C/minute (Fig. 4B.6) in a nitrogen atmosphere. It has been explained in previous reports that the elimination of water from the prepared matrix occurs in two different forms. An endothermic dip in the temperature range of 75 – 175 °C relates to loss of water and organic residues from the system. The physisorbed water eliminates up to

~170 ^{o}C and the chemisorbed water can be eliminated in the range 170 to 400 °C reversibly [38].

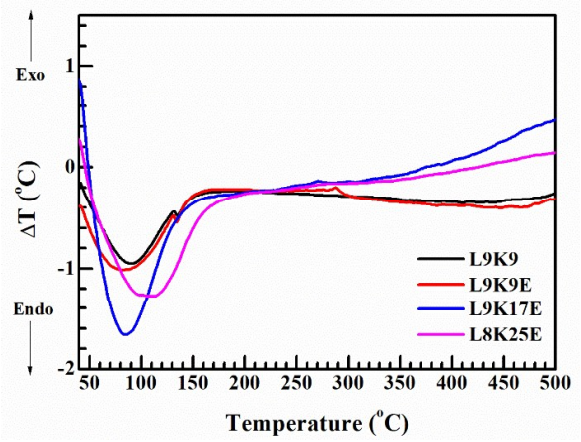

Fig. 4B.6 DTA scan of samples (Series-1).

4B.3.2 Thermogravimetric Analysis

TGA scans were obtained for the prepared silica gel composites (Fig. 4B.7) in a temperature range of 35 – 500 °C with a heating rate of 10 °C/minute in a nitrogen atmosphere. As evident, pristine IL is stable at least up to 250 °C, above which it starts decomposing (or changes its phase) and boiling point of IL can be clearly observed above 350 °C.

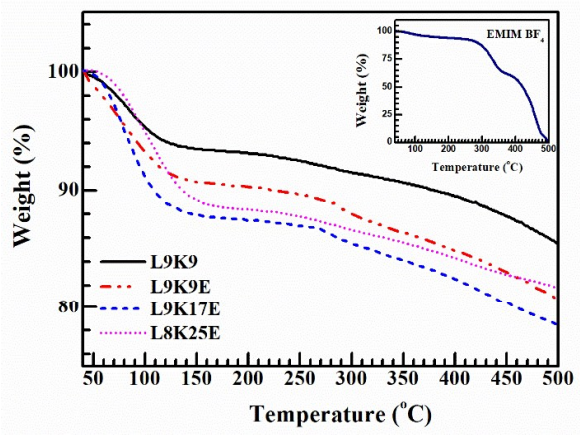

Fig. 4B.7 TGA of the prepared gel composites (Series-1).

Sol-gel prepared composites exhibits ~5% weight loss near 100 °C corresponds to water or organic residue losses. Prepared composites are found to be thermally stable in the

temperature range of 150 - 400 °C. Conductivity cycles have been performed in this stable region only. As explained earlier we observe here also continuous water loss in the temperature range scanned. Up to 400 °C this process is reversible.

4B.4 Electrical Conductivity

4B.4.1 Impedance Spectroscopy

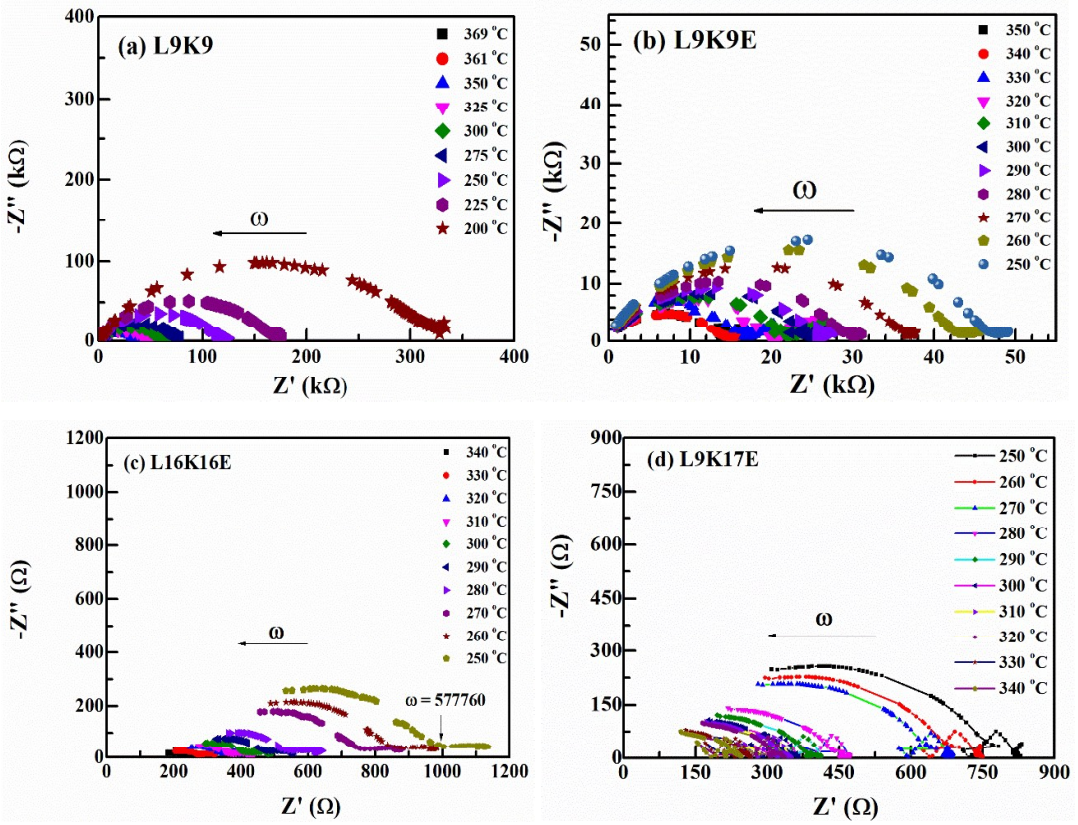

Fig. 4B.8 Nyquist Plots for (a) L9K9, (b) L9K9E, (c) L16K16E, and (d) L9K17E composites with temperature variations.

Nyquist plots (42Hz -5MHz) in blocking electrode configuration for these samples have been analyzed and are shown in Fig. 4B.8. L9K9 composite with no IL showed depressed semicircles. Absence of tail at low frequencies suggests for major electronic contribution. For L9K9E composite, with 1 mol% addition of IL, small spur/inclined tail is evident in the Nyquist plot. This suggests for ionic nature of the composite and marks evidence for the interfacial polarization. Similar to L18 ($18LiNO_3$-$1CuCl_2$-$81SiO_2$) and L18E ($18LiNO_3$-1IL-$1CuCl_2$-$80SiO_2$) composites, dc-polarization studies of L9K9 and L9K9E

composites were performed separately to analyze electronic transport (Fig. 4B.9). To study the polarization behavior, a voltage of 0.5V is applied across the sample and time dependence of the transient current is measured. DC–polarization results confirm predominant ionic transport in both the samples. With the rise in temperature, there is an increase in conductivity of these composites, which marks for these composites to be non-metallic in nature.

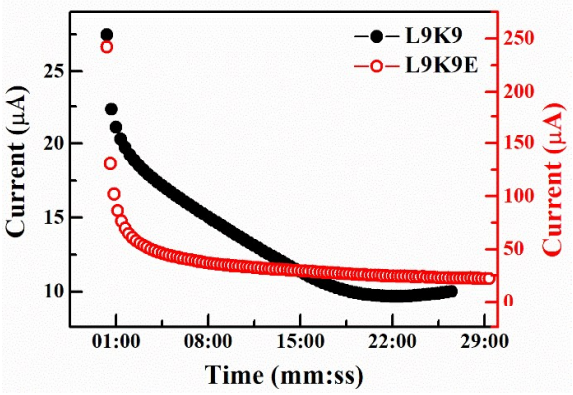

Fig. 4B.9 DC polarization for K9 and K9E composites.

To understand the role of potassium ion substitution in these composites and its effect on electrical conductivity, measurements have been carried out within the thermally stable region.

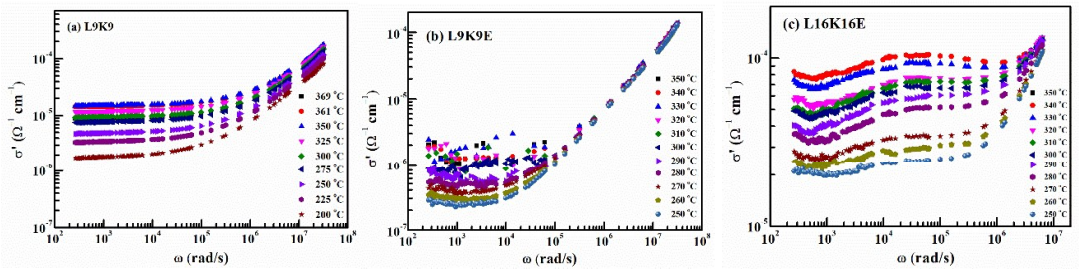

Fig. 4B.10 Frequency dependence of conductivity plots of (a) L9K9, (b) L9K9E, and (c) L16K16E composites with temperature variations.

At the outset, the electrical conductivity (σ) is plotted as a function of frequency (Fig. 4B.10). Conductivity exhibits a plateau in a wide frequency range followed by dispersion in the high frequency region. From the plateau region, the dc conductivity (σ_{dc}) was

obtained, on the other side dispersion region informs about the interfacial polarization. Temperature dependence of σ_{dc} has been plotted in Fig. 4B.11 and Fig. 4B.12.

4B.4.2 Conductivity cycles

Temperature dependence of σ-T cycles exhibits Arrhenius behavior (Fig. 4B.11, 4B.12 and 4B.13). As compared to the previous work with Li^+ ion-containing composites, the conductivity of K^+ ion substituted composites increases by one order of magnitude (L9K9 and L9K9E composites). In previously reported composites, for L18 and L18E, the conductivity obtained at 250 °C was ~10^{-8} and 10^{-7} Ω^{-1} cm^{-1} respectively. However, for potassium-substituted composites, L9K9 and L9K9E, the conductivity obtained was ~10^{-7} and 10^{-6} Ω^{-1} cm^{-1} respectively (Fig. 4B.11). This clearly showed an increase in conductivity of the composites with KNO_3 substitution.

Other compositions of series-K1 and series-K2 were also analyzed for their σ-T properties. As compared to L9K9E composite, a subsequent rise in conductivity of ~2 order of magnitude has been observed for L16K16E composite. This change remains almost unaltered with L23K23E composite (Fig. 4B.12a).

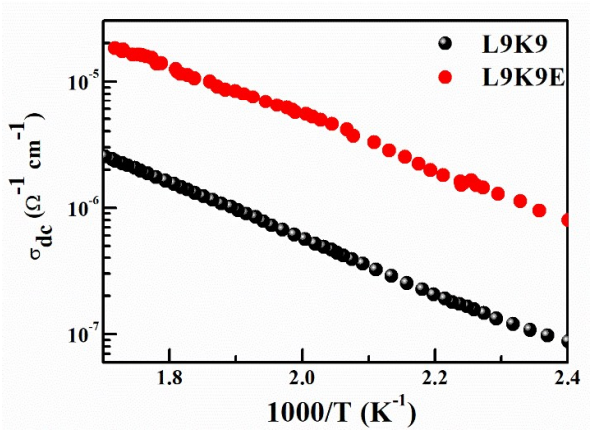

Fig. 4B.11 σ-T cycle of L9K9 and L9K9E composites.

Fig. 4B.12b showed σ-T properties of composites with increasing K^+ ion concentration and keeping Li^+ ion concentration close to 9 mol%. As mentioned in the beginning of this section we observe the rise in conductivity approximately by 2 orders of magnitude for L8K25E (~0.00143 Ω^{-1} cm^{-1} at 558 K) composite compared to L9K9E case.

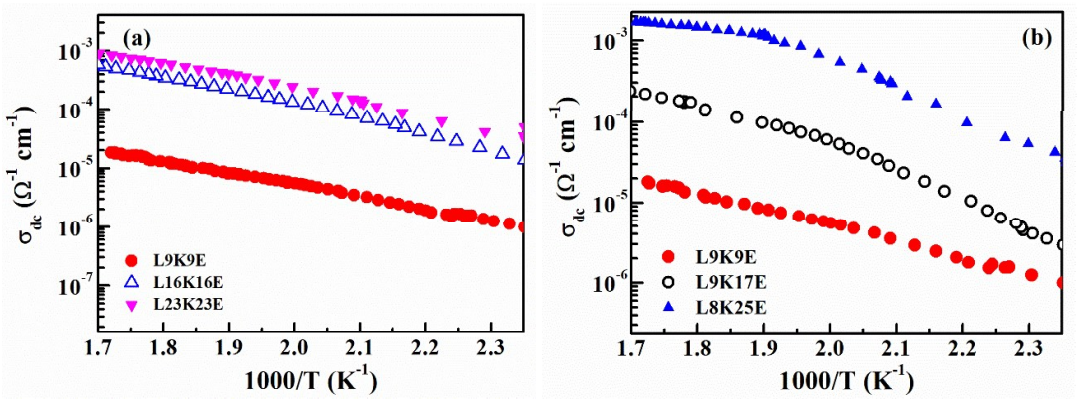

Fig. 4B.12 σ-T cycle of (a) Series-K1 and (b) Series-K2 composites.

In Fig. 4B.13 the σ-T properties of the composites with only K^+ ion-containing composites viz., L0K18 and L0K18E are shown. It is evident from σ-T plots that the conductivity in the entire temperature range is low for the composite where IL is confined. Thus in the composites where only potassium ion is confined, the addition of IL in confinement reduces the conductivity. Exactly reverse trend is observed in only lithium ion confined composites.

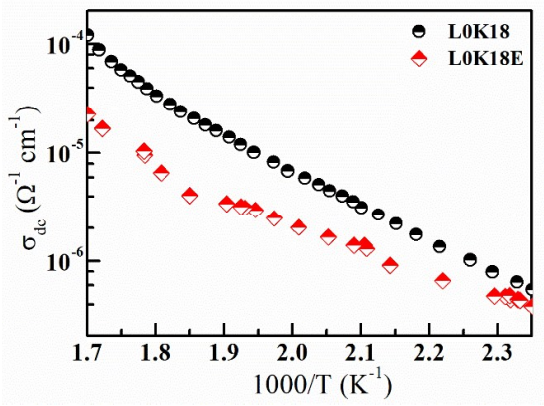

Fig. 4B.13 σ-T cycle of series-K3 composites

The activation energy required in the process of ion conduction has been determined from the slope of σ-T cycles (Table 4.4). It may be noted that in case of L0K18E the conductivity and activation energy both are low compared to the sample without IL (L0K18). This is not contradictory. Due to the additional confinement of IL the conductivity drops down due to structural and other changes which change the pathways of conduction. Within this new structural environment, the increase in conductivity for a specific raise in the temperature is favored in the IL containing composite.

Table 4.4: Activation energy (E_a) and conductivity (at 250 °C) of the composites.

Sample Code	Conductivity at 313 K	Conductivity at 523 K	Conductivity at 548 K	Activation energy (eV)
	(Ω^{-1} cm^{-1})			
Series-K1				
L9K9	$1.1x10^{-7}$	$1.0x10^{-6}$	$1.5x10^{-6}$	0.44
L9K9E	$2.9x10^{-6}$	$8.3x10^{-6}$	$1.2x10^{-5}$	0.42
L16K16E	$2.0x10^{-7}$	$2.3x10^{-4}$	$3.4x10^{-4}$	0.51
L23K23E	$1.5x10^{-6}$	$4.1x10^{-4}$	$5.5x10^{-4}$	0.49
Series-K2				
L9K9E	$2.9x10^{-6}$	$8.3x10^{-6}$	$1.2x10^{-5}$	0.42
L9K17E	$1.7x10^{-7}$	$1.0x10^{-4}$	$1.3x10^{-4}$	0.66
L8K25E	$3.4x10^{-6}$	0.00113	0.00143	0.65
Series-K3				
L0K18	$4.2x10^{-7}$	$1.3x10^{-5}$	$2.9x10^{-5}$	0.63
L0K18E	$1.7x10^{-6}$	$9.4x10^{-6}$	$3.4x10^{-6}$	0.47

In literature we find a phenomenon known as "Mixed Alkali Effect" (MEA) which is based on the observation that in melt quench prepared glasses containing alkali metal oxide, if a second alkali oxide is added then large orders of magnitude changes happen in many properties. Properties most affected are those associated with alkali ion movement such as electrical conductivity and loss, alkali diffusion, internal friction, viscosity etc. [58-59]. Due to MAE the electrical conductivity of a glass which contains two alkali oxides (X and Y) will be less than the conductivity of the same glass if only one oxide (either X or Y) is present with the same total mol %. The conductivity is at minimum when both alkali oxides are present in 50-50 mol%. Swenson and Adams [60], with a model where both the conducting ions have different pathways of low dimensionality, were able to explain the MAE by simulations based on reverse Monte Carlo generated structure models.

Molecular Dynamics based simulations also reveal alkali ions-segregating at micro level and stochastic mixing of alkali ions hinders the conductivity of any particular ion in that mixture [61]. In another molecular dynamics study the authors conclude: Immobilization of ions by the mutually intercepted jump paths has been characterized as ''cooperativity blockage''; dynamical heterogeneity and ''cooperativity blockage'' originating from ion–ion interaction and correlation are fundamental for the observed ion dynamics and the MAE [62]. In summary we can say, the MAE is due to the fact that different alkali ions have different pathways for mobility and in a mixture of alkali ions, the different alkali

ions mutually block the pathways of other ions. MAE in electrical conductivity measurements can persist at higher temperatures also [58].

Table 4.5 Comparison of conductivities of composites with potassium substitution

Sample Code	Total Alkali ion mol%	Li^+ mol%	K^+ mol%	Conductivity at 313 K	Conductivity at 523 K	Conductivity at 548 K
				(Ω^{-1} cm^{-1})		
L18	18	18	0	$1.5x10^{-5}$	**$1.9x10^{-8}$**	**$4.1x10^{-8}$**
L9K9	18	9	9	$1.1x10^{-7}$	**$1.0x10^{-6}$**	**$1.5x10^{-6}$**
L0K18	18	0	18	$4.2x10^{-7}$	**$1.3x10^{-5}$**	**$2.9x10^{-5}$**
L18E	18	18	0	$4.6x10^{-6}$	**$2.3x10^{-7}$**	**$4.6x10^{-7}$**
L9K9E	18	9	9	$2.9x10^{-6}$	**$8.3x10^{-6}$**	**$1.2x10^{-5}$**
L0K18E	18	0	18	$1.7x10^{-6}$	**$9.4x10^{-6}$**	**$3.4x10^{-6}$**
L26E	26	26	0	$4.2x10^{-6}$	**$1.0x10^{-5}$**	**$1.7x10^{-5}$**
L9K17	26	9	17	$1.7x10^{-7}$	**$1.0x10^{-4}$**	**$1.3x10^{-4}$**
L33E	33	33	0	$3.6x10^{-8}$	**$1.5\ x10^{-4}$**	**$2.1x10^{-4}$**
L16K16E	33	16.5	16.5	$2.0x10^{-7}$	**$2.3x10^{-4}$**	**$3.4x10^{-4}$**
L8K25E	33	8	25	$3.4x10^{-6}$	**$1.1x10^{-3}$**	**$1.4x10^{-3}$**
L46E	46	46	0	$2.4x10^{-3}$	$6.5x10^{-5}$	$1.3x10^{-2}$
L23K23E	46	23	23	$1.5x10^{-6}$	$4.1x10^{-4}$	$5.5x10^{-4}$

The conductivity data of some composites of system 4A and 4B are rearranged in the above table (Table 4.5) to look into whether MAE is present in our gel system composites also. The table shows for five sets of composites the electrical conductivity at three different temperatures. As mentioned earlier near room temperature (313 K) the protonic conductivity also contributes to the total conductivity. So we keep this column data aside for this discussion. Also, the last set corresponds to 46% alkali ion conduction and anomalous high conductivity values are observed for such samples (section 4A). Hence we do not include the last two rows of data in our consideration. In all other cases (highlighted numbers) it is very clear that there is no Mixed Alkali Effect seen. Only

conclusion is the conductivity increases with increasing concentration of potassium ion. This means the conducting pathways of lithium and potassium ions do not interfere with each other. They may have the same conducting pathways. Also, potassium ion has better mobility than lithium ion in these composites.

4B.4.3 Ion Transfer Mechanism

To understand the process of ion transport in lithium and potassium composites, scaling behavior in log ω versus log σ plots was determined (Fig. 4B.14) [51-57].

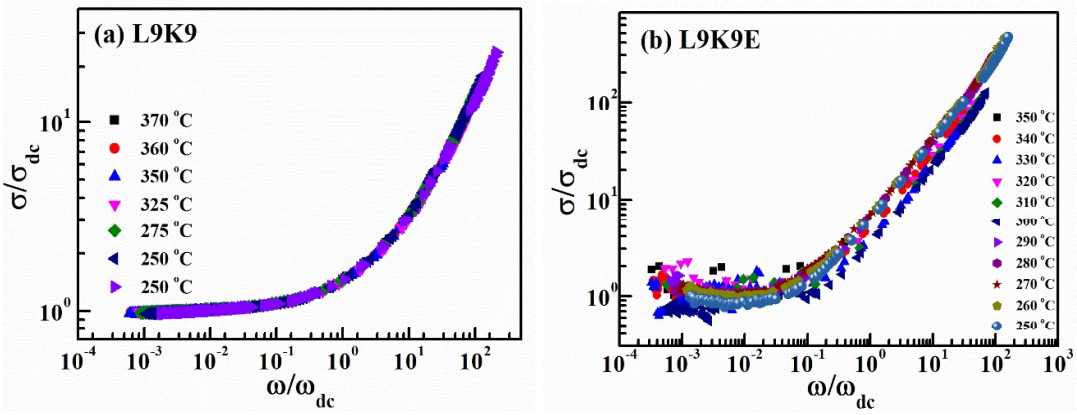

Fig. 4B.14 Scaling behavior of conductivity for (a) L9K9 and (b) L9K9E with temperature variation.

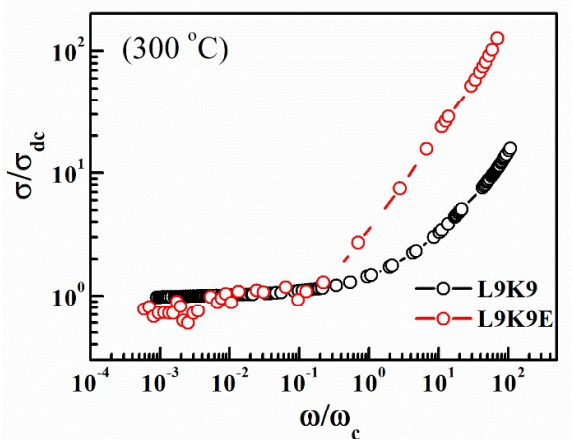

Fig. 4B.15 Scaling behavior of L9K9 and L9K9E composites with salt content at 300 °C.

Frequency-dependent conductivity cycle gives two regions, (1) plateau region of low frequency, which informs about long-range diffusive motion of ions and (2) dispersion region of high frequency, which informs about the short-range motion of ions in the matrix.

σ/σ_{dc} versus ω/ω_c for the prepared samples have been plotted with different temperatures. For L9K9 composite, the ion-relaxation process falls in single master curve irrespective of temperature (Fig. 4B.14a). This specifies a similar ion-relaxation process i.e. available two different conducting ions Li^+ and K^+ follow similar conduction pathways/process. On the other side, for L9K9E composite, also showed scaling behavior (Fig. 4B.14b). However, follows two different relaxation mechanisms in two different temperature ranges i.e. a single master curve can be observed for the temperature range of 250-290 °C and another curve for 300-350 °C. Scaling behavior was also determined with the variation of composition (Fig. 4B.15). From the plot, it is evident that the ionic transport mechanism changes with change in composition.

4B.5 Conclusions

Interesting observations that can be concluded from the study composites of 4B (series-2) are:

1. The composites (with Li^+ ion being substituted by potassium) have been prepared through hydrolytic sol-gel process and exhibit ceramic nature with higher concentrations of potassium.
2. The composites with only potassium ion (no lithium ion) the additional confinement of IL reduces the conductivity.
3. The composites show higher conductivity with increased mol% values of potassium ions.
4. Mixed Alkali Effect (MAE) is not observed in these silica gel composites prepared through sol-gel process.
5. The above two points imply that the conducting pathways of lithium and potassium ions do not interfere with each other and potassium ion has better mobility.
6. The ion transport mechanism of these composites is similar for ion-transfer process in the absence of IL whereas in the presence of IL two different temperature dependent ion transfer processes are observed.

System 4C

[EMIM] BF_4 Confined Lithium Silicate Gel Composites Prepared by Non-Hydrolytic Sol-Gel Process

4C.1 Compositions

The hydrolytic sol-gel process was used to prepared silica gel composites in section 4A. Those composites exhibit interesting structure and conducting properties. To understand the effect of preparation procedures on these properties, the present section, deals with the preparation of the similar composites mentioned in section 4A by non-hydrolytic sol-gel process. Compositions and some physical properties are mentioned in Table 4.6.

Table 4.6 Compositions, density and molar volume of the silica gel composites of non-hydrolytic processing.

Sample Code	$LiNO_3$	EMIM BF_4	$CuCl_2$	SiO_2	Density (gm cm^{-3})	Molar Volume (cm^3 mol^{-1})	
	(mol%)				Experimental	Experimental	Calculated*
Series-1							
L18n	18.2	0	0.90	80.9	1.617	38.57	23.89
L18En	18.2	0.90	0.90	80.0	1.613	39.40	24.54
L26En	26.1	0.87	0.83	72.2	1.758	36.52	24.98
L33En	33.3	0.83	0.83	65.0	1.666	38.88	25.40
L40En	40	0.80	0.80	58.4	1.535	42.55	25.72
L46En	48	0.80	0.80	50.4	1.534	43.04	26.20
Series-2							
L18En	18.2	0.90	0.90	80.0	1.613	39.40	24.54
L18E2n	18.2	1.80	0.90	79.1	1.497	43.35	25.16
L18E3n	18.2	3.60	0.90	77.3	1.558	43.26	26.33
L18E7n	18.2	7.30	0.91	73.6	1.788	40.51	28.86
Series-3							
L18E3n	18.2	3.6	0.90	77.3	1.563	43.26	26.33
L33E3n	33.3	3.3	0.83	62.5	1.723	39.56	27.05
L40E3n	40	3.2	0.80	56	1.664	41.24	27.45
L46E3n	48	3.1	0.77	50	1.619	42.58	27.68

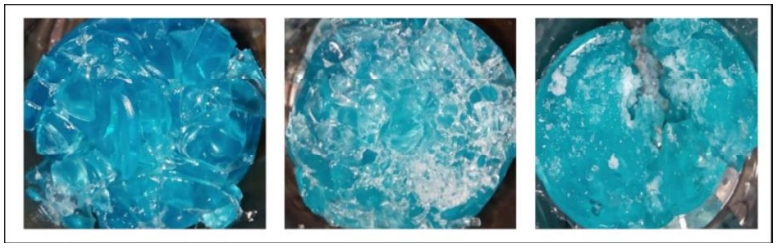

Fig. 4C.1 The photographic image at 1x magnification for stabilized gel after drying homogeneous sol at room temperature.

4C.2 Structural Studies

4C.2.1 Density and Molar Volume

Fig. 4C.2 shows the molar volume variations with the change in concentration of IL as well as $LiNO_3$. Higher calculated molar volume of the composites indicates for the expansion of the network at the time of composite formation. This expanded network indicates the void space or pores in the silicate network that can be used in confinement of different materials of interest.

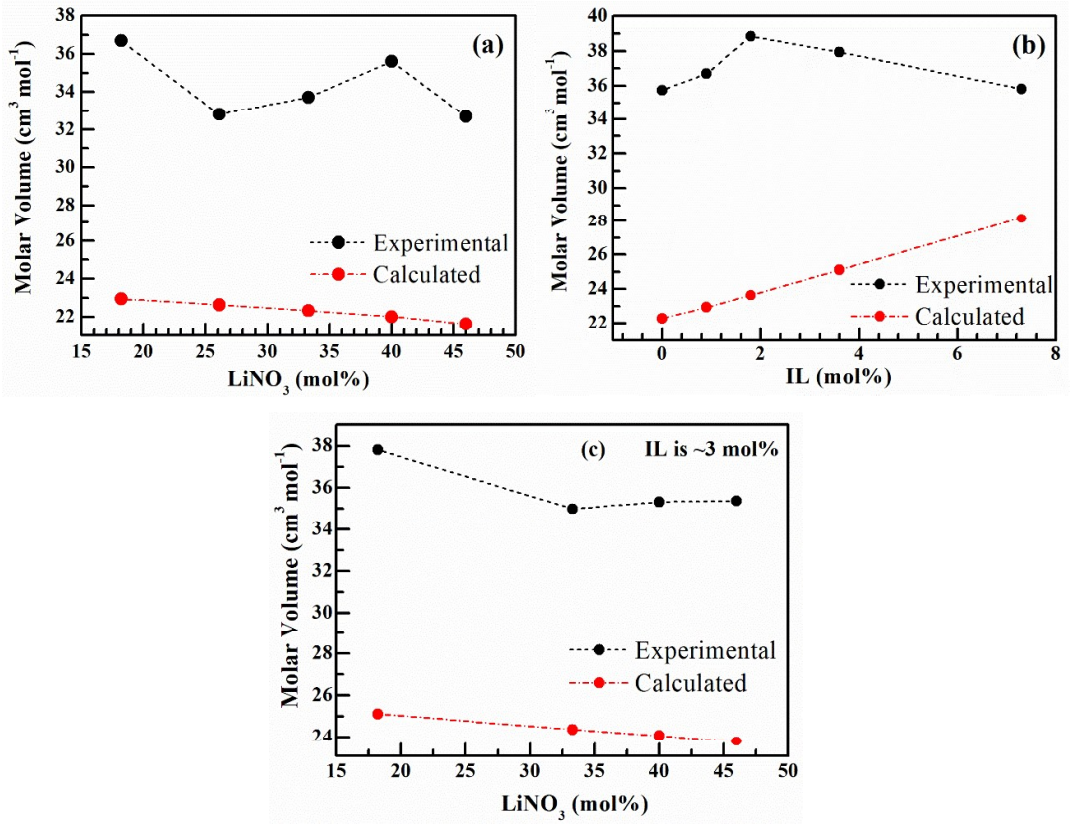

Fig. 4C.2 Molar volume plots for (a) Series 1, (b) Series 2 and (3) Series 3 (with error limits of ±0.05 cm^3 mol^{-1}).

As is evident from the plot, with an increase in IL concentration there is a gradual fall in the molar volume of the composites beyond 2 mol% IL substitution. However, any definite trend could not be observed with respect to the changes in $LiNO_3$ concentration. Nevertheless, a gradual decrease in the molar volume of the composites can be noticed for

series-3 composites. Table 4.6 details about the density and molar volume of the prepared composites.

4C.2.2 Powder X-ray Diffraction

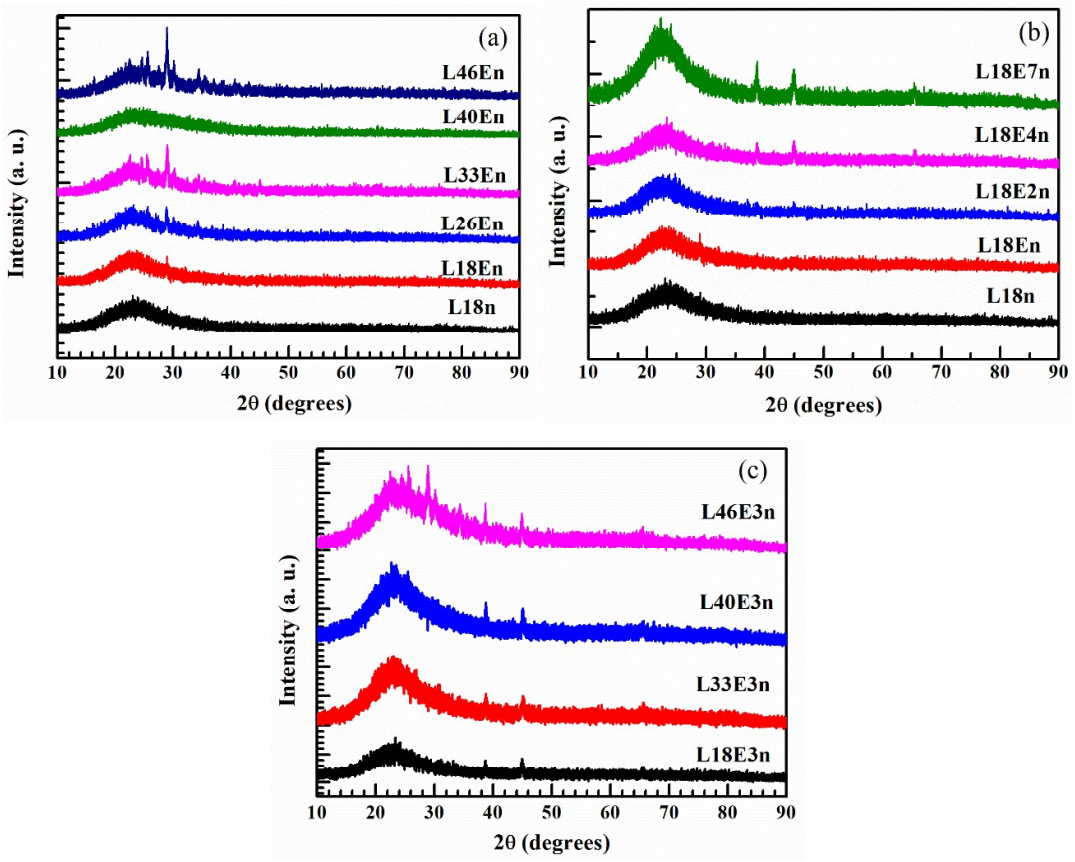

Fig. 4C.3 PXRD profile for the prepared samples via sol-gel non-hydrolytic route. (a) Series 1, (b) Series 2, and (c) Series 3.

Halo patterns (Fig. 4C.3) for most of the prepared samples confirm their amorphous nature in a wider range of planned compositions. However, composites with higher salt as well as IL content exhibit certain peaks of unknown phases. We assume these composites are almost amorphous in nature. PXRD analysis indicates that approximately 33 mol% $LiNO_3$ and 3 mol% IL can safely be accommodated in the amorphous network of the system without disturbing it.

4C.2.3 Electron Paramagnetic Resonance Spectroscopy

EPR of a single composite were determined in X-band and Q-band regions. Presence of Cu^{+2} hyperfine splitting can be clearly seen from Fig. 4C.4.

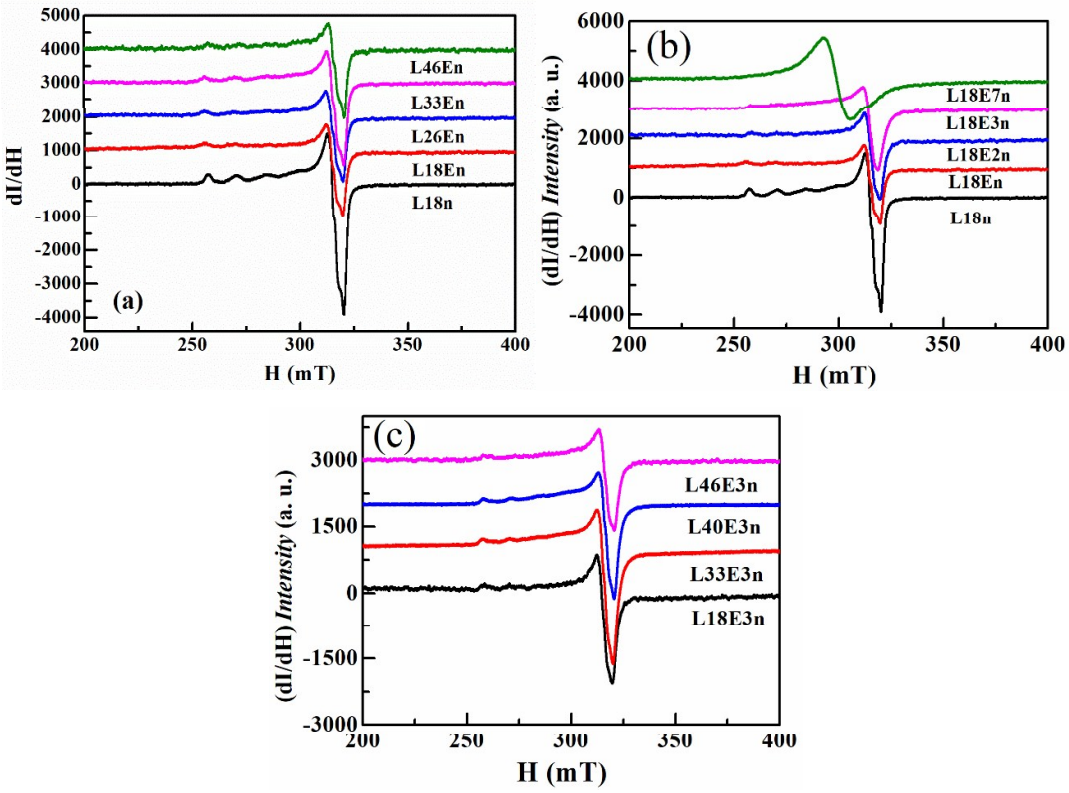

Fig. 4C.4 X-band EPR plots for the prepared samples via sol-gel non-hydrolytic route. (a) Series 1, (b) Series 2, and (c) Series 3.

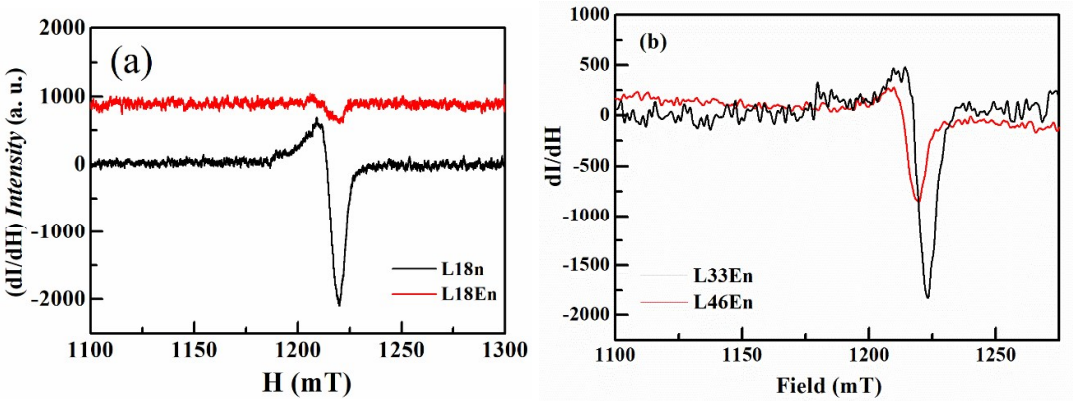

Fig. 4C.5 Q-band EPR plots for the prepared samples via sol-gel non-hydrolytic route. (a) L18 and L18E, and (b) L33E and L46E composites.

From the EPR spectra of the composites the following points may be concluded: (i) At lower concentrations of ionic liquid Cu^{2+} ion is in axial symmetry and not having any fast dynamic movement as the spectrum is anisotropic and well separated hyperfine splittings are seen in parallel and perpendicular regions. (ii) The spectral lines are broadened with increasing concentrations of both lithium ion and IL. Even though the cupric ion concentration is maintained the same in all these composites, when the sites available for cupric ion attachment are getting reduced these are forced to occupy the nearby sites thus increasing the dipolar broadening. (iii) At higher concentrations of IL (L18E7n) we see the spectrum is isotropic and the cupric ion is having dynamic movement in the solvent pools in the nano-pores or otherwise. (iv) As has been explained in section 4A the loss of hyperfine line resolution at higher frequency (Q-band) for samples of low IL content indicates the inhomogeneous distribution of structural parameters from micro site to micro site. (v) By inference we can extend the conclusion to lithium ion and say Li^{+} may also have distributed bonding parameters. (vi) We could record only the room temperature (RT) or lower temperature (LNT) EPR spectra of the samples. Thus we cannot correlate this distribution to the high temperature conductivity variation with respect to composition in our samples.

4C.2.4 FTIR Spectroscopy

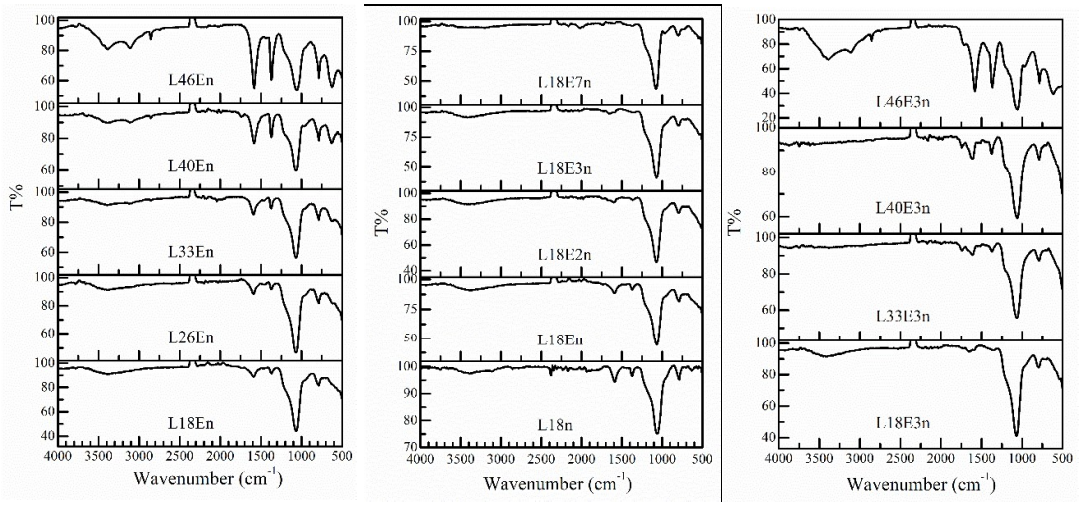

Fig. 4C.6 FTIR for the composites prepared from the non-hydrolytic sol-gel route in ATR mode (a) Series-1, (b) Series-2, and (c) Series-3.

FTIR measurement of the pristine IL has been discussed in the previous section. FTIR of non-hydrolytically prepared silica gel composites was recorded in both ATR as well as in transmission mode. ATR mode transmission spectra have been plotted in Fig. 4C.6 whereas, transmission mode spectra has been plotted in Fig. 4C.7 for their comparative studies.

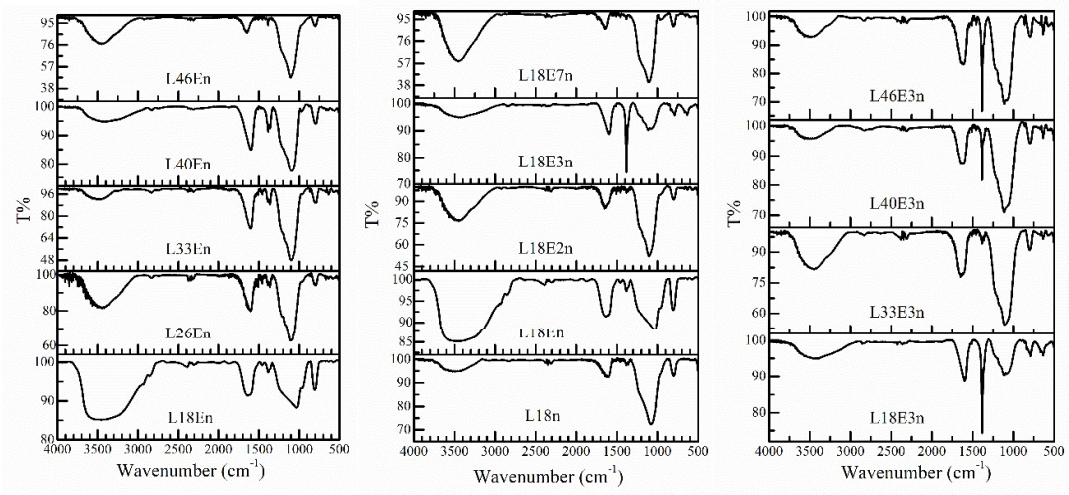

Fig. 4C.7 FTIR for the composites prepared from the non-hydrolytic sol-gel route in transmission mode (a) Series-1, (b) Series-2, and (c) Series-3.

From ATR plots of the composites characteristic, IR peaks of Si-O-Si stretching can be observed in the region of 1000-1200 cm^{-1} for all the composites. Other peaks can be explained in a similar way to that of the composites of system 4A. Along with these findings, another interesting observation is regarding the formic acid used in the preparation. The presence of OH group is indicated in 3400-3000 cm^{-1} region absorptions. However, the carbonyl stretching at ~1700 cm^{-1} is missing. It is possible the formic acid exists in the ionized form of as formate and the peaks near 1600 cm^{-1} are indicative of that. The OH stretching observed may be due to the formation of silanol moieties formed with silicate network by the released protons or the formation of the ethanol during the network forming reaction. In ATR scan of the samples, IR peaks corresponding to hydroxyl groups are seen in trace amount whereas, these peaks can be prominently seen in IR spectrum taken through-transmission mode, indicating this ionization may be taking place only in the inner pores of the network and the ethanol released during the formation of network is also present there.

4C.2.5 Field Emission Scanning Electron Microscopy

Morphology of the composites has been explored through FESEM analysis. Homogeneous nature of the samples increases with increase in IL concentration in these composite (Fig. 4C.8).

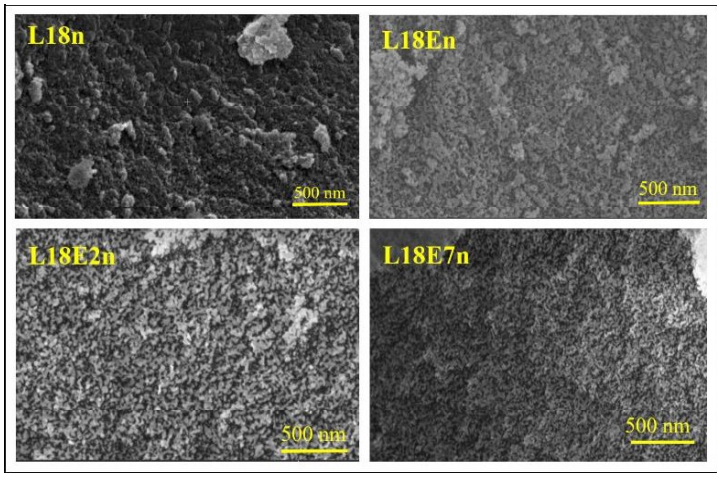

Fig. 4C.8 FESEM images of non-hydrolytically prepared composites with increasing IL concentration (Series-2).

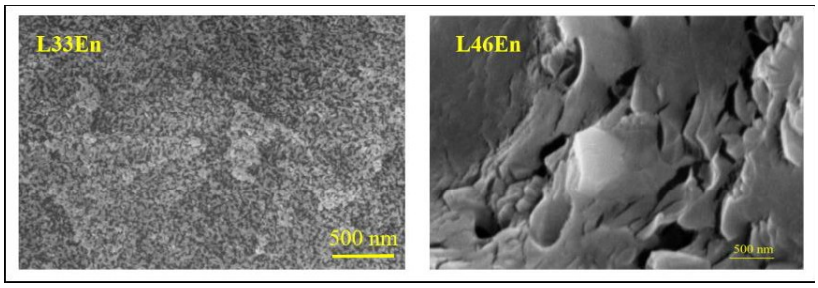

Fig. 4C.9 FESEM images of non-hydrolytically prepared L33En and L46En composites (Series-1).

On increasing the salt concentration into the composites, there occurs no major change in homogeneity. Even for the increase in the concentration of both IL and $LiNO_3$ salt, the homogeneous nature of the composites remains unaffected. All these results indicate that (i) elements corresponding to the prepared silca gel are evenly distributed, and (ii) such a distribution is seen for a wide composition range.

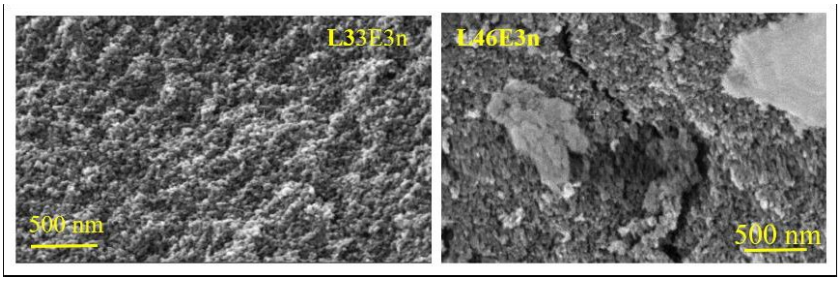

Fig. 4C.10 FESEM images of non-hydrolytically prepared composites from Series-3.

4C.3 Thermal Analysis

4C.3.1 Differential Thermal Analysis

Measurements for DTA scans were taken in a temperature range of 35 °C to 500 °C with a heating rate of 10 °C/minute in a nitrogen atmosphere.

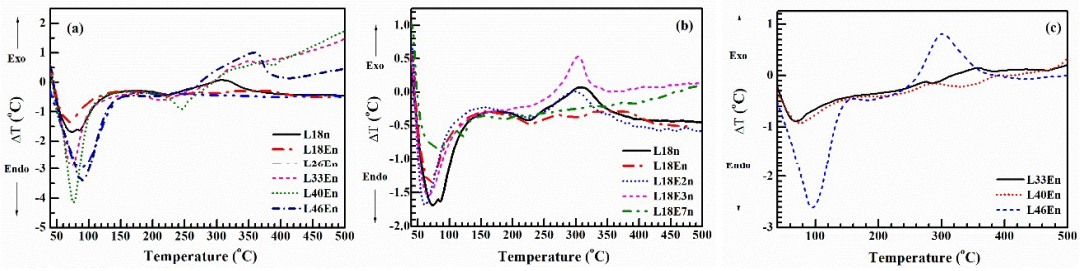

Fig. 4C.11 DTA scan for the composites prepared from the non-hydrolytic sol-gel route: (a) Series-1, (b) Series-2, and (c) Series-3.

These samples are prepared via non-hydrolytic sol-gel route, where formic acid has been used as co-solvent as well as an initiator to both hydrolysis and condensation process of silanols (procedure explained in chapter 2). The small quantity of organic residues (H_2O, EtOH, and EtOOCH) was released during the process can be trapped inside the ultra-porous gel. First endothermic dip in the temperature range of 50 - 150 °C, relates to the loss of adsorbed organic residues from the system. Minimum of endothermic dip is ~78 °C (Fig. 4C.11), corresponds to the boiling point of ethanol released from the surface of the composites and from the capillaries of the ultra-porous structure. Fig. 4C.11a and 4C.11b, second endothermic peaks around 250 °C correspond to $LiNO_3$ melting which is being present in traces in the samples with high lithium concentration. An exothermic peak in the temperature range of 300 - 350 °C corresponds to the removal of IL from the composites. Thus unlike the hydrolytic route the IL is not confined in the nano-pores of

the gel in the samples of non-hydrolytic route preparations if they are heated in the temperature range of 300 - 350 °C.

4C.3.2 Thermogravimetric Analysis

TGA scans (Fig. 4C.12) were obtained for the prepared IL-composite samples via non-hydrolytic sol-gel route.

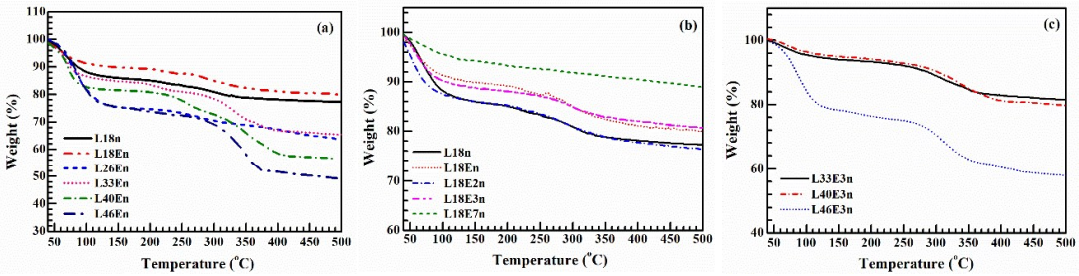

Fig. 4C.12 TGA scan for the composites prepared from the non-hydrolytic sol-gel route: (a) Series 1, (b) Series 2, and (c) Series 3.

Stability of the IL has been explained in the previous section (section 4A). The prepared composites exhibit a weight loss near 100 °C. This is in conformity with the DTA results where we identified this with the loss of confined water/organic residues from the composite. It is interesting to note that, as observed in DTA 300 - 350 ^{o}C there is weight loss which corresponds to removal of IL from the composite by evaporation/decomposition. This is specific to samples prepared through non-hydrolytic route. Based on DTA and TGA results in the stable region of 150 - 300 ^{o}C has been chosen for the electrical conductivity studies.

4C.4 Electrical Transport

4C.4.1 Impedance Spectroscopy

Nyquist Plots (42Hz to 5MHz) of the prepared composites are shown in Fig. 4C.13 and Fig. 4C.14. These measurements have been taken under the blocking electrode (Ag/Electrolyte/Ag) configuration. For L18n composite, only a depressed semicircle without any tail/spur at lower frequency has been observed. This suggests for a parallel combination of resistance and a constant phase element (CPE) with the predominant electronic contribution in electrical conductance. Substitution of IL into the system in very

small amount exhibits no change in nature of Nyquist plots. These results show no clear evidence for ionic transport in low-frequency regions and direct for dominant electronic contribution in these composites. Increase in concentration of IL in the composites also showed no change in the nature of plots this indicates there is no contribution of IL (in any form) towards conductivity.

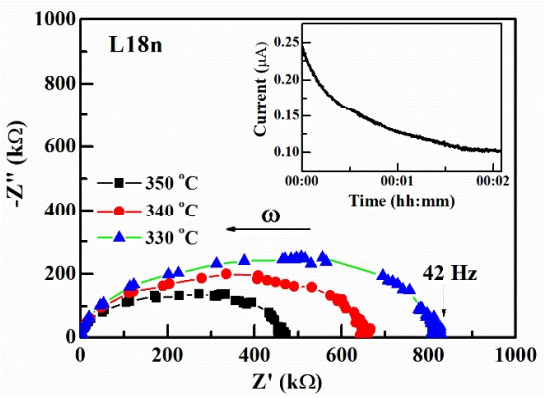

Fig. 4C.13 Nyquist Plots for L18n composite.

To understand the role of IL in the conduction process, its concentration has been fixed to 1 mol% and then the concentration of Li^+ ions has been increased. Unlike composites prepared via hydrolytic route these composites also presented no change in their Nyquist plots except for L46E composite, where a very small tail is visible in low-frequency region and this clearly quantified for the ionic contribution in conduction process.

With the increase in temperature radius of the semicircle decreases and shifts towards the origin, this marks for an increase in conductivity of the composites with a rise in temperature. However, basic conduction nature/process remains the same. Therefore, it is indicated that no significant contribution of IL in the whole conduction process. Its existence in the matrix possibly creates conduction pathways. However, the matrix prepared through non-hydrolytic route is not able to hold the IL beyond a particular temperature as shown by DTA and TGA. Thus in the vicinity of 300 ^oC the silica network starts collapsing with the removal of IL.

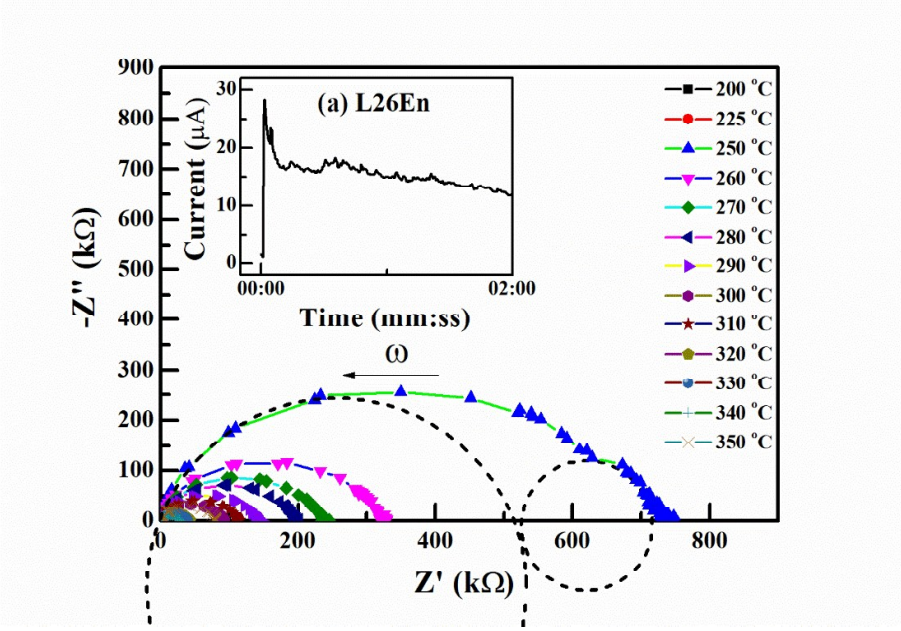
(a) L26En
Current (μA)
Time (mm:ss)
00:00
02:00
ω
-Z'' (kΩ)
Z' (kΩ)
200 °C
225 °C
250 °C
260 °C
270 °C
280 °C
290 °C
300 °C
310 °C
320 °C
330 °C
340 °C
350 °C

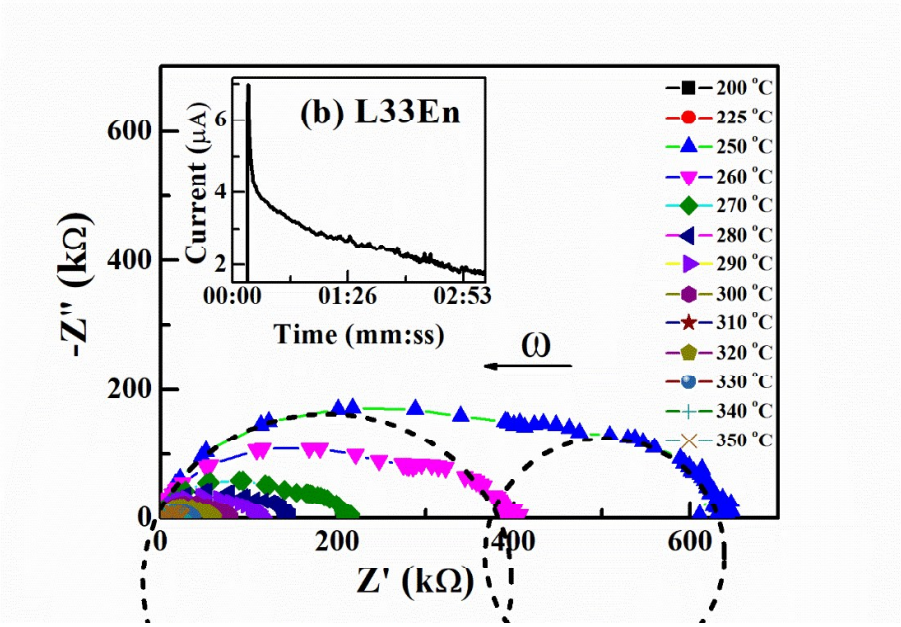
(b) L33En
Current (μA)
Time (mm:ss)
00:00
01:26
02:53
ω
-Z'' (kΩ)
Z' (kΩ)
200 °C
225 °C
250 °C
260 °C
270 °C
280 °C
290 °C
300 °C
310 °C
320 °C
330 °C
340 °C
350 °C

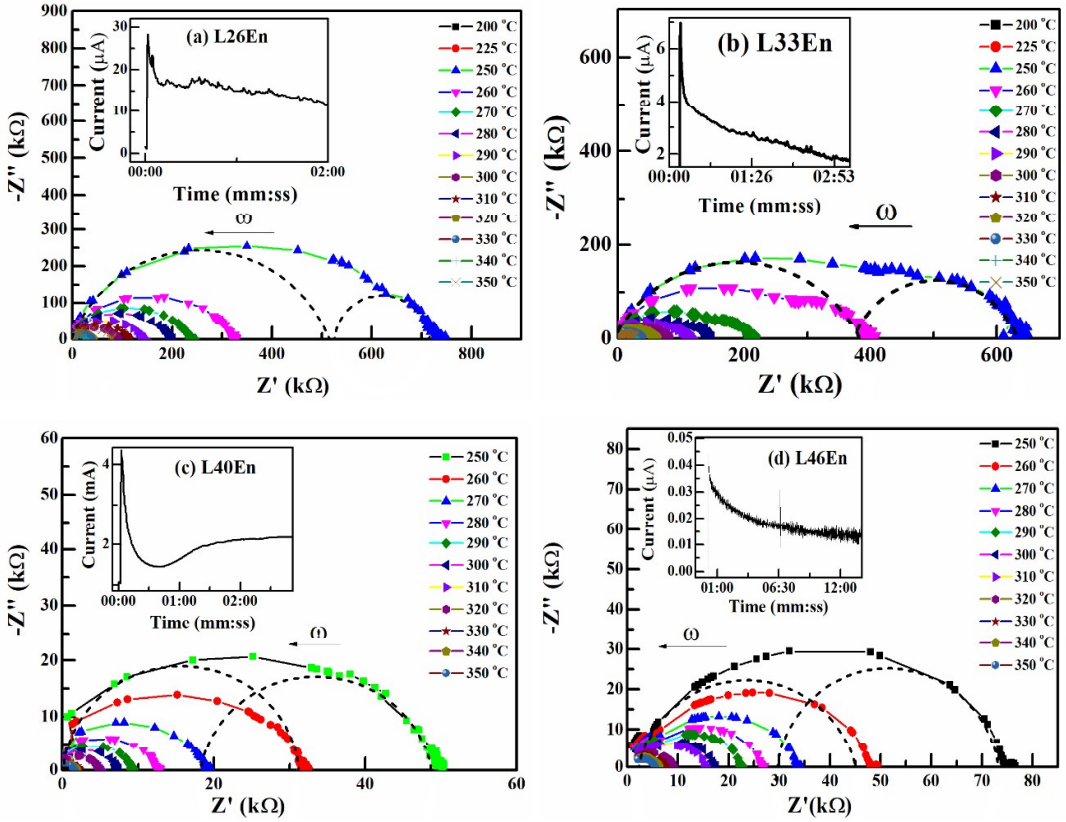

Fig. 4C.14 Nyquist Plots for Series 1 composites.

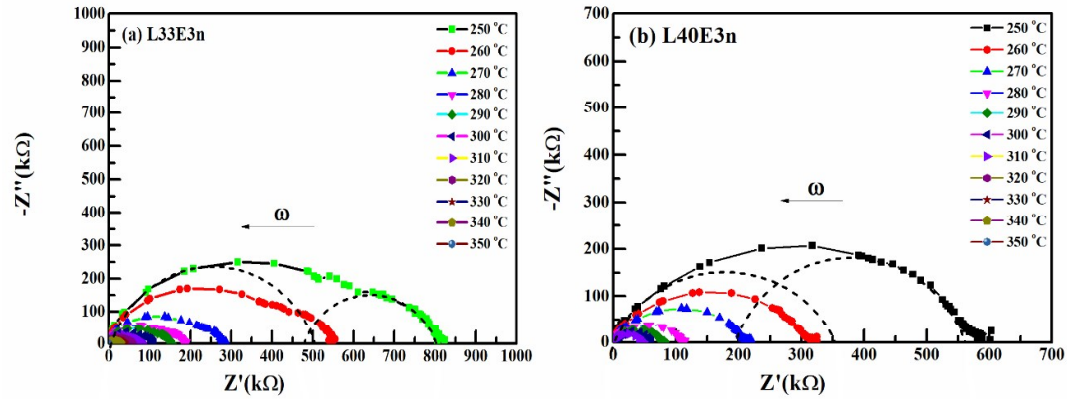

Fig. 4C.15 Nyquist Plots for (a) L33E3n, and (b) L40E3n composites from Series 3.

The semicircles appearing in Fig. 4C.15 are depressed in nature. In fact, for these compositions (Fig. 4C.14 – 4C.15) when one observes carefully the broad semicircles appears to be composed of two merged up semicircles as shown by the dotted line in some of the figures. Such behavior is absent in the composition of other systems. However, this result was repeated and appears similar in every measurement. In composites, the systems

exhibiting two semicircles have been attributed to in-grain and grain-boundary ionic transport. The lower-frequency semicircles is generally attributed to inter-grain electrical transport, whereas, the one at higher-frequencies corresponds to the bulk process. In the present case, however, we note that the matrix is amorphous in nature and no evidence for participation of any phase was seen. It appears that the inhomogeneity in the matrix is possibly responsible for this behavior. This is again is due to the fact unlike other systems the IL is not stable inside the pores of these non-hydrolytic gels starting 300 ^{o}C. So in repeating the experiment in thermal cycles one encounters IL deprived amorphous material 2nd cycle onwards. The ionic conductivity of lithium ion is not enhanced by this.

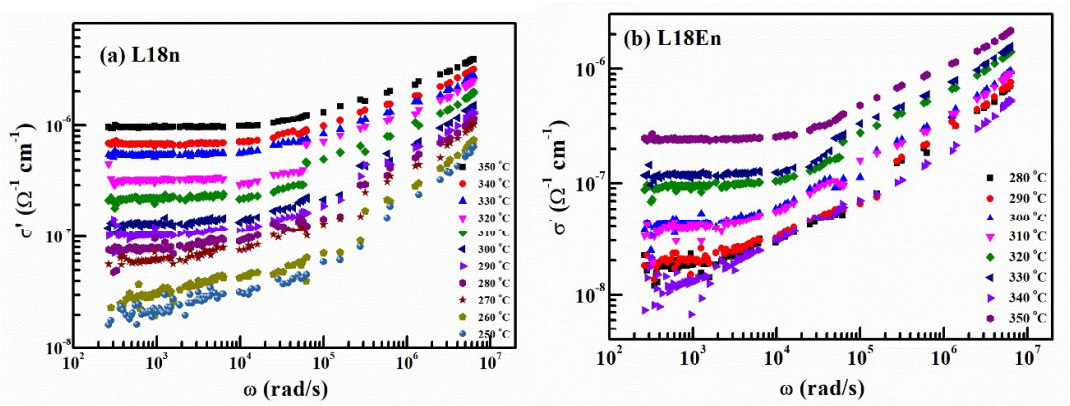

Fig. 4C.16 Electrical conductivity (σ′) as a function of frequency (ω) for L18n and L18En composites in a temperature range of 250 – 350 ^{o}C.

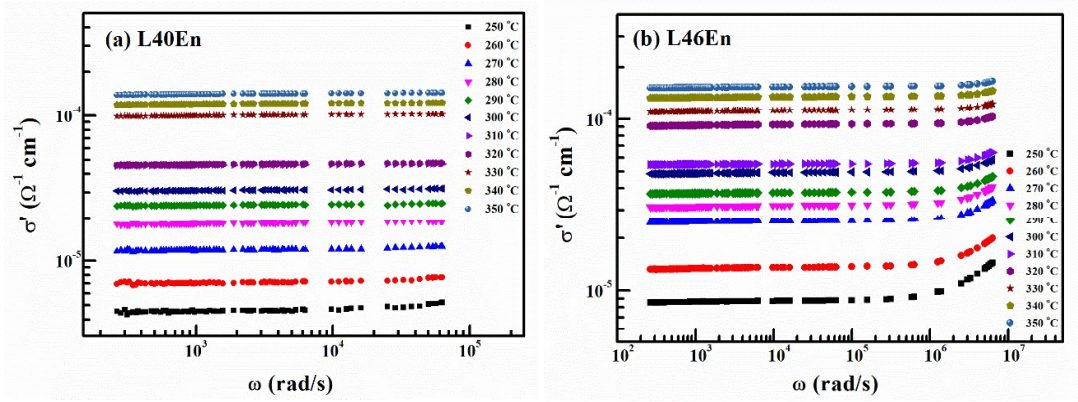

Fig. 4C.17 Electrical conductivity (σ′) as a function of frequency (ω) for (a) L40En, and (b) L46En composites with temperature variations.

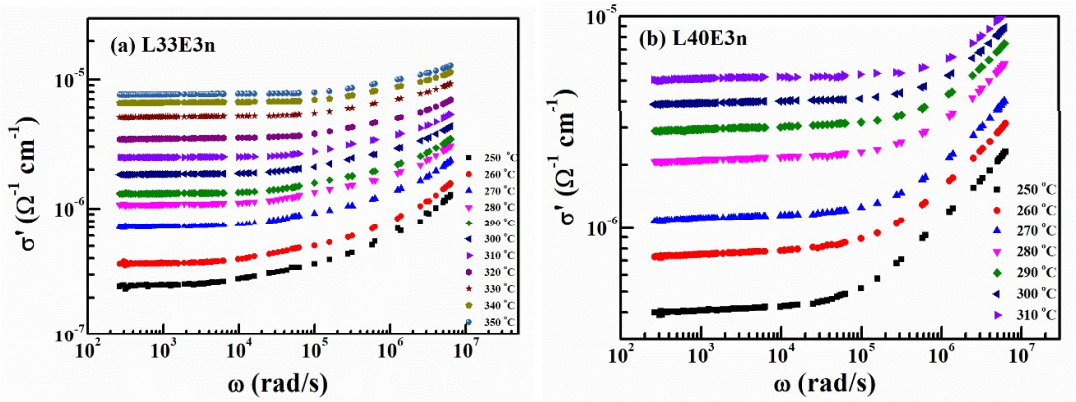

Fig. 4C.18 Electrical conductivity (σ′) as a function of frequency (ω) for (a) L33E3n, and (b) L40E3n composites with temperature variations.

Electrical conductivity measurements of the composites have been reported in a temperature range of 150 - 350 °C. Electrical conductivity (σ′) as a function of frequency (ω) for different compositions in a temperature range of 250 - 350 °C has been plotted in Fig. 4C.16 - Fig. 4C.18.

Two different regions can be easily observed in these plots, (i) plateau region in a wide frequency range and (ii) dispersion region in the high-frequency range. Plateau region is used to determine σ_{dc}. Variation in σ_{dc} with composition and with the rise in temperature has been explained further.

4C.4.2 Conductivity cycles

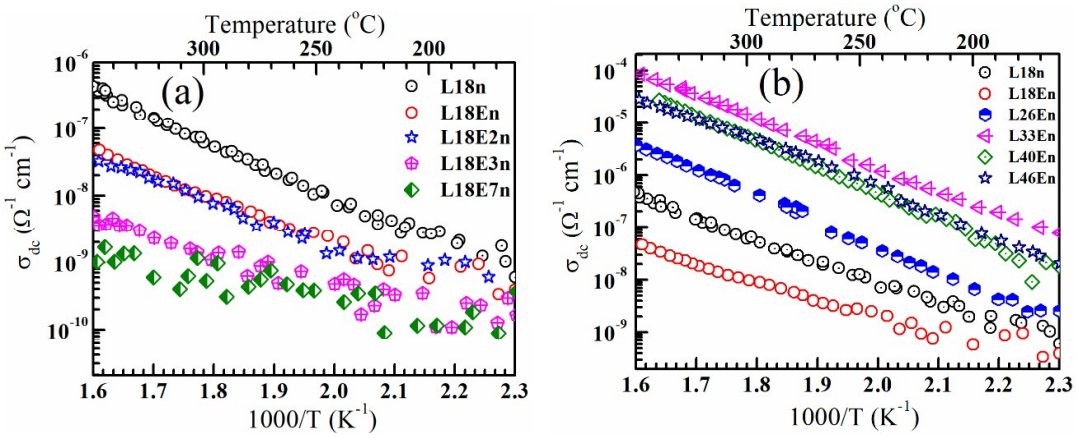

Fig. 4C.19 σ_{dc}-T cycle for (a) Series 1, and (b) Series 2.

Interesting trends have been observed for σ-T cycles of the prepared composites. Fig. 4C.19 indicated the effect of an increase in IL concentration while keeping lithium salt content constant (18 mol%). Unlike the gel composites prepared via hydrolytic sol-gel process, the composites prepared from non-hydrolytic process exhibits quite a different trend in conductivity.

On one side, the addition of a small amount of IL (1 mol%) into the hydrolytically prepared composites exhibits an increase in conductivity i.e. for L18 at 250 °C $\sim 10^{-8}\ \Omega^{-1}\ cm^{-1}$ and for L18E $\sim 10^{-7}\ \Omega^{-1} cm^{-1}$. On the other hand, composites of same compositions prepared via non-hydrolytic process, exhibit almost an order of magnitude lower conductivity value viz., for L18n at 250 °C is $\sim 10^{-8}\ \Omega^{-1} cm^{-1}$ and for L18En is $\sim 10^{-9}\ \Omega^{-1} cm^{-1}$. This fall in conductivity is similar for samples with 2 mol% substitution of IL. Further addition of IL again decreases the conductivity by two orders of magnitude as evident in Fig. 4C.19.

Evidently, when the concentration of $LiNO_3$ is raised, an increase in conductivity is again noticed. Initial 1 mol% addition of IL in L18 composite shows a decrease in conductivity for L18En composite (Fig. 4C.19a). But, a further increase in conductivity has been noticed with an increase in Li^+ ion concentration. L33En composite exhibit a conductivity rise of ~2 - 3 orders of magnitude as compared to L18En composite (Table 4.7). Further, with an increase in Li^+ ion concentration in L40En and L46En composites of series 1, a marginal decrease in conductivity (a saturation in the conduction process) has been evident.

However, this rise in conductivity is saturated for further substitution of lithium salt. A possible explanation of this could be, availability of sufficient amount of available Li^+ ions/charge carriers that are required for promoting ion transfer that fills up the conduction pathways/channels thereby enhancing the conductivity. A reason for the initial decrease in conductivity of L18En composite is the deficiency of conducting ions, due to which the conduction channels created by IL remains deserted and are a major reason for the decrease in conductivity of the composites. With an increase in salt concentration, these channels are well occupied and help in the promotion of ion conduction through the available pathways.

In order to confirm the above-mentioned conductivity concept i.e. IL provides the conduction pathways in the solid matrix and makes these channels available to salt ions to

conduct through, a new series of silica gel composites were prepared as mentioned in series-3 (IL concentration constant to 3 mol% and varying $LiNO_3$ concentration). Electrical conductivity-temperature cycle for these composites exhibits an increase in conductivity. This rise for L46En (~10^{-6} $\Omega^{-1}cm^{-1}$) is noticed to be ~ 2 orders of magnitude higher than that of the L18n (~10^{-8} $\Omega^{-1}cm^{-1}$) composite at 548 K. While comparing with L18E3n (~10^{-9} $\Omega^{-1}cm^{-1}$) composite, this rise is found to be ~ 2 orders of magnitude for L40E3n composite (~10^{-7} Ω^{-1} cm^{-1}) at 548 K. Henceforth, it can be further correlated as there is a requirement of a sufficient amount of conducting ions (Li^+) in the presence of IL to make these composites ionic conducting in nature.

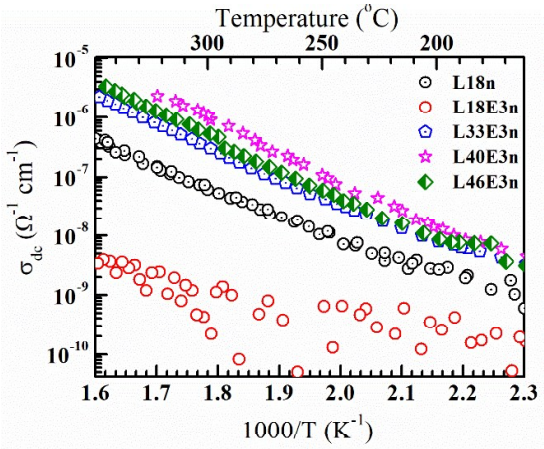

Fig. 4C.20 σ_{dc}-T cycle Series 3 composites.

Table 4.7 provides details about the variation in activation energy and conductivity for three different temperatures for the composites. For an increase in IL concentration (L18E7), a steep decrease in E_a for conduction has been noticed. For rest of the composites i.e. for IL = 1, 2, 3 and 7 mol%, only a small variation in E_a were observed. This decrease in E_a is marked for deserted conduction pathways that are created by IL into the glass matrix due to less concentration of conducting ion. On the other side, a decrease in conductivity of the samples has been noticed at ~250 °C for an increase in IL concentration. This decrease in conductivity of the samples is due to unavailability of sufficient amount of charge transferring ions to conduct. Fig. 4C.19a showed an effect on the increase in Li^+ ion concentration. With an increase in the concentration of Li^+ ion, both the conductivity as well as E_a required for ion conduction increases up to L26En composites and then it almost attains saturation. This rise in conductivity for composites up to L26E is due to the

availability of sufficient amount of conducting ions with the rise in Li^+ ions. For later composites, these samples attain saturation, as sufficient amount of ions are available in the conduction channels for ions transfer.

Table 4.7 Conductivity and activation energy of the composites of three different series.

Sample Code	Conductivity at 305 K	Conductivity at 523 K	Conductivity at 548 K	Activation energy (eV)
	($\Omega^{-1}cm^{-1}$)			
Series-1				
L18n	$1.3x10^{-8}$	$2.2x10^{-8}$	$5.5x10^{-8}$	0.82
L18En	$3.2x10^{-7}$	$4.5x10^{-9}$	$8.7x10^{-9}$	0.67
L26En	$1.4x10^{-6}$	$1.3x10^{-7}$	$4.1x10^{-7}$	0.99
L33En	$1.0x10^{-6}$	$4.0x10^{-6}$	$1.2x10^{-5}$	0.93
L40En	$4.6x10^{-7}$	$1.4x10^{-6}$	$4.4x10^{-6}$	0.97
L46En	$8.9x10^{-7}$	$1.8x10^{-6}$	$4.4x10^{-6}$	0.85
Series-2				
L18n	$1.3x10^{-8}$	$2.2x10^{-8}$	$5.5x10^{-8}$	0.82
L18En	$3.2x10^{-7}$	$4.5x10^{-9}$	$8.8x10^{-9}$	0.67
L18E2n	$1.3x10^{-8}$	$3.9x10^{-9}$	$7.8x10^{-9}$	0.73
L18E3n	$7.7x10^{-9}$	$6.6x10^{-10}$	$1.2x10^{-9}$	-NA-
L18E7n	$8.8x10^{-11}$	$6.6x10^{-10}$	$6.5x10^{-10}$	-NA-
Series-3				
L18E3n	$7.7x10^{-9}$	$6.6x10^{-10}$	$1.2x10^{-9}$	-NA-
L33E3n	$3.8x10^{-6}$	$9.1x10^{-8}$	$2.7x10^{-7}$	0.89
L40E3n	$9.3x10^{-7}$	$2.5x10^{-7}$	$8.1x10^{-7}$	1.00
L46E3n	$7.6x10^{-8}$	$1.2x10^{-7}$	$4.0x10^{-7}$	0.97

Variation in E_a and conductivity for glass composites with 3 mol% IL (with higher IL concentration) and then subsequently increasing $LiNO_3$ to 46 mol% has been shown in Fig. 4C.20. For these composites, a gradual increase in E_a has been observed for up to L40E3 composites and then it almost becomes constant for later composition. A similar trend has also been observed for the conductivity of these glass composites. This trend has been observed as with an increase in IL concentration there is the formation of a sufficient

amount of conduction channels and the availability of the reasonable amount of ions to promote conduction. Also these saturation in conductivity and activation energy may be due to the fact the network prepared through non-hydrolytic route is not able to hold the IL both beyond a temperature (300 ^{o}C) and beyond a composition value.

4C.4.3 Mechanism of electrical transport

Scaling behavior as explained in the previous section has been observed in the composites with composites of series-1 (Fig. 4C.21), and series-3 (Fig. 4C.22) with temperature variations. L26En, L33En, and L46En composites from series-1 exhibit good scaling behavior with temperature variation. Thus, it can be stated that the ion relaxation process in these composites is independent of temperature.

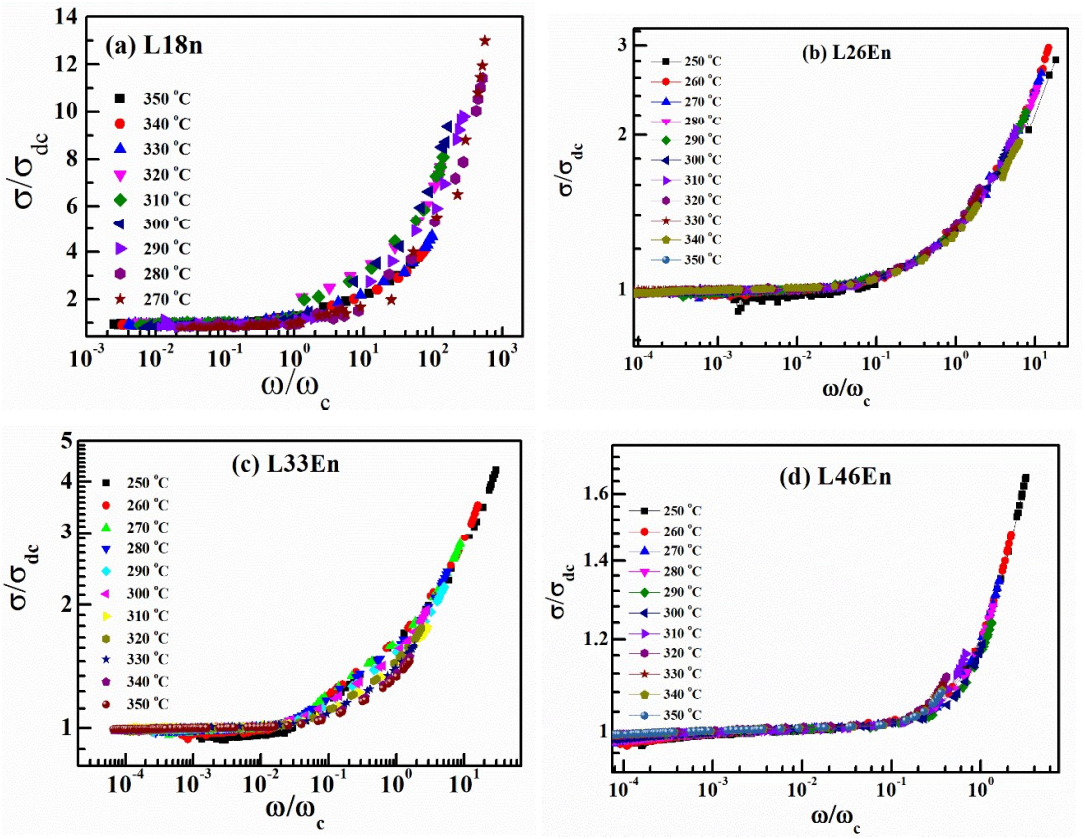

Fig. 4C. 21 Scaling behavior of conductivity for (a) L18n, (b) L26En, (c) L33En, and (d) L46En composites from series 1 with temperature variations.

Similarly, L33E3n, L40E3n and L46E3n composites of series 3, also exhibit a good scaling nature with temperature variations (Fig. 4C.22).

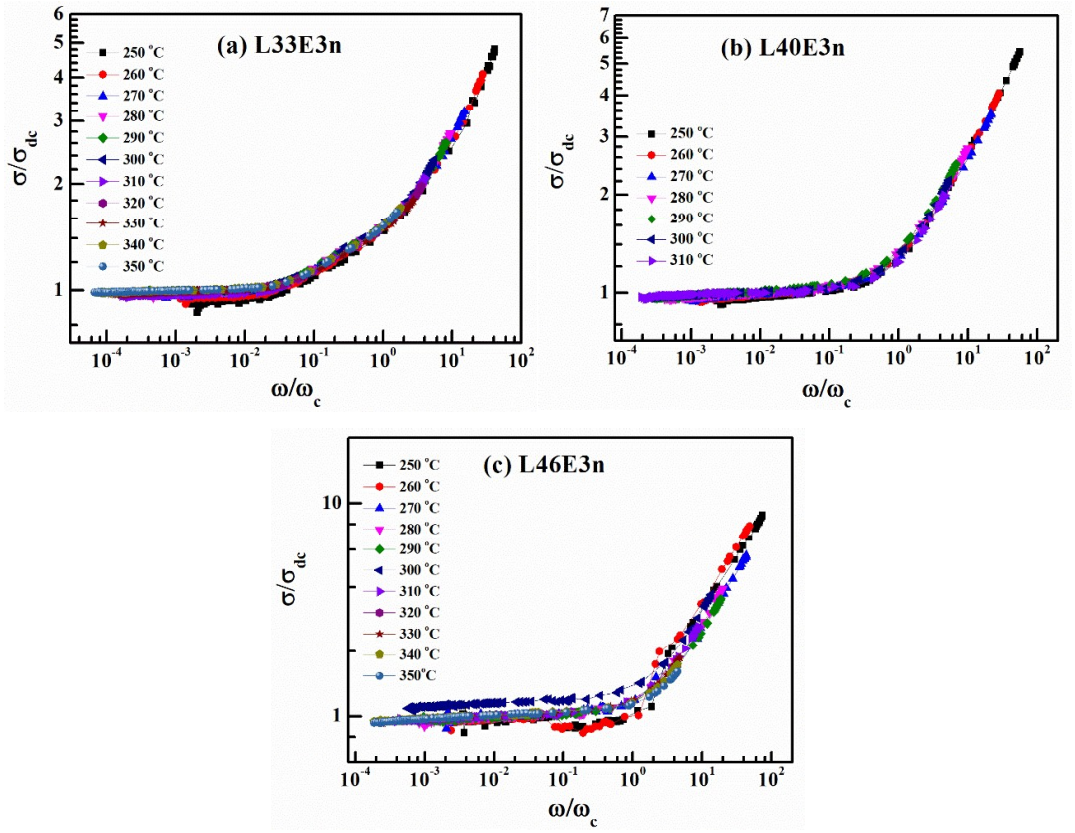

Fig. 4C.22 Scaling behavior of conductivity for (a) L33E3n, (b) L40E3n, and (c) L46E3n composites from series-3 with temperature variations.

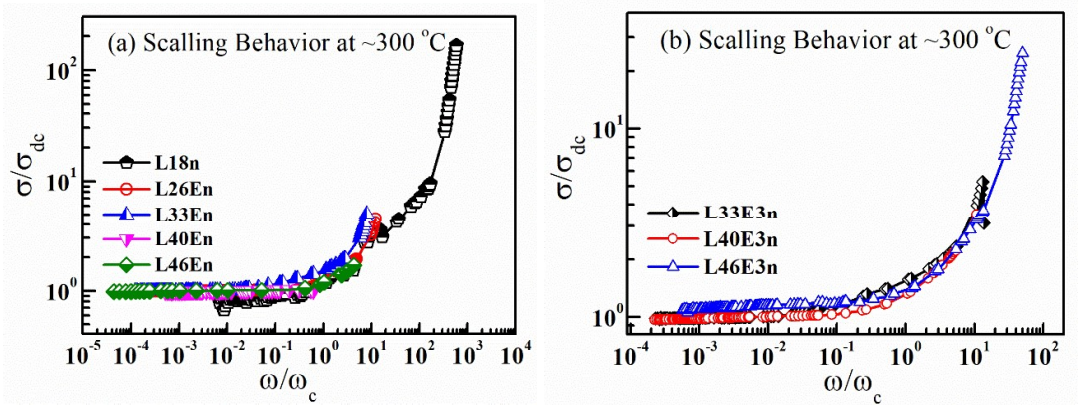

Fig. 4C.23 Scaling behavior of conductivity for (a) Series 1 and (b) Series 3 at ~300 °C.

The scaling behavior for compositional variation has also been analyzed and plotted at ~ 300 ^{o}C (Fig. 4C.23). It is evident from the plots that, for series 1 compositions (Fig. 4C.23a), the ion transfer process is different for L18n composite as compared to other composites containing 1 mol% of IL (L26En, L33En, L40En, and L46En). A similar trend of scaling behavior for the compositions of series 3 has also been noticed (Fig. 4D.24). From these scaling plots of different compositions at 300 ^{o}C suggests for the presence of a similar process of ion relaxation. But, for L18n composite the ion relaxation process seems different.

4C.5 Conclusions

Some of the conclusions are:

1. The silica gel composites prepared through non-hydrolytic process are widely amorphous in nature.
2. From IR we understand the formic acid exists in ionized form in the inner pores of the network.
3. DTA and TGA indicate the removal of IL from the network at 300 ^{o}C.
4. These composites exhibit reduced conductivity (of at least one order of magnitude) as compared to their corresponding hydrolytic sol-gel processed composites and this may be due to the instability of IL in the system as indicated by thermal studies. Also the conductivity decrease may be due to complex formation of Lithium ion with the ionized formic acid (formate ion).
5. From the Nyquist plots and other studies we could see the ionic conduction is suppressed as compared to the hydrolytic-route samples. However, with increasing concentration of salt ions (lithium ion) ionic conductivity increases.
6. There is no specific effect of IL on the conductivity of the samples as the IL is not thermally stable in the composite. In some cases it is clear that additional confinement of IL reduces the conductivity.

System 4D

[BMIM] Br Confined Lithium Silicate Gel Composites Prepared by Hydrolytic Sol-Gel Process and the Effect of Heavy Metal Ion Substitution

4D.1 Composition

In continuation of the work in the previous three sections here we report the confinement of a new IL i.e. [BMIM]Br, and Li^+ ion (from the salt LiCl) in silica gel composites prepared by hydrolytic sol-gel process. The homogeneous sol formed was solidified at room temperature to form a densified gel composite. Later, it was dried initially at 50 ^oC for a couple of days and then further air-dried at 150 ^oC for several days to obtain densified amorphous composites (Fig. 4D.1 and 4D.2).

The present system focuses on these two series viz., $xLiCl\text{-}IL\text{-}CuCl_2\text{-}(98\text{-}x)SiO_2$, $10LiCl\text{-}yIL\text{-}CuCl_2\text{-}(89\text{-}y)SiO_2$ and were prepared for different x and y so that x = 10, 20, 25 and 30 mol% and y = 0, 1, 2 and 4 mol% (Table 4.8). Further, in some of the composites of the first series, to explore the effect of the heavy metal substitution, 10 mol% Pb was introduced in place of SiO_2. $CuCl_2$ has been added into the system to use Cu^{2+} as an electron paramagnetic resonance (EPR) probe, to explore and to find out the microstructure distributions as reported earlier for lead oxide-lead halide glasses [36-37] and to correlate the EPR parameter distributions thus obtained with the observed conductivity properties. The hydrolysis of TEOS followed by condensation is done in acidic medium and ethanol (TEOS: H_3O^+: EtOH - 1: 4: 10). After the formation of homogeneous sol, IL, LiCl, $Pb(NO_3)_2$ and $CuCl_2$ were added subsequently.

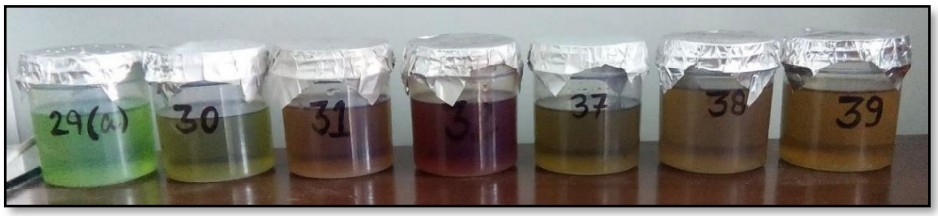

Fig. 4D.1 Photographic images at 1x magnification for homogeneous sol kept at the ambient condition for the formation of a solidified gel.

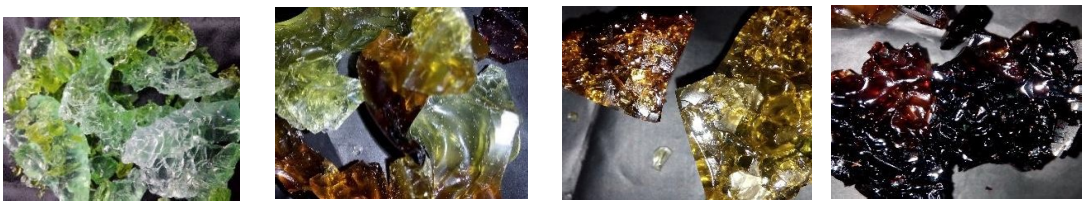

Fig. 4D.2 Photographic images (magnification 1X) of gel composites (from left to right the pictures correspond to 10L, 10LB, 10L2B, 10L4B).

Table 4.8: Compositions of the samples: Sample codes have been used as abbreviations for compositions in the text.

Sample Code	Mol %					Density (g cm^{-3})	Molar Volume (cm^3 mol^{-1})		Conductivity at 523 K (Ω^{-1} cm^{-1})
	LiCl	[BMIM] Br (IL)	$CuCl_2$	$Pb(NO_3)_2$	SiO_2	Experimental	Calculated*	Experimental	
Series-1 - Increase in LiCl Concentration									
L10	10	0	1	0	89	1.813	22.71	32.57	6.99×10^{-10}
L10B	10	1	1	0	88	1.787	23.42	33.94	6.99×10^{-10}
L20B	20	1	1	0	78	2.018	23.27	29.18	2.47×10^{-8}
L25B	25	1	1	0	73	1.964	23.20	29.53	2.93×10^{-7}
L30B	30	1	1	0	68	1.841	23.12	31.02	4.71×10^{-7}
Series-2 - Increase in [BMIM] Br Concentration									
L10	10	0	1	0	89	1.813	22.71	32.57	6.99×10^{-10}
L10B	10	1	1	0	88	1.787	23.42	33.94	6.99×10^{-10}
L10B2	10	2	1	0	87	1.848	24.22	33.68	8.01×10^{-10}
L10B4	10	4	1	0	85	2.177	25.65	30.05	8.01×10^{-10}
Series-3 - Increase in LiCl Concentration with 10 mol % of Pb									
L10P	10	0	1	10	79	2.087	30.89	41.29	7.82×10^{-10}
L10PB	10	1	1	10	78	2.375	31.68	36.95	7.82×10^{-10}
L20PB	20	1	1	10	68	2.386	31.61	36.04	6.15×10^{-8}
L25PB	25	1	1	10	63	1.803	31.64	47.20	3.87×10^{-7}

Superscript * denotes based on the densities of the pure components

4D.2 Structural Studies

4D.2.1 Molar Volume

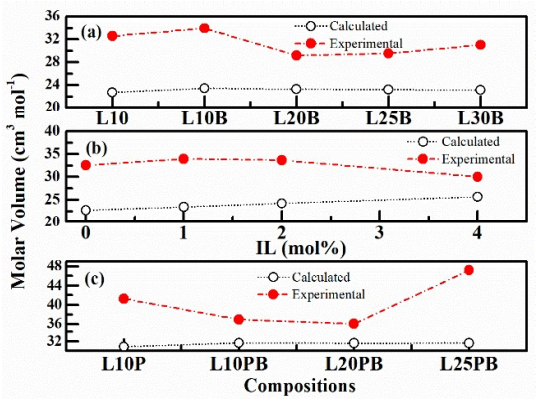

Fig. 4D.3. Molar volumes of the composites (a) series-1, (b) series-2 and (c)series-3 (with error limits of ±0.05 cm^3 mol^{-1}).

Experimental density values are specific for each sample. Molar volumes of samples in all three series of composites are apparently higher than the theoretically expected values,

indicating that in the amorphous structures there are substantial voids. No specific trend was verified in molar volume with respect to composition (Fig. 4D.3).

4D.2.2 Powder X-Ray Diffraction

Halo patterns (Fig. 4D.4) for the prepared samples confirm their amorphous nature in a wider range of compositions. For incorporation of IL up to 4 mol%, IL addition does not lead to formation/precipitation of any compound or crystallization of the gel composite even after drying. As evident from the plots, the presence of chloride ions from LiCl and $CuCl_2$ does not lead to any phase separation/crystallization.

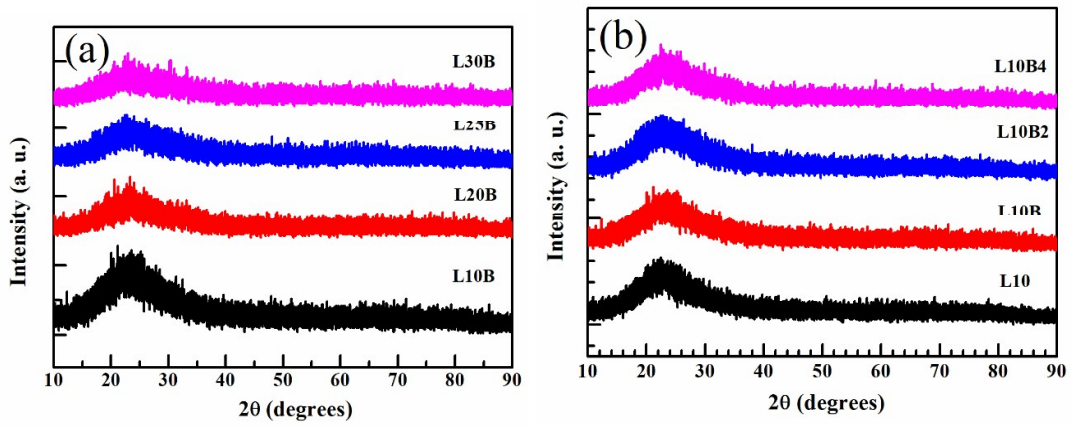

Fig. 4D.4 Fig. 3 Powder X-ray Diffraction (PXRD) patterns of the as prepared composites of (a) series-1 and (b) series-2.

4D.2.3 Electron Paramagnetic Resonance Spectroscopy

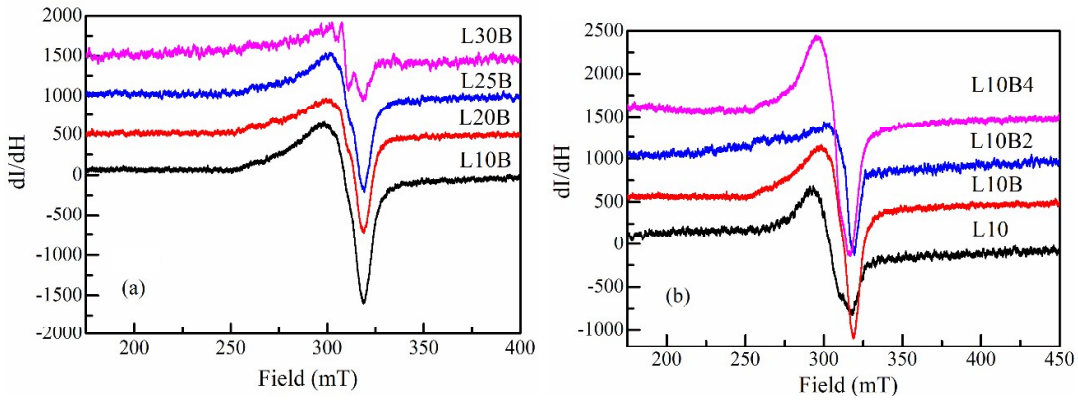

Fig. 4D.5 X-band (a) increasing IL concentration (b) Increasing LiCl concentration.

From the EPR spectra of the composites the following points may be concluded: (i) Cu^{2+} ion is a fluidic environment and having fast dynamic movements as the spectrum is almost isotropic and the line is broad and hyperfine splittings are seen only in low Li^{+} concentration case. (ii) The spectral lines are broadened with increasing concentrations of both lithium ion and IL. Even though the cupric ion concentration is maintained the same in all these composites, when the sites available for cupric ion attachment are getting reduced these are forced to occupy the nearby sites thus increasing the dipolar broadening. (iii) At higher concentrations of lithium ion we see the spectrum is made of two isotropic spectra. Thus the cupric ion even though in an isotropic environment is present in two different environments (case of L30B). By inference we can extend the conclusion that lithium ion may also be present in similar environment. (iv) We could record only the room temperature (RT) or lower temperature (LNT) EPR spectra of the samples. Thus we cannot correlate this distribution to the high temperature conductivity variation with respect to composition in our samples.

4D.2.4 FTIR Spectroscopy

FTIR spectra were recorded in attenuated total reflection (ATR) mode with an undiluted sample as well as in transmission mode with the sample in dry KBr. While the normal transmission mode spectra (Fig. 4D.7) correspond to the absorption by the bulk of the sample, in the ATR mode (Fig. 4D.6), IR attenuation (absorption) happens up to ~ 5 μm depth that may provide the surface information. We observe, interesting changes between the spectra of the samples obtained in these two modes.

The sample preparation is done in aqueous media and ethanol comes out as a product. As evidenced in literature [38], the solvent molecules (water and ethanol) are physisorbed as well as chemisorbed respectively in the ultra porous gel structure and the surface of the composite. Interestingly, complete elimination of the solvents takes place above 800 ^{o}C, but the liberation of water/ethanol from the matrix up to 400 ^{o}C is reversible. Since these samples were heat-treated at 150 ^{o}C, the unbound water along with some physisorbed water would have been eliminated at that stage. However, due to the reversal of physisorption process, the water/ethanol absorptions are likely to be observed.

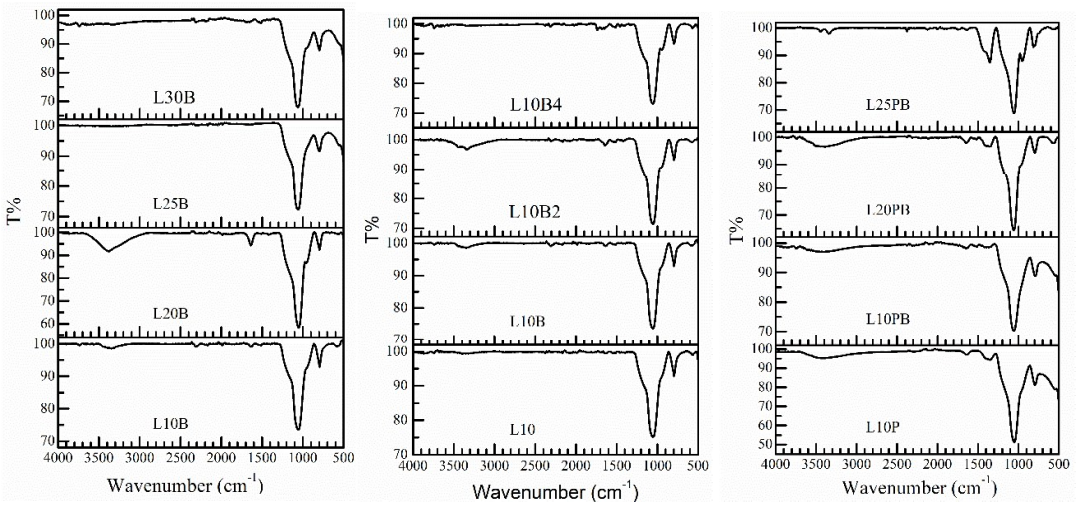

Fig. 4D.6 FTIR spectrum of the composites in the ATR mode (a) series-1, (b)series-2 and (c) series-3.

Comparing the Figures 4D.6 and 4D.7, the peaks corresponding to water and ethanol emerges strongly in transmission mode. Stretching vibration of hydrogen-bonded -OH (ν_{OH}) broad peak at 3500 cm^{-1}, bending vibrations of water (δ_{OH}) at 1600 cm^{-1} and bending vibrations of -CH_2-(δ_{CH2}) at 1400 cm^{-1}, indicates for the major amount of water/ethanol being present in the physisorbed form in the porous gel structure, and not at the surface.

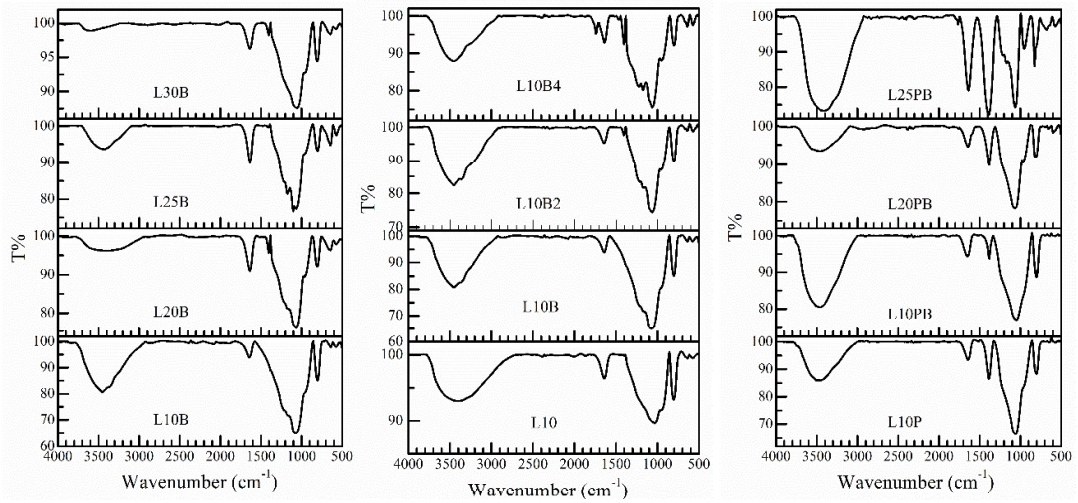

Fig. 4D.7 FTIR spectrum of the composites in normal transmission mode (a) series11, (b) series-2 and (c) series33. Samples were in dry KBr matrix during the measurement.

Other absorptions present are (and identified as): 825 cm^{-1} (Si-O-Si symmetric stretching), and 1072 cm^{-1} broad peak with a shoulder at 1188 cm^{-1} (Si-O-Si asymmetric stretching). Composites made with and without IL, yield similar IR spectra (compare 10L with 10LB

and 10LP with 10LPB). We are not observing any absorption exclusively due to IL in the spectra. For the IL ([BMIM]Br), some major absorptions are [63]: 3172 cm^{-1} (asymmetric stretching of ring HCCH), 1576 cm^{-1} (H_3C-N, H_2C-N stretching and ring in-plane asymmetric stretching), 839, 842, 847 cm^{-1} (ring HCCH asymmetric bending). Since the mol% of IL is low in our compositions these peaks may be of low intensity or merged with the other peaks observed in the region. However, the inclusion of IL in the composite is confirmed by SEM-EDS experiment as discussed further.

The 1400 cm^{-1} peak has been assigned to bending vibrations of -CH_2-(δ_{CH2}); however, at the same position nitrate ions also show a strong absorption. As Pb was introduced in the system through the precursor $Pb(NO_3)_2$. Thus, in series-3 the 1400 cm^{-1} peak is rather strong indicating the presence of nitrate ions in such systems.

4D.2.5 Field Emission Scanning Electron Microscopy

Morphology of the gel composites has been analyzed through FESEM analysis at 500 nm scale. The analysis showed homogeneity within their solid matrix (Fig. 4D.8 and Fig. 4D.9). It is also evident that with an increase in the concentration of Li^+ and [BMIM]Br, there is an increase in surface pore sizes which is reflected in their surface morphologies.

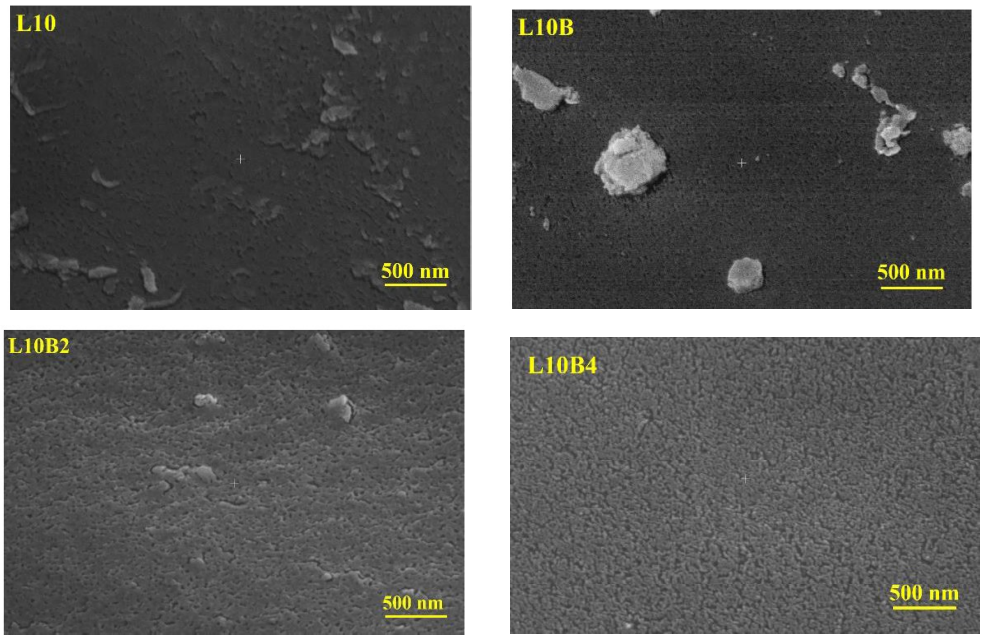

Fig. 4D.8 FESEM images of (a) L10, (b) L10B, (c) L10B2 and (d) L10B4 samples

IL containing samples (L10B, L10B2, and L10B4) are found to be more homogeneous in nature as compared to only salt-containing (L) composite. The major difference which can be observed from the FESEM pattern is the increase in the size of the pore/channels with an increase in IL concentration (Fig. 4D.8). These patterns are uniformly seen in different recordings of the sample.

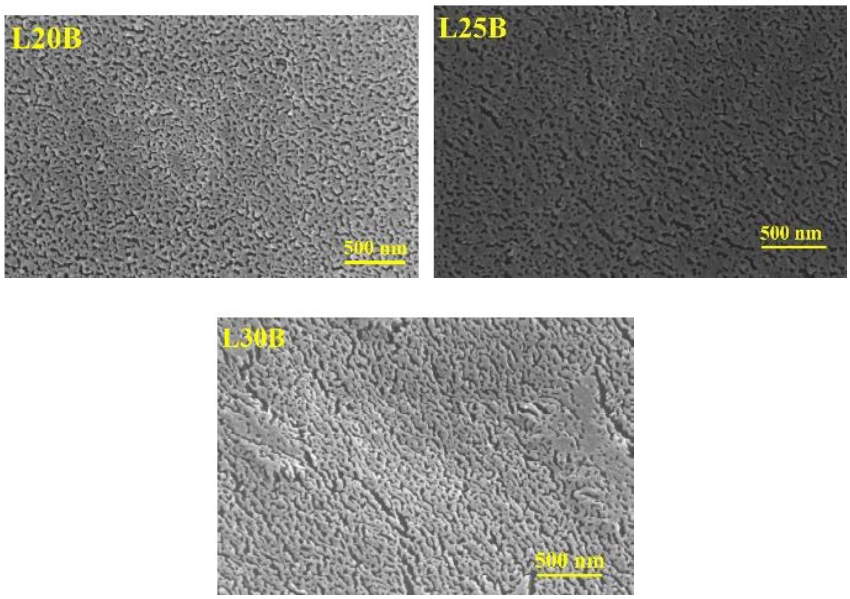

Fig. 4D.9 FESEM images of (left) L20B, (center) L25B, and (right) L30B samples

The homogeneous distribution of constituent elements in these composites was further deduced from the elemental (EDS) mapping at ~1μm scale (Fig. 4D.10 and 4D.11 - shown for only 30LB composite).

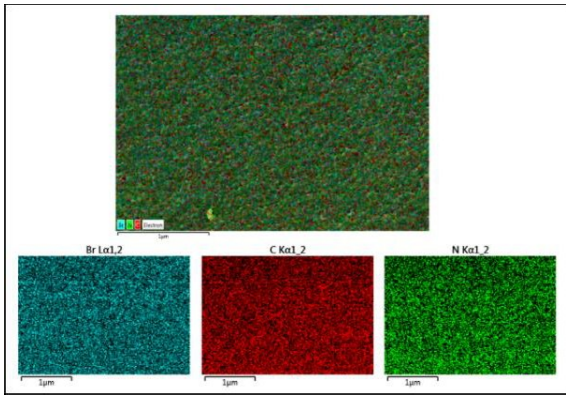

Fig. 4D.10 EDS mapping for L30B composite prior to conductivity-temperature cycles.

The homogeneous distribution of IL elements (C, N, and Br) is clearly evident that suggests the presence of IL in the matrix. Even though carbon can be from the ethanol trapped, noticeable traces of nitrogen and bromine are exclusively from IL in this case. The elemental analysis on the composites was again performed after several (at least three) successive conductivity-temperature cycles up to 300 ^{o}C, the presence of IL in the solid composite is again noticed. Similar trends were observed for other IL containing samples as well. It is interesting to note that the N and Br peaks (though weak due to low IL content) are evident in the ED spectra (Fig. 4D.12) for a sample containing IL.

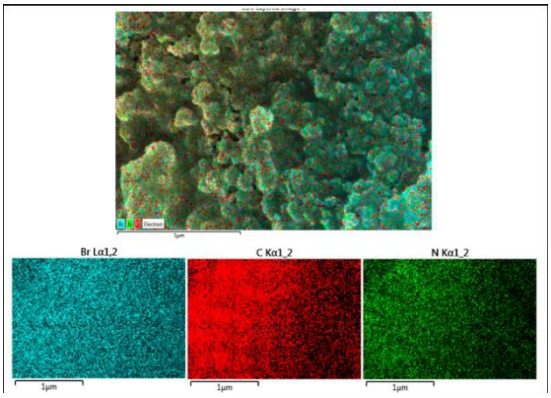

Fig. 4D.11 EDS mapping for the fractured surface of L30B composite pellet. Measurements were done after a conductivity cycle (30 – 300 ^{o}C).

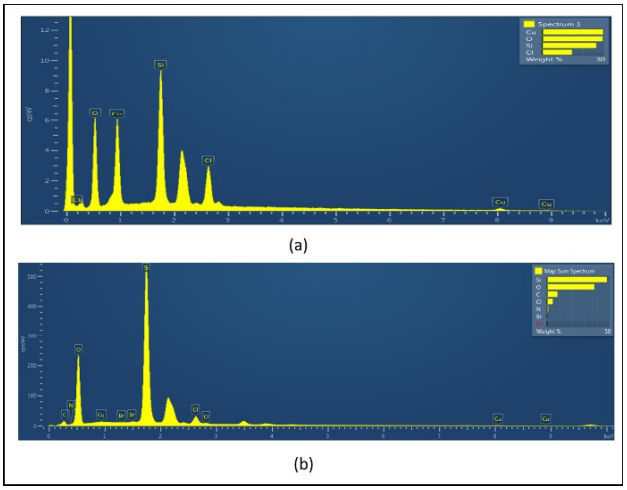

Fig. 4D.12 ED Spectra of samples (a) L10 and (b) L10B.

The elemental analysis has also been performed on the composites after conductivity measurements (at least after 3 cycles), where the samples were heated up to ~300 ^{o}C. The

presence of IL in the solid composite is again seen, even after high-temperature conductivity measurements (i.e. cycling between 100 - 250 ^{o}C).

4D.3 Thermal Analysis

4D.3.1 Differential Thermal Analysis

DTA scans of the samples (Series 1 and 2) have been taken in a temperature range of 35 to 350 °C with the heating rate of 10 °C/minute in a nitrogen atmosphere (Fig. 4D.13).

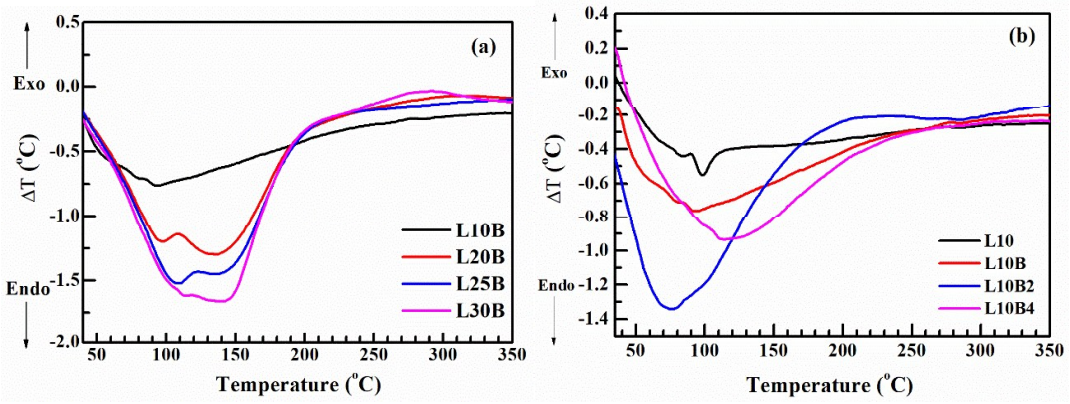

Fig. 4D.13 DTA scans of the as prepared gel composites (a) series 1 and (b) series 2.

The dehydration processes in the silicate gel networks prepared through the sol-gel process have been well summarized in a review by Hench and West [38]. Here we should interpret the word "dehydration" to include removal of ethanol also. There are two kinds of water present in the sol-gel system. The physisorbed water present in the ultra porous gel structure and the chemisorbed water on the gel surface in the form of silanol moieties. In the heating process, up to 170 ^{o}C only the physisorbed water is eliminated. Between 170 and 400 ^{o}C the surface chemisorbed water is eliminated reversibly and above 400 ^{o}C irreversible elimination of surface water along with structural changes happens. The presence of IL in our systems may change these temperatures to a certain extent. Thus, the DTA plots are of a similar pattern when the IL mole fraction is maintained at the same value (Fig. 4D.13a) and large variations are seen when IL fraction is varied (Fig. 4D.13b). In Fig 4D.13a, the broad endothermic peaks in the range of 70 - 170 °C are due to the elimination of solvents (water and ethanol) trapped in the system by physisorption in the ultra porous gel structure. Except for continuous solvent elimination, which is reversible, we do not observe any thermal event in the temp range 170 - 350 °C for most of the

composites; therefore, all our conductivity measurements are focused in this temperature range.

4D.3.2 Thermogravimetric Analysis

TGA scan for pristine IL [BMIM] Br has been discussed in the inset of Fig. 4D.14.

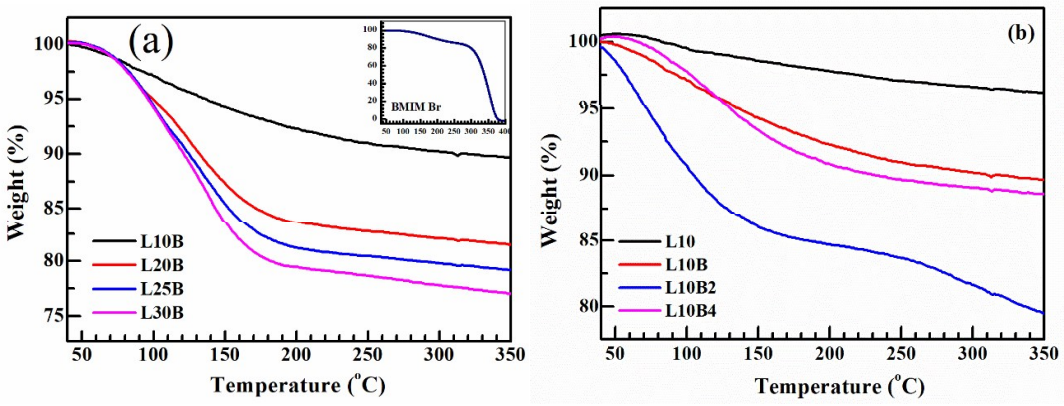

Fig. 4D.14 TGA scan of the as prepared gel composites (a) series 1 and (b) series 2. Inset of Fig.: TGA for pure ionic liquid.

The TGA plots are in accordance with DTA results. TGA of pure IL [BMIM]Br is shown as an inset. The IL starts decomposing at ~275 °C. This decomposition is not seen in DTA as well as in TGA. Thus in the temperature range, 170 - 350 °C IL is not eliminated from the composites. Weight loss of 20% observed near 70 - 170 °C, corresponds to the loss of water-ethanol mixture (solvent) trapped in the matrix by physisorption in the ultra porous gel structure. Similar to what is seen in DTA, the TGA plots are of a similar pattern when the IL mole fraction is maintained at the same value (Fig. 4D.14a) and large variations are seen when IL fraction is varied (Fig. 4D.14b). The minimal weight loss seen above 170 °C in a gradual manner corresponds to the elimination of surface chemisorbed hydroxyl and ethoxy groups in the form of water and ethanol which is reversible. In both series 1 and 2, we find there is not much solvent elimination when Li content is only 10 mol%.

4D.4 Electrical Transport

4D.4.1 Impedance Spectroscopy

Firstly, The Effect of confinement of IL [BMIM] Br on to the structure and electrical properties of the gel matrix (Series-1 and Series-2) was explored in the temperature range of thermal stability (~150 - 250 ^{o}C as defined by TGA and DTA). Fig. 4D.15a and 4D.15b

show the Nyquist plots obtained at various temperatures for two of the composites with (a) 25 mol% and (b) 30 mol% of LiCl content (series-1). As apparent, depressed semicircles are observed that suggests non-Debye type nature of these samples. A typical tail/spur at lower frequencies, characteristic feature of ionic transport, is though missing. Since both of these compositions contain a significant amount of LiCl, ionic conduction was expected. Thus, dc polarization studies were separately performed to analyze electronic transport (inset of Fig. 4D.15a and 4D.15b). Polarization behavior thus confirms predominant ionic transport in both the samples.

From similar measurements, Nyquist plots were obtained for samples with various LiCl contents. For all the other samples, the conductivity was obtained from the diameter of the semicircles (as shown in Fig. 4D.17) except for samples with low LiCl content. In these, due to very high resistivity, semicircles were not visible. Thus, the conductivity at 1 kHz was considered as the dc conductivity that lies at the plateau region of σ-ω plots. (as shown in Fig. 4D.16).

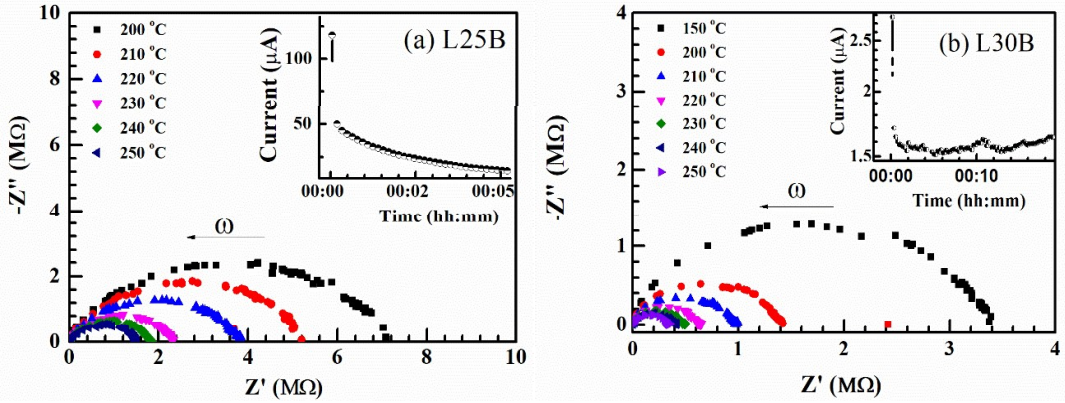

Fig. 4D.15 (a) Nyquist plots for L25B composite, and **(b)** Nyquist plots for L30B composite. Inset: Transient current obtained during dc polarization measurement. Rapid fall in the current followed by a saturation confirms ionic nature of these samples.

The electrical conductivity of the composites has been analyzed and understood by plotting conductivity (σ′) as a function of frequency (ω) (Fig. 4D.16). Conductivity plot exhibits a plateau region in the low-frequency domain followed by dispersion region in the high-frequency domain. An increase in plateau region in a wide frequency range with an increase in Li^+ ion concentration have been further noticed, this remarks for the increase in conductivity of the samples with an increase in Li^+ ion concentration. Plateau region

helps in determining σ_{dc} for the gel composites which is independent of frequency change. Electrical conductivity (σ_{dc}) of the composites have been further explored and understood as a variation in temperature (Fig. 4D.17).

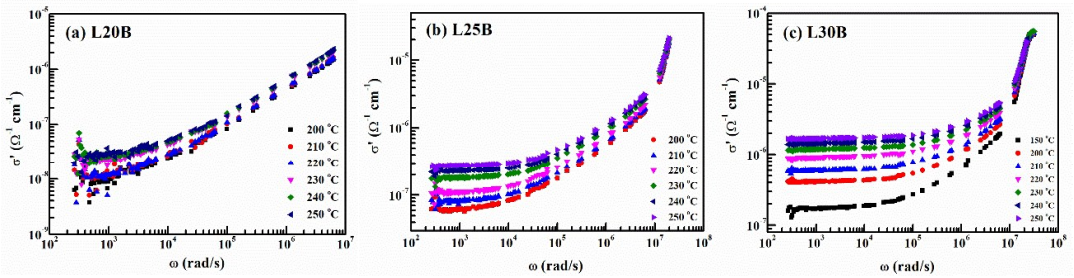

Fig. 4D.16 log σ′ as a function of frequency (ω) for (a) L20B, (b) L25B and (c) L30B with the increase in temperature.

4D.4.2 Conductivity cycles

The σ-T behavior was studied in the thermally stable region (as revealed from DTA and TGA plots). Thus, Fig. 4D.17 shows the temperature dependence of electrical conductivity of two different series of samples. In Fig. 4D.17b, the conductivity is plotted for the samples with a fixed salt content of 10 mol%, and the IL content was gradually increased (from 1-4 mol%). As evident, the conductivity does not show any specific trend, or even thermally activated behavior. This readily suggests that due to large potential barriers IL ions hardly contribute to the conductivity.

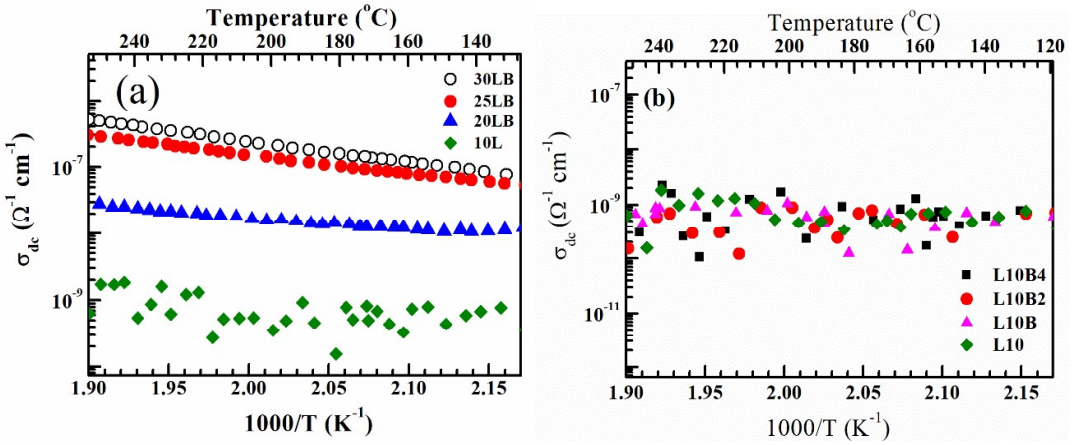

Fig. 4D.17 (a) Temperature dependence of dc conductivity for increasing LiCl content with fixed IL (1 mol%), and (b) Temperature dependence of dc conductivity for samples with increasing IL concentration and fixed salt content of 10 mol%,

On the other hand, a very interesting trend in the conductivity was observed when IL content is fixed to a low value of 1 mol% and the salt content is gradually increased (Fig. 4D.17a). Evidently, for significantly larger salt content (i.e. 20-30 mol% of LiCl) conductivity exhibits ~ 2-3 orders of magnitude rise along with an Arrhenius behavior with the low activation energy of ~ 0.6-0.7 eV. This result suggests that the salt ions dissolved in the matrix contributed to the electrical conductivity and also to thermally activated electrical transport.

Table 4.9: Electrical properties of the composites.

Sample Code	Conductivity at 313 K (Ω^{-1} cm^{-1})	Conductivity at 473K (Ω^{-1} cm^{-1})	Activation energy (eV)
Increasing IL concentration			
L**10**	8.46 x 10^{-9}	5.65 x 10^{-10}	0.24
L10B	8.46 x 10^{-9}	5.65 x 10^{-10}	0.34
L10B2	1.87 x 10^{-5}	5.65 x 10^{-10}	0.04
L10B4	4.73 x 10^{-10}	8.97 x 10^{-10}	0.07
Increasing LiCl Concentration			
L10B	8.46 x 10^{-9}	5.65 x 10^{-10}	0.34
L20B	5.84 x 10^{-5}	1.08 x 10^{-8}	0.38
L25B	5.84 x 10^{-8}	5.98 x 10^{-8}	0.57
L30B	1.38 x 10^{-7}	8.82 x 10^{-8}	0.63

It is interesting to note that the confinement of IL (at higher mol%) does not lead to an improvement in conductivity. It has been observed by others, that addition of lithium salts such as LiCl to ILs increases the viscosity [30]. Due to this, the mobility of ions of IL and Li^+ both will be reduced. However, the effect will be more on the ions of IL and Li^+ becomes the major conducting species. Thus, high salt content in the presence of a small amount of IL does lead to (i) a systematic temperature dependence, and (ii) significant enhancement of conductivity.

It was also important to understand the behavior of electrical transport near room temperature. Thus, for the two of the samples with high Li^+ ion content, the σ-T behavior is shown in Fig. 4D.18. The conductivity exhibits an almost linear rise with low activation energy (0.5 – 0.6 eV). The sample with high Li^+ ion content (L30B) apparently exhibits better conductivity. However, above this range of temperature, measurements were avoided in view of various thermal events (as observed in thermal studies). Nevertheless,

the ionic conductivity for such poor ionic system is seen to exhibit a notable rise with the addition of a very small amount of IL (1 mol %).

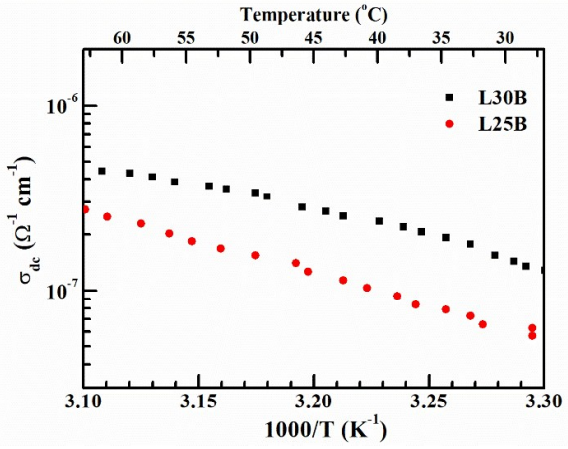

Fig. 4D.18 Temperature dependence of dc conductivity for L25B and L30B at ambient temperatures.

4D.4.3 Ion Transport Mechanism

The effect of compositional alterations and temperature on electrical transport is again examined using conductivity relaxation. Electrical transport mechanism of the prepared IL-based gel composites can also be understood via well known Jonscher Power Law (JPL) behavior described in many studies on ionic systems [52-53] as well as disordered non-metals [54-56, 64]. The JPL behavior, also known as the universal dynamic response (UDR) deals with frequency dependence of conductivity. The conductivity relaxation process helps in understanding the mobile ion dynamics in solids. The scaling behavior [51-57, 64] can be examined using the characteristic frequency (ω_c) and conductivity (σ_{dc}), according to the following relation:

$$\frac{\sigma}{\sigma_{dc}} = F\left(\frac{\omega}{\omega_c}\right) \quad (1)$$

The frequency dependence of conductivity viz. σ-ω plots have been scaled using σ_{dc} and ω_c that is the characteristic crossover frequency obtained from the onset point of dc to the dispersion region. If all the measured data falls on a single master curve according to equation (1), then it is because of the similar process of charge transfer, hence conductivity mechanism i.e. ion-relaxation process.

Thus, σ/σ_{dc} versus ω/ω_c plots for two best-conducting composites have been plotted for different temperatures (Fig. 4D.19). Plot gives two different types of regions within the measured frequency range, (i) plateau region at low frequencies and (ii) dispersion region at high frequencies. Former gives information about frequency-independent conductivity (σ_{dc}) due to the long-range diffusive motion of ions, whereas the latter infers about the short-range motions of ions within the bulk.

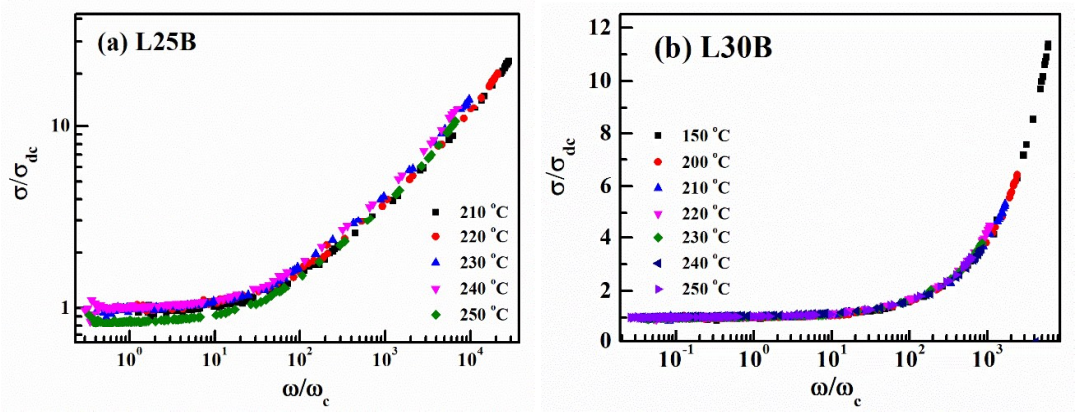

Fig. 4D.19 Scaling behavior of conductivity for L25B and L30B composites with temperature variation.

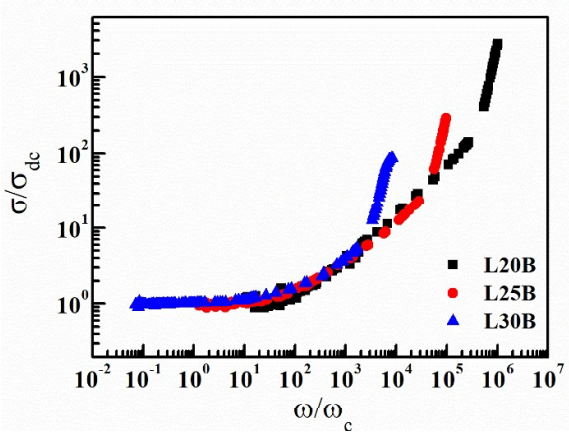

Fig. 4D.20 The scaling behavior with composition variation. Scaling is missing in compositional variation.

As evident, with temperature variation, a good scaling behavior is noticed in an appreciably wider frequency range. This clearly indicates that the mechanism of ion transfer remains unchanged with temperature variations. This result indeed compliments DTA/TGA analysis that suggests appreciable thermal stability in this temperature range.

Fig. 4D.20 shows σ/σ_{dc} versus ω/ω_c plot with compositional variation at a fixed temperature of 210 °C. Apparently, scaling behavior is not evident. Thus, the concentration of salt ions (mainly mobile Li^+) play a significant role in electrical transport and mechanism is governed by compositional changes in the matrix.

4D.5 Effect of Heavy Metal (Pb^{+2}) Ion Substitution

Fig. 4D.21 The photographic image at 1x magnification (a) Homogeneous sol of the composition (b) Prepared (solid) gel after annealing at 150 °C.

In view of further understanding of the effect of IL addition, the composition of the series-1 was altered by introducing Pb^{+2} ions in the matrix (Series-3). Up to 25 mol% LiCl could be dissolved in the gel matrix in presence of Pb^{+2} ions. It has been reported elsewhere, that because of bigger ion size such substitutions may lead to an increase in molar volume and consequently increase in the free volume of gel matrix [57]. From Table 4.8 it is clearly suggestive that the molar volumes of Pb containing samples are more compared to the corresponding samples of series-1. Interestingly, the addition of Pb^{+2} (through precursor $Pb(NO_3)_2$) in the matrix leads to better ionic mobility which is evident from the Nyquist plots where the tail (attributed to the polarization of ions) at lower frequencies is visible (discussed later).

Although, two series of compositions viz., xIL-(79-x)(SiO_2)-10$Pb(NO_3)_2$-1$CuCl_2$-10LiCl and yLiCl-(88-y)(SiO_2)-10$Pb(NO_3)_2$-1$CuCl_2$-1IL were prepared for different values of IL ([Bmim]Br) and LiCl. Different concentrations of x and y were used, where x = 0, 1, 2, 4 and 8 mol% and y = 0, 10, 15, 20 and 25 mol%. These gel composites have been prepared via hydrolytic sol-gel process. However, Electrical transport properties have been studied and explored thoroughly only for the composites given in Table 4.8 (series-3).

4D.5.1 Heavy Metal (Pb^{2+}) Substitution: Structure and Electrical Properties Study

4D.5.1.1 Powder X-ray Diffraction

PXRD patterns (Fig. 4D.22) were obtained for all the prepared compositions and their halo pattern suggests for these samples to be of amorphous nature in a wide range of composition. The amorphous network of these gel composites has not been disturbed by IL addition. Although the presence of lead into the system makes it, a little complicated.

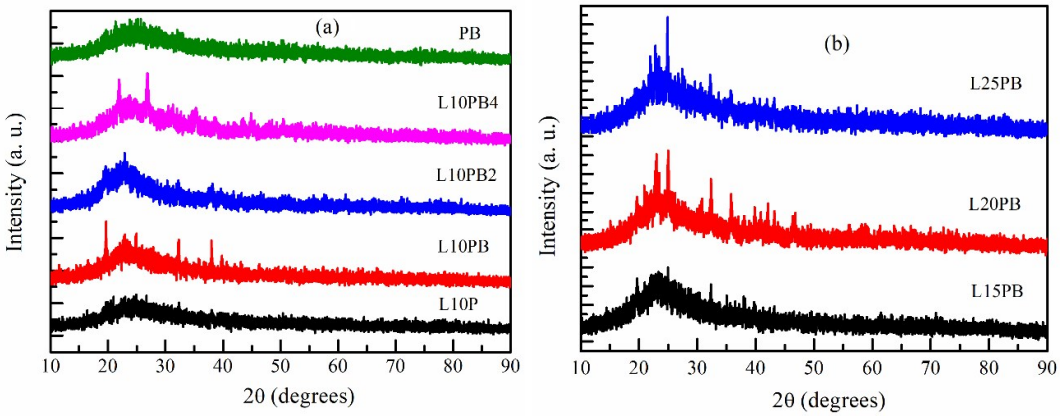

Fig. 4D.22 PXRD pattern of sol-gel synthesized amorphous composites.

4D.5.1.2 Differential Thermal Analysis

DTA scans of the prepared gel composites were taken in the temperature range of 35 to 350 °C with a heating rate of 10 °C/minute under nitrogen atmosphere (Fig. 4D.23). First endothermic dip in a temperature range of ~70 - 100 °C corresponds to water and organic residues from the gel matrix. Their residues are trapped within the matrix at the time of condensation or annealing of these composites. Apart from this, these composites are thermally stable in a wide temperature range of ~150 - 300 °C (Fig. 4D.23a and 4D.23b). Thermally stable region of the composites has been used for determining the conductivity and other properties of the gel composites. The IL [BMIM]Br has the decomposition temperature at around 273 °C [65]. The exothermic peaks seen at 210 - 280 °C are due to this decomposition and this is seen only in some Pb containing samples. In samples without Pb the IL is preserved in the temperature range of conductivity measurements (350 °C).

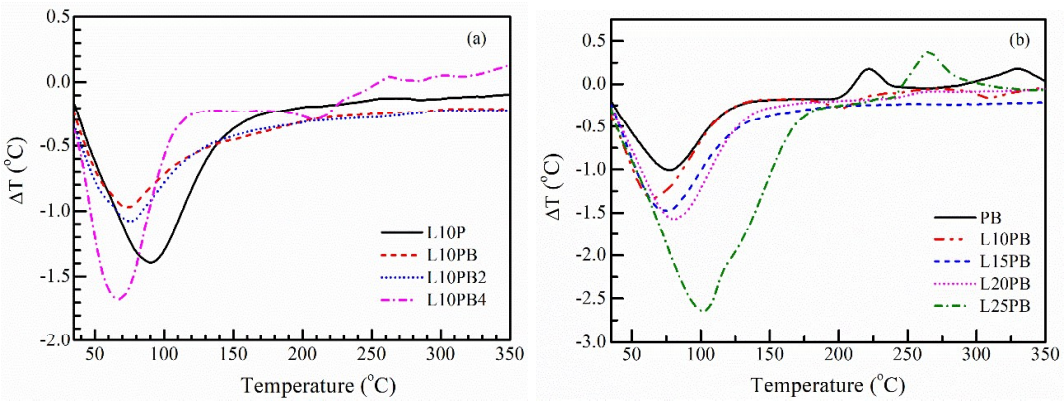

Fig. 4D.23 DTA of gel composites (a) increasing IL concentration and (b) increasing LiCl concentration.

4D.5.1.3 Thermogravimetric Analysis

TGA scan of pristine [BMIM] Br has been shown in the inset of Fig. 4D.24b, from the figure it can be clearly observed that there is a phase transformation in IL at approximately 200 °C and then it starts decomposing ~300 °C.

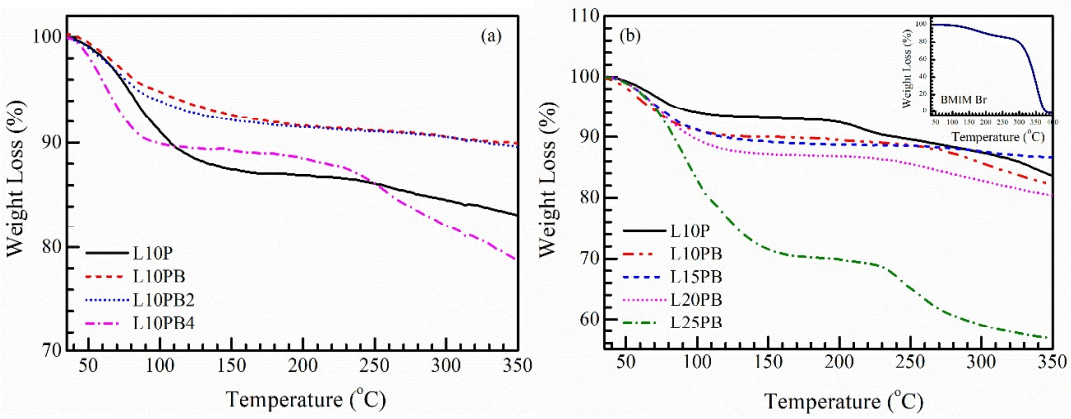

Fig. 4D.24 TGA of gel composites (a) increasing IL concentration and (b) increasing LiCl concentration. TGA of Pristine [BMIM]Br is shown in the inset.

Interestingly, the prepared gel composites exhibit a weight loss near 100 °C, that may again be attributed to the loss of water and some low melting organic residues form the matrix (Fig. 4D.24a & 4D.24b). IL confined samples are found to be stable through the TGA scan and weight loss at 250 °C in some composites is corresponding to IL decomposition as mentioned in DTA section.

4D.5.1.4 Field Emission Scanning Electron Microscopy

The morphology of the samples has been determined from FE-SEM images, obtained at 500 nm scale. Interestingly for IL less sample (10LP), gel grains of almost uniform size ~30-50 nm are visible (Fig. 4D.25a). The grains are agglomerated in some regions. On the other hand, a sample containing IL (10LPB) appears to be more homogeneous and uniform with no separate grains are visible (Fig. 4D.25b). The measurements were done at room temperature at which IL may exist in the interfaces; therefore, its channels could not be seen. Nevertheless, it may be further suggested that IL exists uniformly well within the matrix.

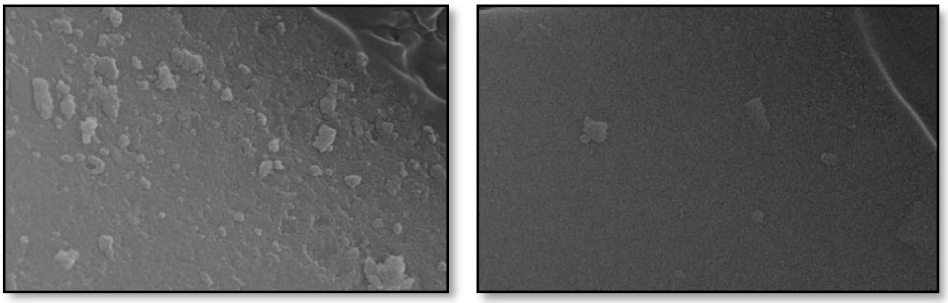

Fig. 4D.25 FE-SEM image of (a) IL-free sample (L10P) and (b) L10PB at 500 nm scale.

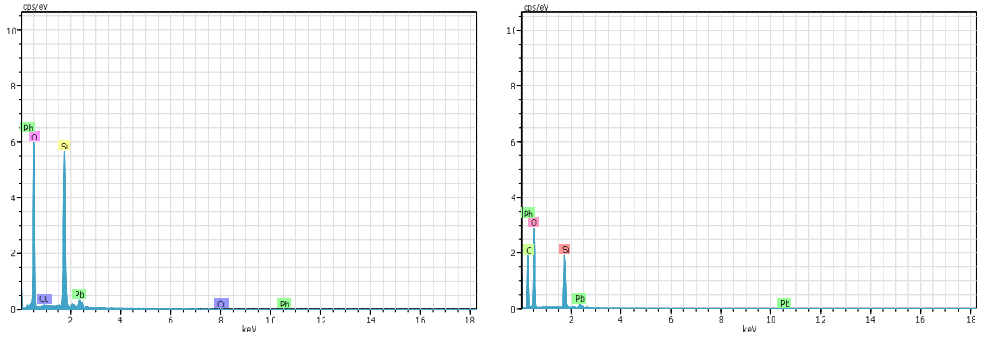

Fig. 4D.26 EDS results for sample (a) L10P and (b) L10PB.

Energy-dispersive X-ray spectrum (EDS) was also obtained to understand elemental composition in these systems. As seen (Fig. 4D.26a & 4D.26b) all the expected elements are visible in IL-free sample with no Carbon peak. This, in turn, suggests an error-free preparation process. In IL-confined samples, interestingly, a new peak corresponding to C

appears along with other peaks corresponding to expected elements. The peak corresponding to Carbon once again suggests confinement of IL in the matrix.

4D.5.2 Electrical Conductivity

Electrical transport in these systems has been explored through Nyquist plots for composites with (L10PB) and without IL (L10P) substitution (Fig. 4D.27a and 4D.27b). For both the cases, depressed semicircles (at higher frequencies) followed by an inclined line (at lower frequencies) is readily noticed. Thus, the samples are modeled as a parallel combination of resistance and a constant phase element (CPE1) in series with another CPE2. The inclined line at lower frequencies suggests predominant ionic transport, whereas, the depressed nature of the obtained semicircles confirms typical 'ionic glass-like' nature of the samples. The observed depression may be attributed to the non-Debye type nature of the samples; a typical characteristic of ionic glasses was also seen for IL-dispersed glasses investigated recently [24].

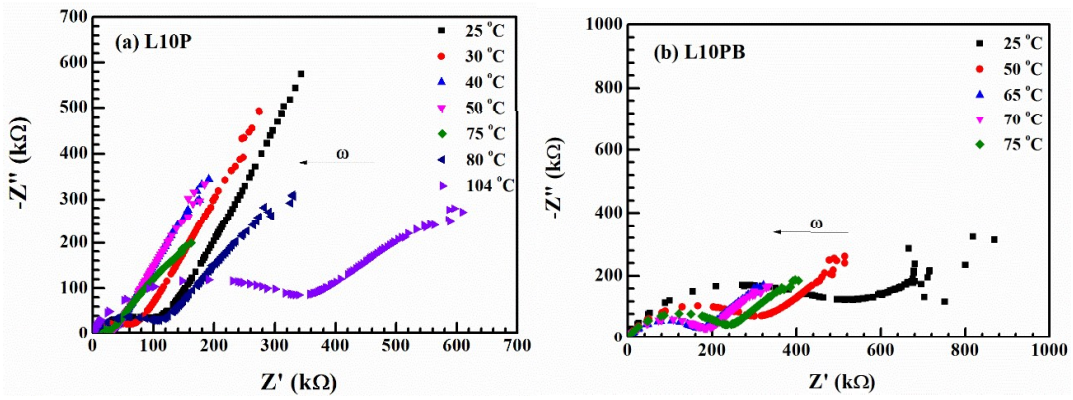

Fig. 4D.27 Nyquist plots for gel sample (a) with no IL (L10P), and (b) with 1 mol% IL (L10PB)

For both L10P and L10PB composites, the diameter of the semicircle (and hence dc resistance) gradually decreases, but above ~70 °C for both cases it increases. It may be inferred that due to the complex nature of these gel composites thermal stability is up to 70 °C.

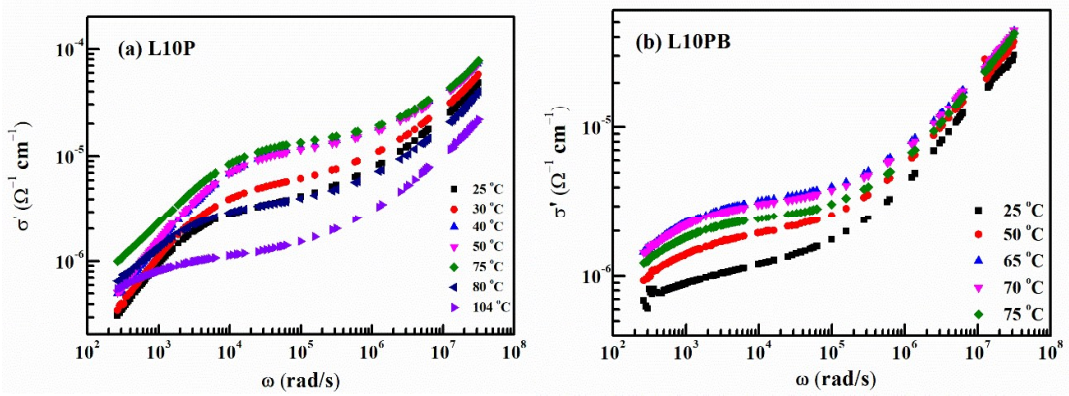

Fig. 4D.28 Electrical conductivity (σ′) has been plotted as a function of frequency (ω) for (a) L10P, and (b) L10PB gel composites.

The electrical conductivity of the gel composites has been determined and explored to understand the role of ions in conduction. Electrical conductivity (σ′) has been plotted as a function of frequency (ω) for L10P and L10PB gel composites (Fig. 4D.28a & 4D.28b). Apparently, conductivity exhibits a plateau region in a wide frequency range followed by dispersion in the high-frequency region as well as in the low-frequency region. Plateau region was used to obtain dc conductivity (σ_{dc}). Three distinct regions of the plots correspond for (i) dispersion at a high-frequency region corresponding to short-range motions, (ii) plateau region, where conductivity is independent of the frequency and (iii) low-frequency polarization corresponding to different interfacial polarization.

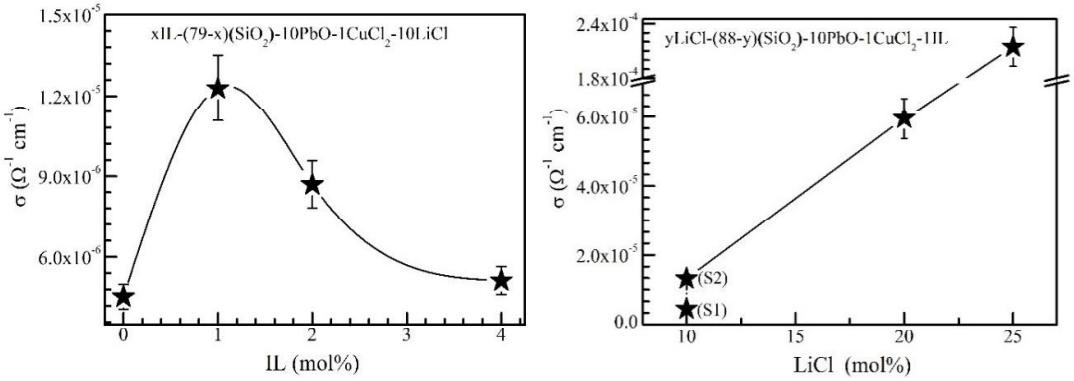

Fig. 4D.29 (a) Electrical conductivity vs IL content at 300K. (a) Increasing IL for fixed LiCl concentration (10 mol%), and (b) increasing LiCl for fixed IL concentration (1 mol%).

Composition dependence of electrical conductivity has also been determined as a function

of IL content (Fig. 4D.29a) as well as a function of LiCl concentration (Fig. 4D.29b) at 300K. As evident, for 1 mol% of IL, conductivity is found to be significantly higher than that of the parent gel composition. On further IL addition, conductivity drops gradually. A maximum value of ~10^{-5} $\Omega^{-1}cm^{-1}$ has been obtained for sample 10LP and 10LPB. For further studies, IL content was fixed to 1 mol% and Li^+ ion content was further increased as shown in Fig. 4A.29b. Interestingly conductivity exhibits appreciable rise up to 25 mol% of LiCl. Thus, for this composition, a conductivity of ~ 2 x 10^{-4} $\Omega^{-1}cm^{-1}$ is obtained at room temperature. Due to its complex nature, it was not possible to prepare gel for LiCl content higher than this composition.

Temperature dependence of electrical conductivity (σ_{dc}) is shown in Fig. 4D.30 and 4D.31. Apparently, in the low-temperature region sample with no IL (L10P), exhibits a relatively poor room temperature conductivity that increases linearly with temperature (Fig. 4D.30). On IL addition, an apparent rise in room temperature conductivity is witnessed. For this sample as well, conductivity exhibits similar Arrhenius behavior. When Li^+ ion content is increased, keeping IL amount constant, conductivity further increases. As evident, for the sample with high Li^+ content (L25PB), conductivity falls above ~ 53 °C that may be due to the different kinds of equilibria maintained at the inner pores of the composite and also due to the complex composition.

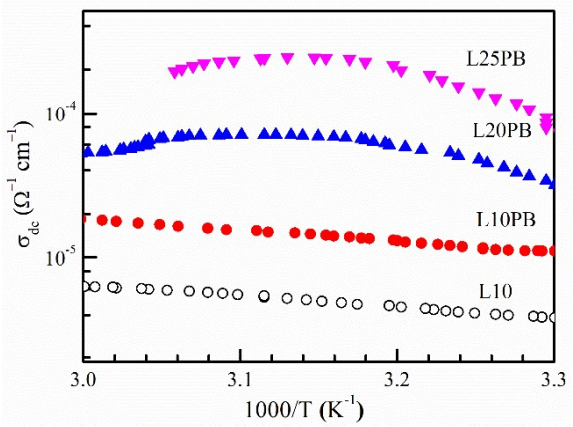

Fig. 4D.30 Electrical conductivity versus temperature for different samples.

Low-temperature conductivity of the prepared gel composites is attributed to the conductivity of both Li^+ ions and H^+ conduction form the adsorbed water molecules, on

initial thermal activation. With a rise in temperature and with loss of water, a fall in conductivity has been noticed. However, later with a further rise in temperature (above 125 °C), conductivity (in the high-temperature region) has been observed predominantly due to Li^+ ion conduction through the gel matrix [18].

The conductivity of these composites in high temperature (125 - 275 °C) region was also determined (Fig. 4D.31). For an increase in IL concentration, there is a decrease in conductivity of the samples and their obtained conductivity is ~10^{-8} to 10^{-9} Ω^{-1} cm^{-1} at ~200 °C. However, on increasing LiCl concentration with 1 mol% IL no significant rise in conductivity (~10^{-7} to 10^{-6} Ω^{-1} cm^{-1}) was noticed up to 25 mol% LiCl substitution in the whole temperature range. However, on further increase in LiCl to 30 mol% increase in conductivity (~10^{-5} Ω^{-1} cm^{-1}) can be seen in Fig. 4D.31 at ~200 °C.

For the samples of this series-3, the temperature dependence of conductivity was found to be very similar (to series-1), particularly for high salt content. As apparent, Arrhenius behavior is again witnessed with an activation energy of ~ 0.6 – 0.8 eV. If the conductivity is compared with that of similar composition of series-1 (25 mol%) then a marginally high conductivity is seen in the case of composites having Pb^{+2}.

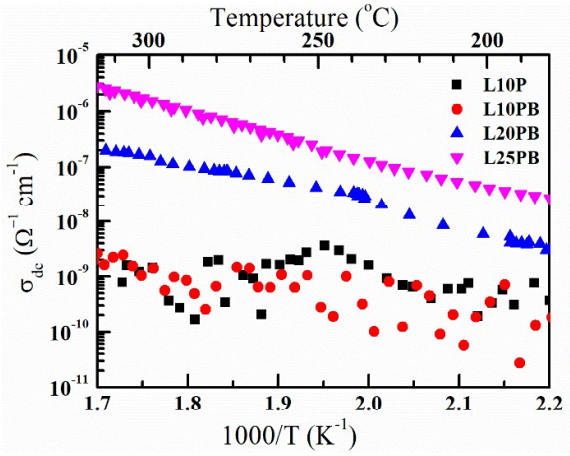

Fig. 4D.31 Electrical conductivity versus temperature for different gel composites.

4D.5.3 Ion Transport Mechanism

Just like the above system, gel composites of these systems also exhibit a good scaling behaviour with temperature variation as evident in Fig. 4D.32. L10P and L10PB

composites exhibit a similar process of charge transfer in the whole temperature range.

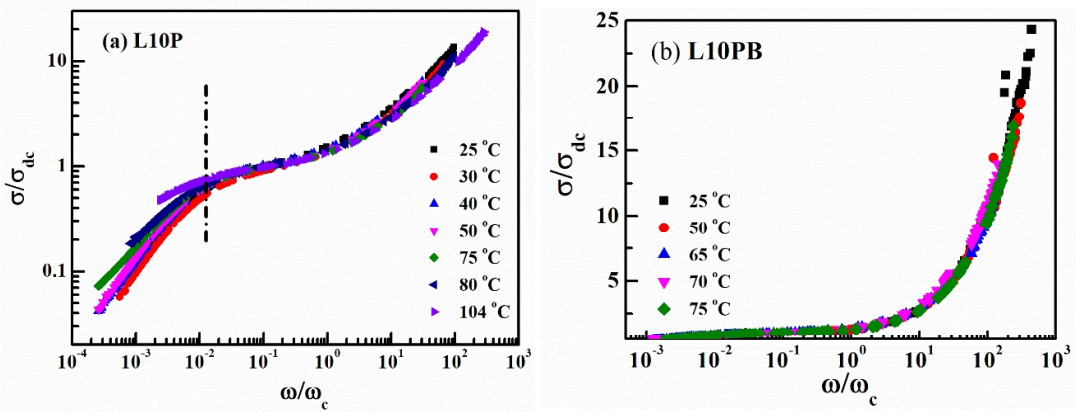

Fig. 4D.32 Scaling behavior of conductivity for L10P and L10PB with temperature.

However, the process of ion transfer remains the same even with the change in the compositions of the composites (Fig. 4D.33). Thus, the ion transfer process in these composites is independent of both (i) change in temperature and (ii) change in composition.

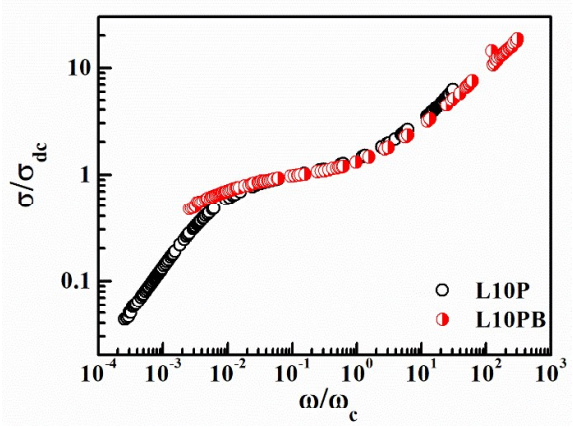

Fig. 4D.33 Scaling behavior of conductivity for L10P and L10PB and S2 at ~50 °C.

4D.6 Conclusions

Ionic liquid ([BMIM] Br) confined Li^+ ion-based silicate glassy composites have been prepared in three series of compositions. Investigations on structural, thermal properties, particularly with a focus on electrical transport and capacitance reveal interesting results. As evident from electrical transport studies, the ionic liquid does not contribute directly to the conductivity of the samples. The bigger and heavy ions of ionic liquids are not expected to move in the solid electrolytes. It may be suggested that ionic liquid contributes in two

ways viz. (i) providing a medium for salt ions to propagate and (ii) facilitating the dissociation of salt owing to its high dielectric constant. Thus, it contributes to the conductivity enhancement with increasing LiCl content samples. Some interesting inferences for this system are:

(i) Presence of a very small amount of IL enables Li^+ ion activation in the composites. It is proposed that IL ions remain immobile and do not contribute to electrical transport. In fact, IL acts like a plasticizer to support Li^+ ion mobility.

(ii) IL ions ($[BMIM]^+$ or Br^-) do not contribute to electrical transport. This may be due to their bigger size and smaller content in the matrix,

(iii) IL presence in the matrix, though apparently in small amount, facilitates Li^+ ion motion. This is evident from the effect of temperature variation and compositional alterations on electrical conductivity,

(iv) The structural investigations suggest that IL is very much confined in the matrix. Both structural and thermal studies indicate that in composites without Pb. at least up to 350 ^oC IL is confined in the system and does not decompose. Thus, a wide thermal stability range is observed for these composites.

(v) The EPR results indicate the conducting ions may be present in a pool of fluidic substances in the inner-pores of the composites.

(vi) The samples in both these series are predominantly ionic in nature as apparent from the dc-polarization studies.

(vii) Incorporation of Pb^{+2} ion in the composite increases the conductivity marginally. In some of the Pb containing samples the decomposition of IL is seen in thermal studies.

System 4E

[EMIM] CF_3SO_3 Confined Lithium Silicate Gel Composites Prepared by Hydrolytic Sol-Gel Process

4E.1 Compositions

In continuing with the variations with system 4A, here we have replaced IL: [EMIM] BF_4 with IL: [EMIM] CF_3SO_3. This particular IL has been chosen to understand the effect of change in counter ion on the structure and conducting properties of silica-gel solid electrolytes. The composites have been prepared by the hydrolytic sol-gel process (Table 410). We have said earlier that the complex formation with lithium ion with the anion of IL could be one possible reason for the conductivity changes in different compositions. The study with a changed anion of the same ionic liquid can possibly throw some evidences for the above conjecture.

Table 4.10 Composition, density and molar volume of composites with [EMIM] CF_3SO_3.

Sample Code	$LiNO_3$	[EMIM]CF_3SO_3	$CuCl_2$	SiO_2	Density (gm cm^{-3})	Molar Volume (cm^3 mol^{-1})	
	(mol%)				Experimental	Calculated*	Experimental
Series-1							
L18F	18.2	0.90	0.90	80	1.153	24.68	55.65
L33F	33.3	0.83	0.83	65	1.297	25.60	50.34
L46F	46.1	0.76	0.76	52.3	1.281	26.27	51.69
Series-2							
L18F	18.2	0.9	0.9	80	1.153	24.68	55.65
L18F3	18.2	2.7	0.9	78.2	1.115	26.37	60.78
L18F4	18.2	4.5	0.9	76.3	1.232	27.96	57.88
L18F9	18.2	9.1	0.9	71.8	1.231	32.36	65.46
L18F13	18.2	13.6	0.9	67.3	1.156	36.71	77.49
Series-3							
L18F4	18.2	4.5	0.9	76.3	1.232	27.96	57.88
L33F4	33.3	4.1	0.83	61.2	1.205	28.65	59.68
L46F4	46.1	3.8	0.76	49.2	1.254	29.13	57.62

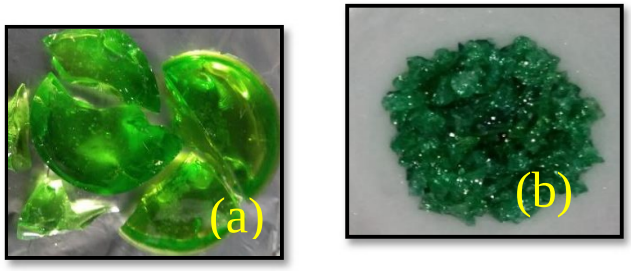

Fig. 4E.1 Photographic images at 1x magnification of the homogeneous densified gel (left) just before and (right) after heating at 150 ºC.

4E.2 Structural Studies

4E.2.1 Density and Molar Volume

Molar volume variation of the composites can be observed with a change in concentration of both $LiNO_3$ as well as IL (Fig. 4E.2). The experimental molar volume is higher as compared to the calculated values, suggests an expansion of the network during the formation of amorphous composites. However, the trend of both the calculated and the experimental molar volume variation remains similar for specific compositional alterations. The density results are also indicative of an increase in the volume of the composites with increasing IL content. However, with an increase in $LiNO_3$ content, the net volume of the composites remains almost comparable. Thus, it may be suggested that the presence of IL in a matrix certainly brings in the changes of the network structure, the added lithium ions go to the void nano pores of the silica gel.

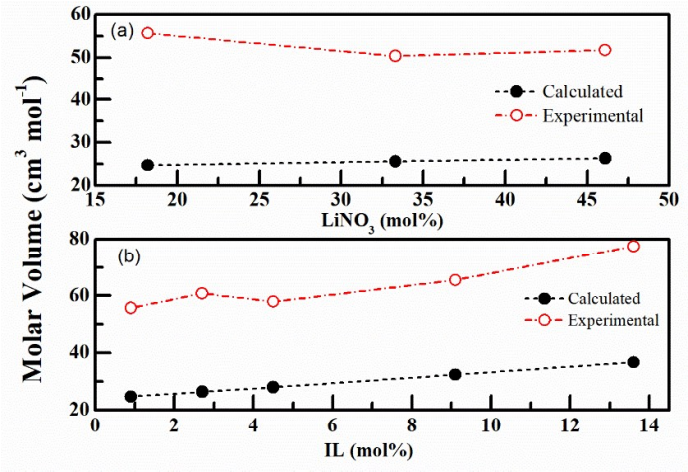

Fig. 4E.2 Molar Volume of the prepared composites (a) Series 1 and (b) Series 2 (within error limits of ±0.05 cm^3 mol^{-1}).

4E.2.2 Powder X-Ray Diffraction

Powder X-ray diffraction patterns of the prepared composites were analyzed to understand their structure. Halo patterns (Fig. 4E.3) for most of the prepared samples confirm their amorphous nature in a wider range of planned compositions. For incorporation of IL up to 13 mol%, it does not lead to formation/precipitation of any compound, or even crystallization of the gel or the glass composite obtained even after drying. Therefore, composites are non-crystalline in nature.

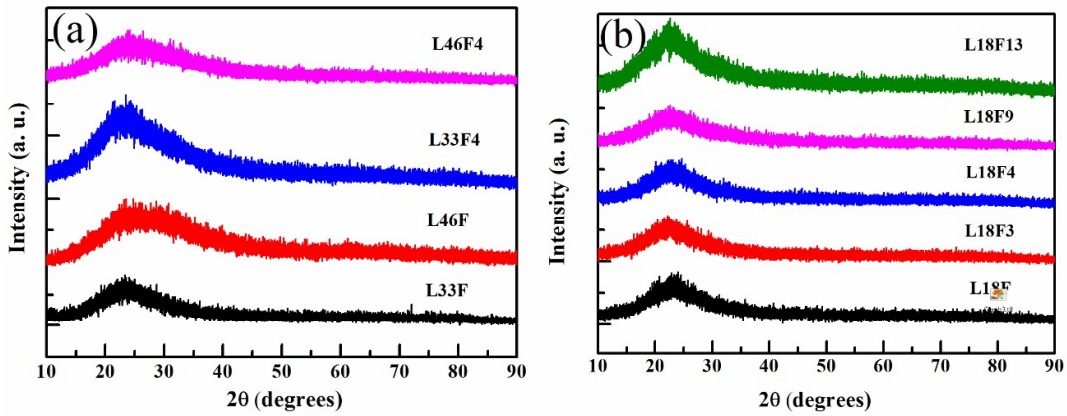

Fig. 4E.3 XRD plots for (a) Series 1 and 3, and (b) Series 2.

4E.2.3 FTIR Spectroscopy

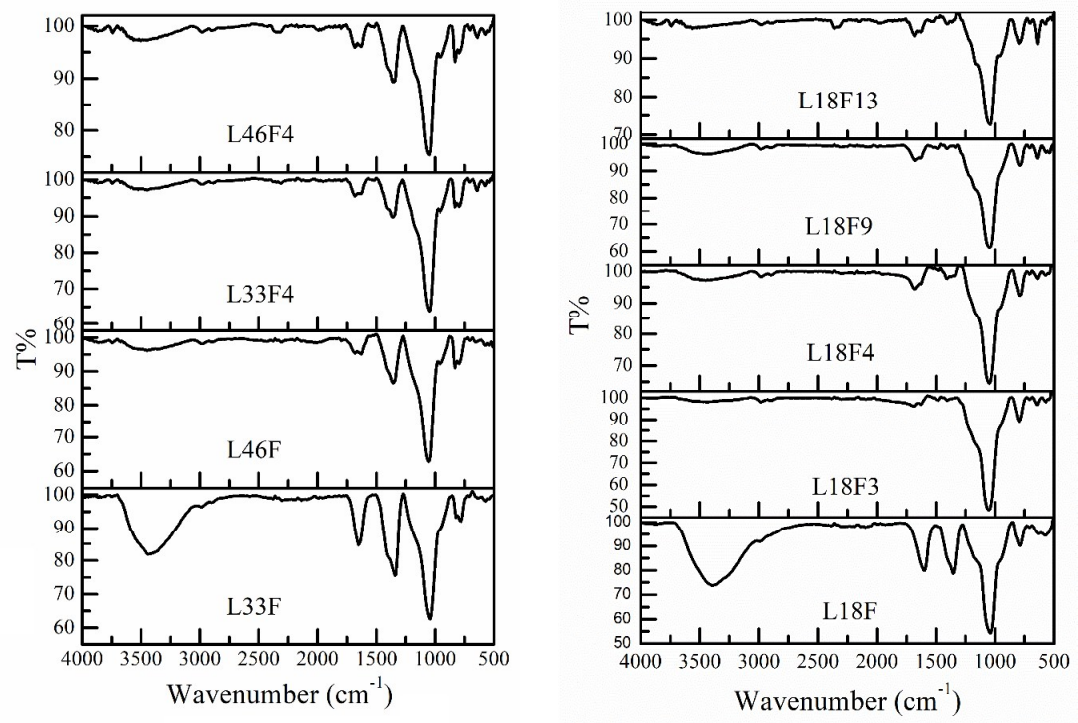

Fig. 4E.4 FTIR plots of the composites in ATR mode (a) Series-1 and-3, and (b) Series-2.

FTIR of the samples was recorded in ATR mode and also in the normal transmission mode where dry sample is in KBr matrix. Absorption in the IR spectrum in ATR mode is mainly due to silica network and water-ethanol mixture (as explained earlier in other sections). However, in the IR spectrum of transmission mode peaks corresponding to water, nitrate and ethanol emerge strongly. Stretching vibration of hydrogen-bonded -OH (ν_{OH}) broad

peak at 3500 cm^{-1}, bending vibrations of -CH_2-(δ_{CH2}) at 1400 cm^{-1} and bending vibrations of water (δ_{OH}) at 1600 cm^{-1}, indicating the major amount of water, ethanol mixture is present in the physisorbed form in the porous gel structure. The peak at 1400 cm^{-1} is also due to the antisymmetric stretching mode of the nitrate anion. Other absorptions are (identified as) 463 cm^{-1} (O-Si-O bending), 825 cm^{-1} (Si-O-Si symmetric stretching), and 1072 cm^{-1} broad peak with a shoulder at 1188 cm^{-1} (Si-O-Si asymmetric stretching).

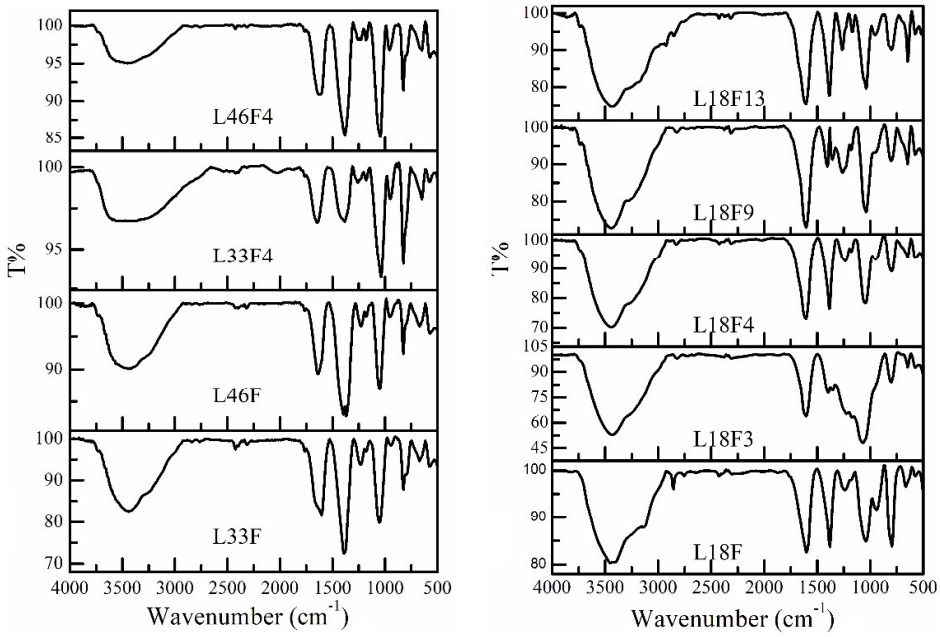

Fig. 4E.5 FTIR plots of the composites in transmission mode (a) mode (a) Series-1 and -3, and (b) Series-2.

For the IL ([EMIM] CF_3SO_3), some of the important absorptions corresponding to 1-ethyl-3-methylimidazolium cation are expected at; 3118 and 3157 cm^{-1} (aromatic ring C-H stretching). Weak 2984 -2970 cm^{-1} (Antisymmetric stretching of –CH_3, -CH_2 and symmetric stretching of –CH_2), sharp peak 1576 cm^{-1} (ring C=C stretching vibrations), and 1172 cm^{-1} (stretching vibrations of N-Et and N-Me) [63, 66]. IR spectrum range between 800 and 1400 cm^{-1} marks for local structural changes in CF_3SO_3 [TFS^-]. The strong band below 1400 cm^{-1} (vibrations of TFS^- anion), 1032 and 1270 cm^{-1} are attributed to symmetric and asymmetric stretching vibrations of SO_3 anion respectively. CF_3 asymmetric and symmetric vibrations were assigned to peaks around 1163 and 1227 cm^{-1} respectively [63]. The peaks in these regions corresponding to CF_3SO_3 group of anions can

be identified in the transmission mode IR spectrum easily. This helps in confirming the presence of IL: [EMIM] CF_3SO_3 in the prepared silica gel matrix.

4E.2.5 Field Emission Scanning Electron Microscopy

Morphology of the prepared composites has been analyzed through FESEM analysis (Fig. 4E.6) perceived at 500 nm scale to understand the effect/distribution of IL in the matrix. Homogeneous nature of the prepared composites is evident from the figures.

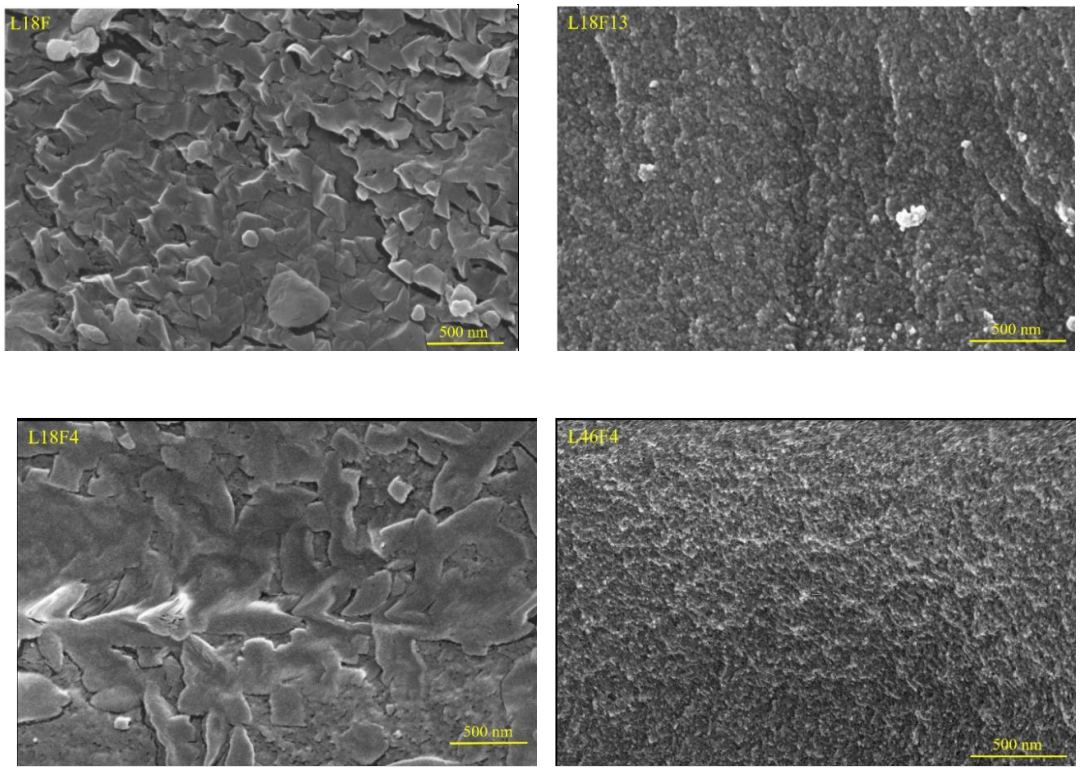

Fig. 4E.6 Change in the structure of L18F, L18F13, L18F4, and L46F4 composites.

With the increase in the IL concentration, the morphology of the silica gel matrix changes considerably; it exhibits an extremely homogeneous nature for high IL containing composite (L18F13) as compared to the composite with low IL content (L18F). The low IL containing composites (L18F and L18F4) exhibit tiny undistinguishable grains, which is more apparent in the case of L18F. A beginning of liquidus (increase in homogeneous) nature can also be seen in these composites (L18F4) on increasing IL content.

Elemental Mapping of the composites showed a uniform distribution of the elements corresponding to IL elements (C, N, F, and S) throughout the matrix. FESEM analysis of

the composites states that the homogeneous distribution of IL in the silica gel matrix facilitates new structural changes (Fig. 4E.7).

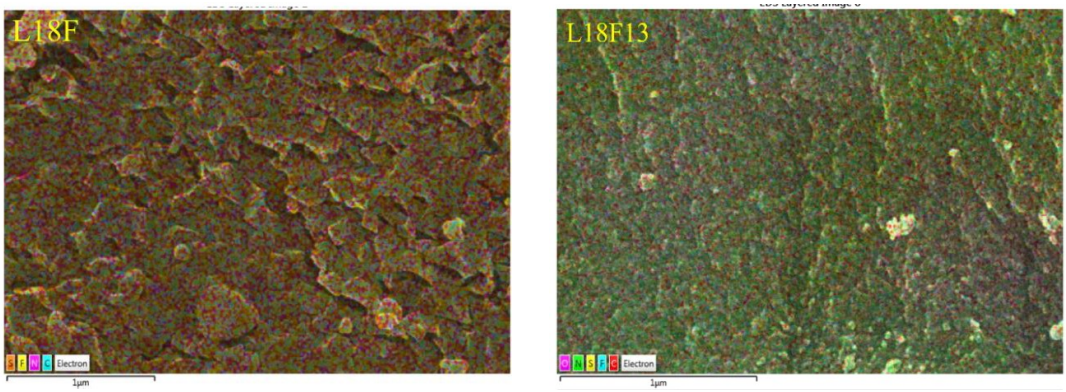

Fig. 4E.7 EDS mapping of L18F and L18F13 composites.

4E.3 Thermal Analysis

4E.3.1 Differential Thermal Analysis

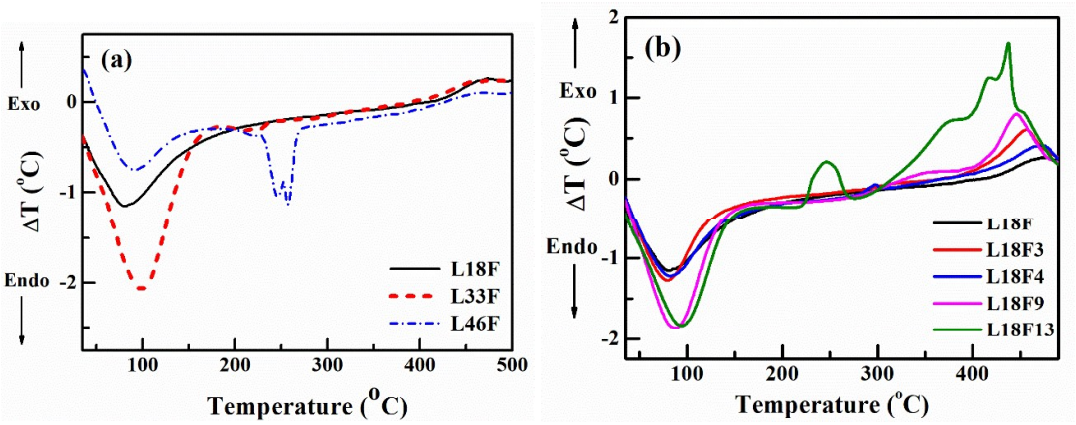

Fig. 4E.8 DTA plots for (a) Series-1, and (b) Series-2.

DTA of the prepared composites have been done in the temperature range of 35 ^{o}C to 500 ^{o}C with a heating rate of 10 ^{o}C/minute in a nitrogen atmosphere (Fig. 4E.8). The first endothermic dip obtained in the temperature range of 50 to 150 ^{o}C, is related to the loss of adsorbed water and ethanol from the matrix of the system. This loss is mainly observed from the capillaries or from the surface of the composites. For composites with increased concentration of the $LiNO_3$ (L46F), an endothermic dip around 250 ^{o}C corresponding to the melting of $LiNO_3$ appears, indicating the presence of $LiNO_3$ being present in the matrix

of the composites. These composites also exhibit an exothermic peak after 400 ^{o}C corresponding to the loss of IL from the matrix in beyond a certain temperature (>400 ^{o}C). This exothermic peak is observed in all the DTA plots, however, prominently for the composites with an increase in IL concentration.

4E.3.2 Thermogravimetric Analysis

TGA scans of the prepared IL ([EMIM] CF_3SO_3) confined composite via hydrolytic sol-gel process are shown in Fig. 4E.9. The composites exhibit a weight loss near 100 °C, as observed with the DTA results where the loss of confined water/ethanol from the composite occurs. It is interesting to note that, for IL increasing composites there is minimal weight loss in the range of 150 - 400 ^{o}C indicating only solvent removal from surface and inner pores happens at this temperature range as explained in previous sections. The decomposition/loss of IL can be marked by a significant weight loss of 5 - 10 w% after 400 ^{o}C in the composites with an increase in IL concentration. These studies showed that these composites are thermally stable in a wide temperature range and on the basis of these results the stable region of ~150 - 350 ^{o}C has been identified for high-temperature electrical transport investigations.

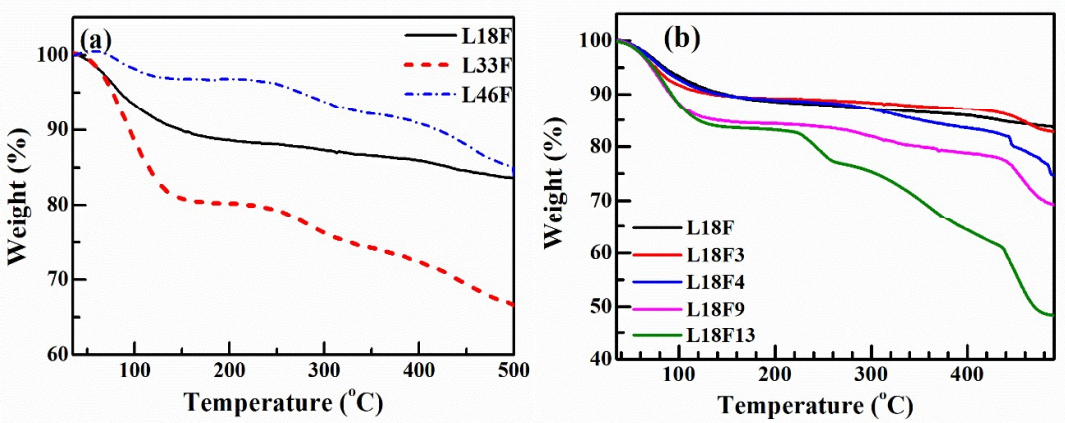

Fig. 4E.9 TGA plots for (a) Series-1, and (b) Series-2.

4E.4 Electrical Conductivity

4E.4.1 Impedance Spectroscopy

Impedance spectroscopy has been used to understand the temperature (250 - 350 ^{o}C) and frequency (42 Hz to 5 MHz) dependence of electrical transport thoroughly. Nyquist plots in blocking electrode configuration have been shown in Fig. 4E.10 for the composites with

an increase in IL concentration and keeping Li^+ ion content constant (18 mol%). The plots exhibit depressed semicircles with no/low polarization in the low-frequency region. Basic nature of the Nyquist plots remains unaffected with the increase in IL concentration except for L18F13 composite. This suggests for prevailing electronic contribution in the total electrical transport in these composites. Besides, an increase in conductivity of the composites with temperature also suggests non-metallic behavior of the composites as well.

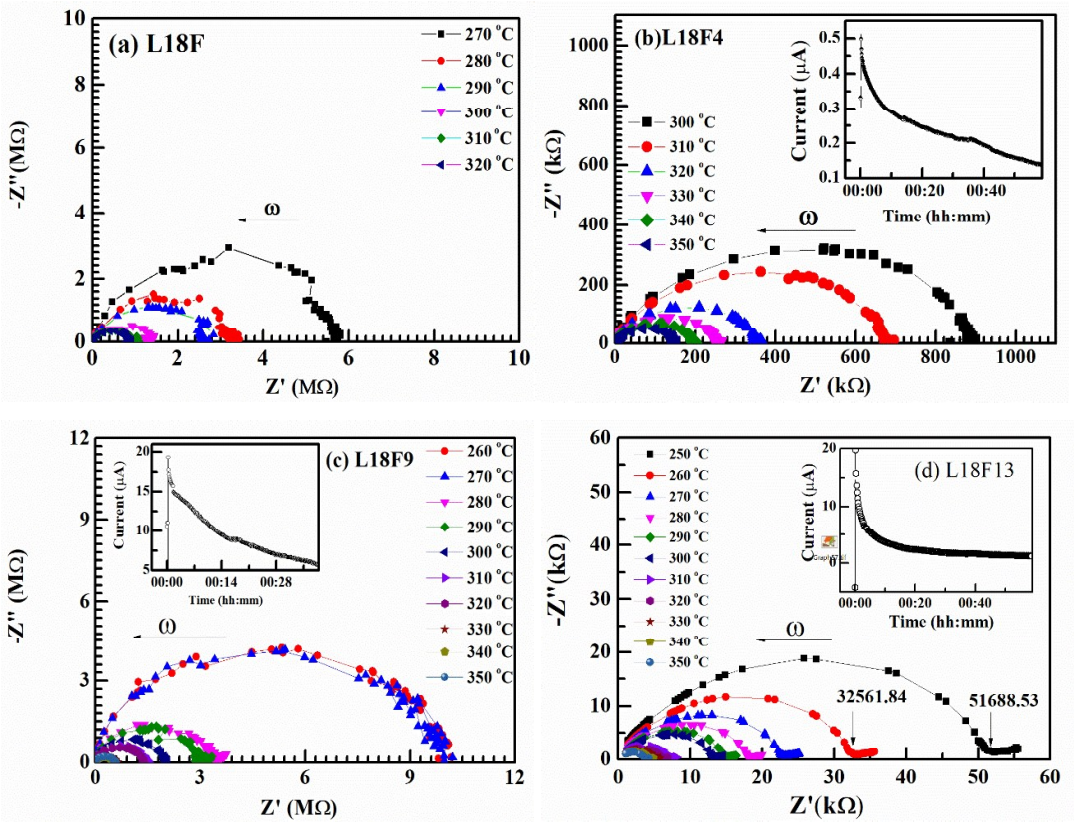

Fig. 4E.10 Nyquist plots for the composites with increasing IL and constant Li^+ ion content (18 mol%) – Series 2.

To further understand the conductivity nature of the composites, IL content has been fixed to 4 mol% and Li^+ ion concentration has been varied (Fig. 4E.11). An insignificant change in nature of the Nyquist plots of the composites could be seen in form of a small tail/spur in low-frequency region with an increase in Li^+ ion concentration, suggesting for the increase in polarization of ions at the interfaces. This marks evidence for the initiation of ionic transport with salt addition and the polarization effect is marked due to ionic transport

of the ions. All these composites are expected to be equivalent to a parallel combination of the resistor and constant phase element (CPE) in the electronic circuit.

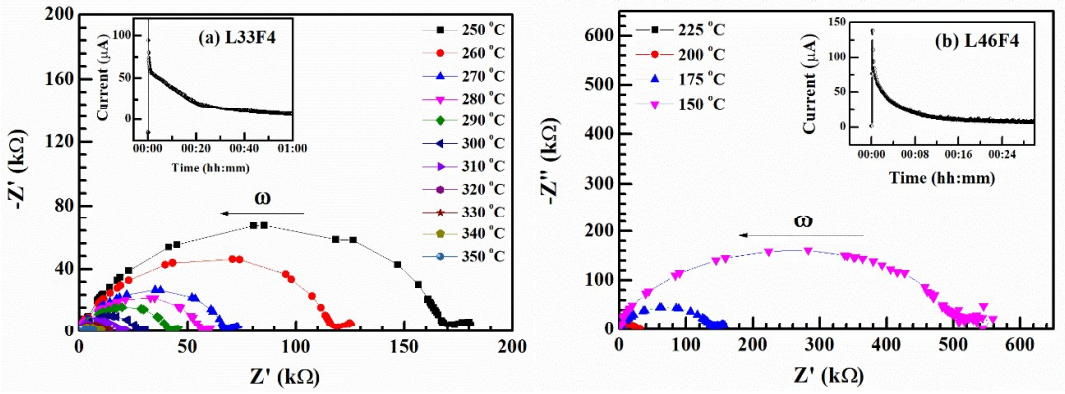

Fig. 4E.11 Nyquist plots for the composites of series-3.

Ionic nature of the composites has been further explored by dc-polarization studies (Inset: Fig. 4E.11a and b), where dc voltage of ~0.5 V has been applied across the sample and time dependence of the transient current is measured. DC polarization results state that these composites are ionic in nature.

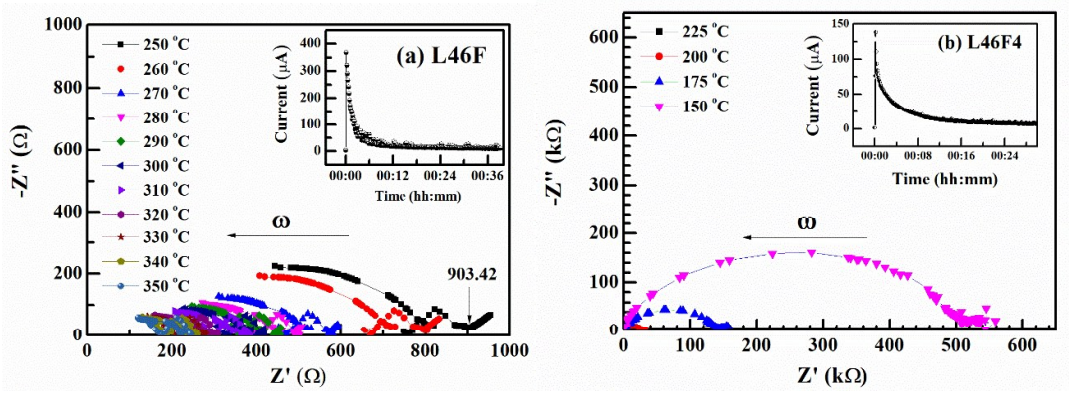

Fig. 4E.12 Nyquist plots for (a) L46F and (b) L46F4 composites in a temperature range of 250-350 °C.

Unlike, the other cases, where the Nyquist plots exhibit well defined depressed semi-circles trend, here for some of the compositions (L46F and L46F4) in Fig. 4F.12 the plots appear differently. Particularly, at lower frequencies scattered data points are seen followed by initiation of a depressed semicircle. This is most likely due to high ionic conductivity in comparison to other compositions. So, generally as discussed previously a

semicircle in Nyquist plots represent a parallel combination of resistance and capacitance. When frequency is very low, the capacitive reactance value becomes significantly high. Further, if the resistance of sample is low then the overall equivalent circuit may be modelled as a resistance alone. When the frequency is high the capacitive reactance decreases and now the sample may be modelled as a parallel combination of resistance and capacitance. Therefore, semicircle trend at higher frequencies is not surprising. However, at the lower frequencies a tail is evident that readily suggests polarization at electrode-electrolyte interface. This also suggests predominant ionic nature of the highly ionic conducting compositions.

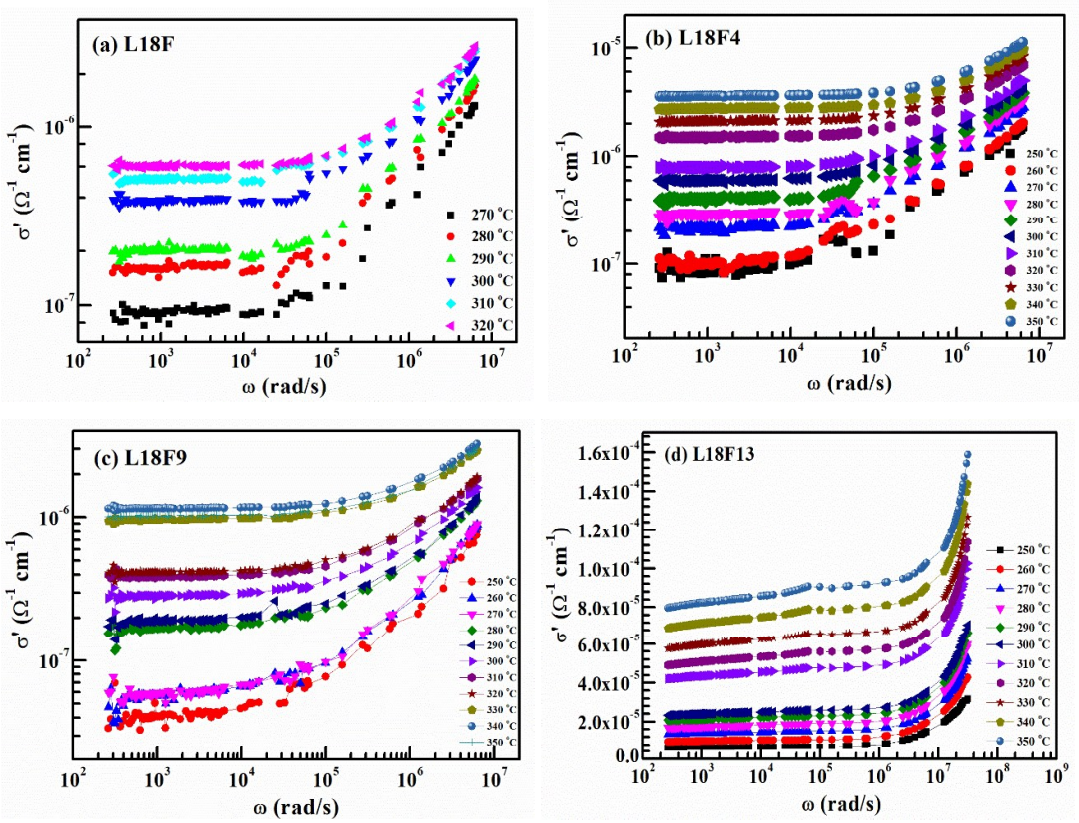

Fig. 4E.13 Electrical conductivity (σ′) as a function of frequency (ω) plots for the composites Series-2.

These composites exhibit thermal stability in a wide temperature range as evident from DTA and TGA plots. Electrical measurements have been explored in this thermally stable region, to understand the confinement effect of the IL in the matrix. Electrical conductivity (σ′) has been plotted as a function of frequency for different composites in a wide

temperature range (Fig. 4E.13). Conductivity exhibits a plateau in a wide range of frequency followed by dispersion in the high-frequency region. Plateau region corresponds to frequency-independent conductivity (σ_{dc}) whereas the dispersion corresponds to interfacial polarization.

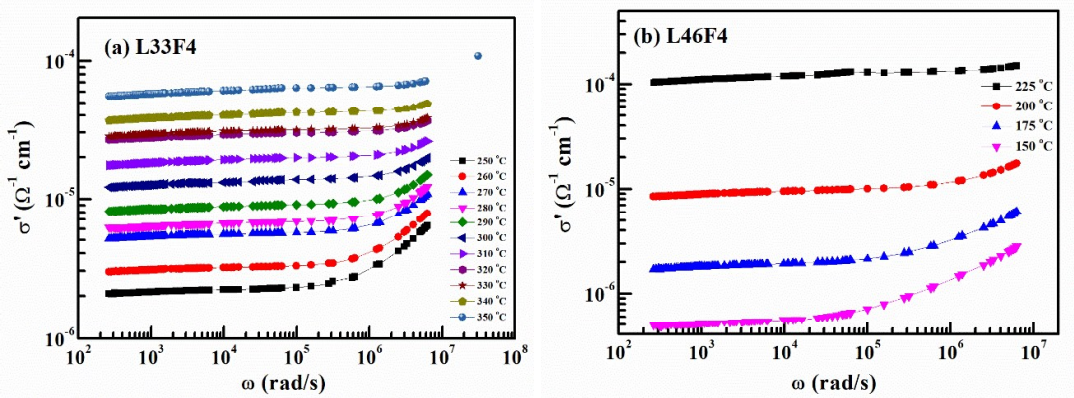

Fig. 4E.14 Electrical conductivity (σ′) as a function of frequency (ω) plots for L33F4 and L46F4 composites.

Fig. 4E.13 and Fig. 4E.14, it is showed that these composites exhibit frequency-independent conductivity in a wide frequency region, attributed to a suppression of the events associated with polarization and/or long-range diffusive motion of ions. Thus, with an increase in the concentration of both IL and $LiNO_3$ long-range ionic motion is facilitated. A possible reason for this could be an increase in the homogeneous structure of the matrix with no/less grain boundary effect, where the resistance required for ionic motions is reduced.

4E.4.2 Conductivity cycles

σ-T cycles of the prepared composites have been explored and shown in Fig. 4E.15 and 4E.16. These plots exhibit an Arrhenius trend in conductivity with the rise in temperature. It is interesting to note that (i) it was possible to incorporate ~13 mol% IL ([EMIM] CF_3SO_3) in the matrix (which was ~7 mol% in case of [EMIM] BF_4 containing composites), (ii) with increase in IL concentration the rise in conductivity was also observed significantly. Conductivity rise of ~2 orders of magnitude rise was observed from L18F to L18F3 composites (Fig. 4E.15 (left)). For a maximum of 13 mol% IL substitution, maximum conductivity of ~10^{-6} Ω^{-1} cm^{-1} was achieved at 250 ^oC with a linear rise. This

indicates that IL [EMIM] CF_3SO_3 plays an important role in enhancing the electrical conductivity of these composites.

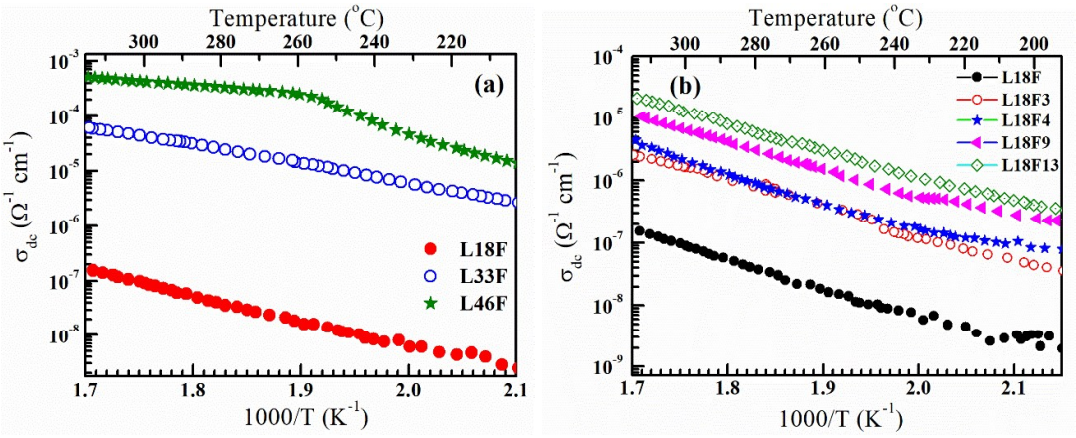

Fig. 4E.15 σ-T plots for (left) Series-1 and (right) Series-2.

σ-T cycles of the prepared composites have been explored and shown in Fig. 4E.15 and 4E.16. These plots exhibit an Arrhenius trend in conductivity with the rise in temperature. It is interesting to note that (i) it was possible to incorporate ~13 mol% IL ([EMIM] CF_3SO_3) in the matrix (which was ~7 mol% in case of [EMIM] BF_4 containing composites), (ii) with increase in IL concentration the rise in conductivity was also observed significantly. Conductivity rise of ~2 orders of magnitude rise was observed from L18F to L18F3 composites (Fig. 4E.15 (left)). For a maximum of 13 mol% IL substitution, maximum conductivity of ~10^{-6} Ω^{-1} cm^{-1} was achieved at 250 °C with a linear rise. This indicates that IL [EMIM] CF_3SO_3 plays an important role in enhancing the electrical conductivity of these composites.

The effect of an increase in $LiNO_3$ concentration by keeping IL concentration constant to 1mol% also showed an interesting trend (Fig. 4E.15 (left)). Conductivity rise by ~3 orders of magnitude was noticed on increasing the concentration of Li^+ ions from 18 mol% to 33 mol%. However, for similar composites with 4 mol% IL an analogous conducting behaviour was also observed. In the present case rise in conductivity was more from L33F4 to L46F4 composites (Fig. 4E.16). We can say that IL and Li^+ ion (in a certain compositional range/combinations) can exhibit very encouraging electrical conducting properties. The change in conductivity of the composites with temperature variations and their activation energy has been tabulated systematically in Table – 4.11.

Table 4.11: Conductivity at different temperatures and activation energy for the samples at high temperature.

Sample Code	Conductivity at 305 K	Conductivity at 523 K	Conductivity at 548 K	Activation Energy (eV)
	(Ω^{-1} cm^{-1})			
Increasing $LiNO_3$ Concentration with 1 mol% IL				
L18F	$8.2x10^{-11}$	1.8×10^{-8}	6.0×10^{-8}	0.98
L33F	$6.2x10^{-6}$	1.5×10^{-5}	3.2×10^{-5}	0.64
L46F	$4.9x10^{-4}$	2.5×10^{-4}	3.8×10^{-4}	0.32
Increasing IL Concentration with 10 mol% $LiNO_3$				
L18F	$8.2x10^{-11}$	1.8×10^{-8}	6.0×10^{-8}	0.98
L18F3	$1.8x10^{-5}$	4.1×10^{-7}	1.2×10^{-6}	0.77
L18F4	$4.7x10^{-8}$	4.1×10^{-7}	1.2×10^{-6}	0.99
L18F9	$3.3x10^{-5}$	1.5×10^{-6}	4.2×10^{-6}	0.88
L18F13	$2.2x10^{-7}$	3.2×10^{-6}	8.3×10^{-6}	0.88
Increasing $LiNO_3$ Concentration with 5 mol% IL				
L18F4	$4.7x10^{-8}$	4.24×10^{-7}	1.3×10^{-6}	0.99
L33F4	$7.7x10^{-6}$	1.37×10^{-6}	4.0×10^{-6}	0.89
L46F4	0.0014	1.73×10^{-4}	2.2×10^{-4}	0.26

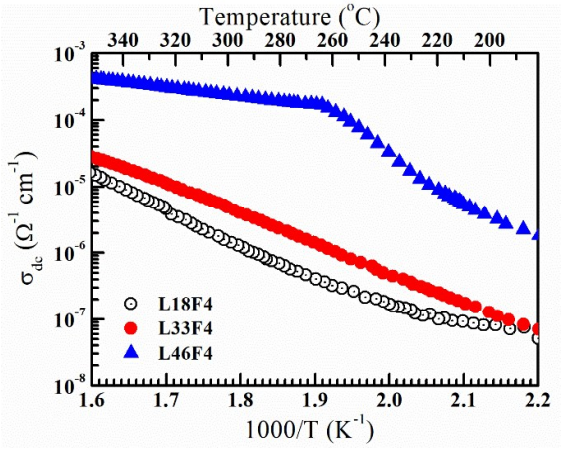

Fig.4E.16 σ-T plots for series-3 composites.

In order to understand the effect of IL on conductivity of the composites and another composite $20LiCF_3SO_3$-$CuCl_2$-$79SiO_2$ ($LiCF_3SO_3$ (20 mol%)) was prepared and its conductivity was compared with other comparable Li^+ ion composites i.e. L33F and L33F4 (Fig. 4.19). It is evident from the plot that $LiCF_3SO_3$ (20 mol%) composite exhibit very poor conductivity as compared to IL containing correspondent. This could be because the

presence of IL in silica solid support modifies the structure in such a way that Li^+ transfer is promoted. In absence of IL extremely poor conductivity (~10^{-8} – 10^{-9} Ω^{-1} cm^{-1}) has been observed.

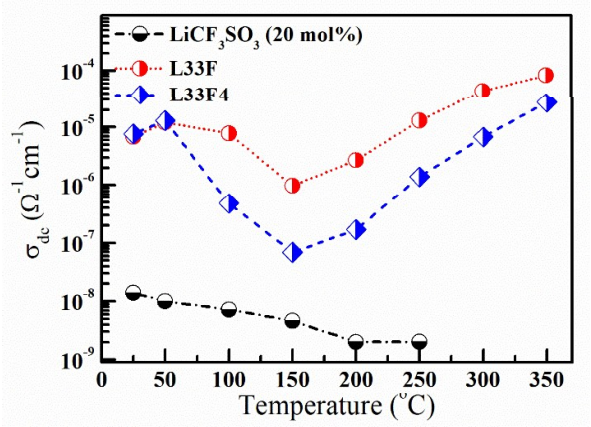

Fig. 4.17 σ-T plots for $LiCF_3SO_3$, L33F and L46F4 composites for comparision.

4E.4.3 Conductivity Formalism

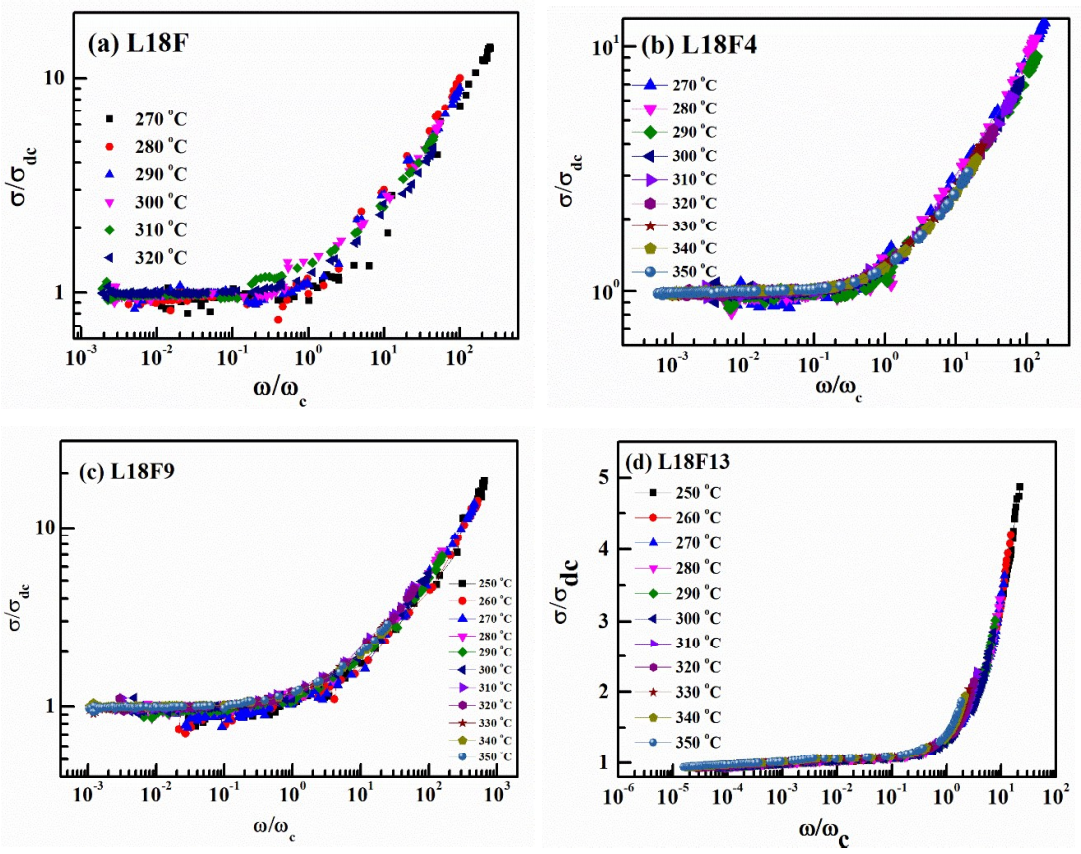

Fig. 4E.18 σ/σ_{dc} versus ω/ω_c plot for the composites of series-2.

The process of conduction mechanism was understood by determining the scaling behavior in log ω versus log σ plots (as explained earlier). σ/σ_{dc} versus ω/ω_c for the prepared composites have been plotted with different temperatures (Fig. 4E.18). From the scaling plots of increase in IL concentration, it is obvious that the ion-relaxation process falls on a single master curve in a wide frequency range with temperature variation. And the same trend could be observed for almost all the composites in a wide temperature range, indicating for a temperature-independent ion transfer mechanism.

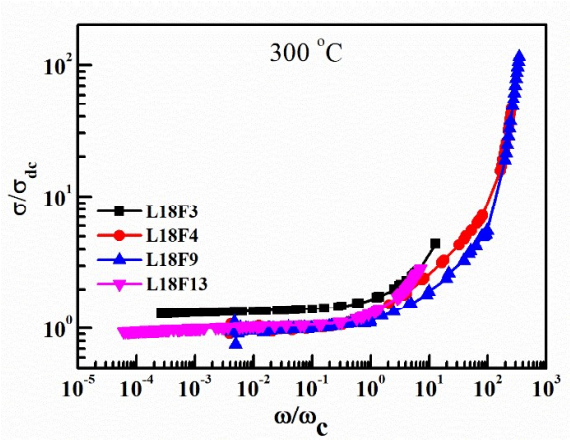

Fig. 4E.19 σ/σ_{dc} versus ω/ω_c plot for different compositions at ~300 °C.

However, for change in different composition (keeping Li^+ content fixed and increasing IL content) at ~300 °C, states for the different ion transfer process. This remarks that the ion transfer mechanism is independent of temperature but dependent on the composition (Fig. 4E.19).

4E.5 Conclusions

1. [EMIM] CF_3SO_3 and lithium nitrate containing composites formed amorphous silica gel in a wide range of compositions.
2. FTIR, FESEM and thermal analytical techniques supports the confinement of IL in the silica gel matrix.
3. FESEM analysis showed an increase in homogeneity of the surface on IL addition, and the EDS mapping determined the homogeneous distribution of elements.
4. Thermal analysis supports that the prepared silica gel composites are thermally stable in a wide temperature region (30 – 350 °C). Beyond which the decomposition of IL is evident from the thermal analysis plots.

5. Conductivity and dc polarization measurements supports that the presence of IL in the system supports the ionic conduction, where as in absence of IL as explored in case of $20LiCF_3SO_3$-$CuCl_2$-$79SiO_2$ composite, extremely poor conductivity ($\sim 10^{-8} - 10^{-9}\ \Omega^{-1}\ cm^{-1}$) was observed.
6. The process of ion conduction was dependent on compositions of the samples, and it was independent of temperature.
7. Some of the samples of this system show highest electrical conductivity among all the composites probed in this work.

4F

Evidence for the Presence of IL in the Solid Matrices

4F. Evidence for the presence of IL in solid matrices

The presence of IL in the prepared silica gel matrices was the biggest quest. In order to confirm the same, a few experiments were performed. It was still difficult to analyze the structure of these composites and how the IL was modifying the structure. But, these experiments could help us in understanding the important role IL is playing in defining magnificent properties of these composites. IL confinement has been explained mostly on [EMIM]BF_4 containing composites.

4F.1 Differential Scanning Calorimetry (DSC)

To prove the presence of IL in the system a low-temperature differential scanning calorimetry study on one of the samples (L18E) was done (Fig. 4F.1), as done by others [44].

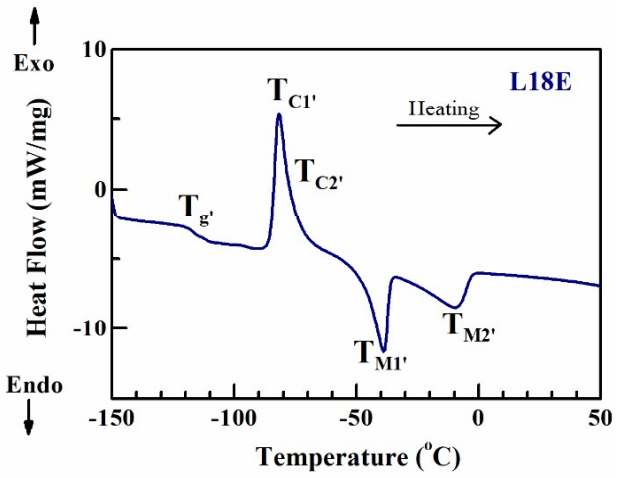

Fig. 4F.1 DSC plot of L18E composite.

In Fig. 4F.1, the low-temperature DSC recording of the sample L18E is shown. The glass transition is seen as a shallow endothermic peak from around -118 °C to around -90 °C, followed by an exothermic crystallization peak at -81 °C (with a shoulder at -74 °C) and two endothermic peaks indicating melting at -40 °C and -9 °C. The two sets of crystallization and melting peaks may be due to the presence of two crystalline forms. The pattern is similar to that of bulk IL as reported, [32, 39] but due to confinement and in the presence of lithium salt the critical temperatures have shifted to lower values. This result confirms the presence of IL in the composite prepared and the interaction of lithium salt and IL forming complexes.

4F.2 Electrical Conductivity Measurements

As explained earlier the samples were dried at 150 ^{o}C to remove the unbound external solvents. During this process, the IL confined in the system remains intact. To check the effect of heat treatment at a higher temperature, two samples one containing IL (L18E) and other without IL (L18) was heated at 500 ^{o}C for 24 hrs. and the conductivity measurements were repeated.

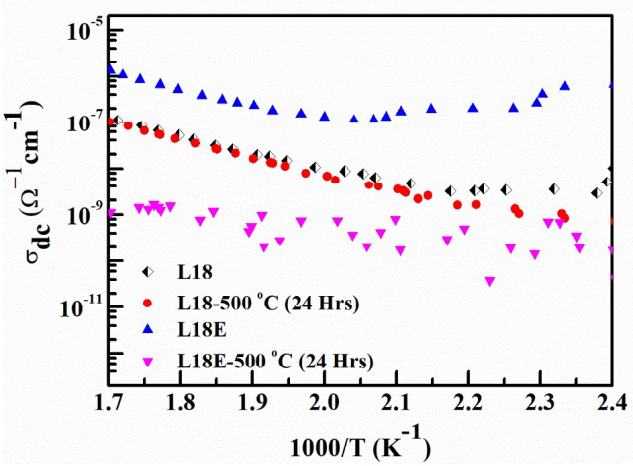

Fig. 4F.2 Conductivities of L18 and L18E composites, before and after heat treatment at 500 ^{o}C for 24 hrs.

In Fig. 4F.2, for L18, a sample without IL, the conductivity vs. temperature plot remains more or less the same. Whereas in the sample containing IL, L18E the conductivity is down by three orders of magnitude and fluctuating after heat treatment at 500 ^{o}C. By heating at 500 ^{o}C for 24 hrs the sample loses most of the solvent present in the surface and inner pores. Also since this temperature is well above the boiling-decomposing temperature of IL (350 ^{o}C) the IL might have also been removed from the matrix. However, while the IL is lost from the matrix along with IL more solvent molecules might have been removed and the nitrate decomposition process is accelerated as can be seen from Fig. 4B.9 (FT-IR or these samples after heat treatment). To summarize we may say, the addition of small amounts of IL increases the conductivity by an order of magnitude, however, if removed by thermal treatment even the minimum conductivity of skeleton structure is lost.

4F.3 X-Ray Photoelectron Spectroscopy (XPS)

Chemical composition of the surface of a material can be determined through XPS measurements. The technique is mostly a surface sensitive and mostly probes the top most layer of the material, but, it also be employed to depth profiles of up to 10 nm if high energies are employed.

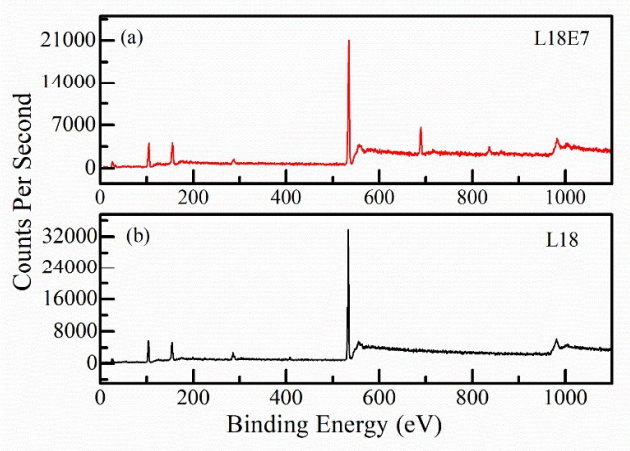

Fig. 4F.3 XP spectra of L18 and L18E7 composites.

Fig 4F.3 shows the XPS spectra of two composites where (a) with 7 mol% of $[EMIM]BF_4$ (L18E7) and (b) without IL, but lithium content is maintained at same level (L18). We could see additional peak at 690 eV which corresponds to F (1s) and the presence of $[EMIM]BF_4$ is confirmed [67]. In the sample containing IL another additional peak was observed at binding energy value of ~840 eV. This could be due to some impurity which we were unable to identify. The energy peak around 258 eV is attributed to C 1s of ethanol as it is present in both the spectra. Literature findings of silica nano-porous structures clearly define the chemical state of Si in the silicates or its other derived materials. Binding energy peak at 104 eV corresponds to Si^{4+} state in SiO_2 structure. The XPS signals for O 1s associated to silica network can be distinguished in two different oxygen environments, i.e. a bridge oxygen (~533 eV) and terminal oxygen (~531 eV) atoms [68].

References

1. Philippe Knauth, "Inorganic solid Li ion conductors: An overview." *Solid State Ionics*. **180** (2009) 911-916.
2. F. Borsa, D. R. Torgeson, S.W. Martin, H.K. Patel, "Relaxations and Fluctuations in Glassy Fast Ion Conductors: Wide-Frequency Range NMR and Conductivity Measurements." *Physical Review* **B46** (1992) 795-800.
3. Gin-ya Adachi, Nobuhito Imanaka, Hiromihi Aono, "Fast Li^+ conducting ceramic electrolytes." *Advanced Materials* **8** (1996) 127-135.
4. Victoria M. Hultgren, Andrew W. A. Mariotti, Alan M. Bond, Anthony G. Wedd, "Reference Potential Calibration and Voltammetry at Macrodisk Electrodes of Metallocene Derivatives in the Ionic Liquid [BMIM][PF_6]." *Analytical Chemistry* **74** (2002) 3151-3156.
5. Marisa C. Buzzeo, Russell G. Evans, Richard G. Comp, "Non Haloaluminate Room Temperature Ionic Liquids in Electrochemistry—A Review." *ChemPhysChem* **5** (2004) 1106-1120.
6. Deborah L. Boxall, Robert A. Osteryoung, "Electrochemical Properties of Alkali Metals in 1-Butyl-3-Methylimidazolium Hexafluorophosphate." *Journal of The Electrochemical Society* **149** (2002) E185-E188.
7. E. Stathatos, P. Lianos, S. M. Zakeeruddin, P. Liska, M. Grätzel, "A Quasi-Solid-State Dye-Sensitized Solar Cell Based on A Sol-Gel NanoComposite Electrolyte Containing Ionic Liquid." *Chemistry of Materials* **15** (2003) 1825-1829.
8. Hiroyuki Ohno (Editor), "*Electrochemical Aspects of Ionic Liquids*" Wiley (2005).
9. Kenneth R. Seddon, Annegret Stark, Maria-José Torres, "Influence of chloride, water, and organic solvents on the physical properties of ionic liquids." *Pure and Applied Chemistry* **72** (2000), 2275-2287.
10. Cinzia Chiappe, Daniela Pieraccini, "Kinetic study of the addition of trihalides to unsaturated compounds in ionic liquids. Evidence of a remarkable solvent effect in the reaction of ICl_2^-." *Journal of Organic Chemistry* **69** (2004) 6059-6064.
11. Philippe Hapiot, Corinne Lagrost, "Electrochemical reactivity in room temperature ionic liquids." *Chemical Review* **108** (2008) 2238-2264.

12. Douglas R. MacFarlane, Naoki Tachikawa, Maria Forsyth, Jennifer M. Pringle, Patrick C. Howlett, Gloria D. Elliott, James H. Davis, Jr., Masayoshi Watanabe, Patrice Simon, C. Austen Angell, "Energy applications of ionic liquids." *Energy and Environmental Science* **7** (2014) 232-250.
13. Shiguo Zhang, Jiaheng Zhang, Yan Zhang, Youquan Deng, "Nanoconfined ionic liquids." *Chemical Review* **117** (2017) 6755-6833.
14. Abdul Rehman, Xiangqun Zeng, "Ionic liquids as green solvents and electrolytes for robust chemical sensor development." *Accounts of Chemical Research* **45** (2012) 1667-1677.
15. Andrzej Lewandowski, Agnieszka Świderska-Mocek, "Ionic liquids as electrolytes for Li-ion batteries – An overview of electrochemical studies." *Journal of Power Sources*. **194** (2009) 601-609.
16. Jun Yan, Qian Wang, Tong Wei, Zhuangjun Fan, "Recent advances in design and fabrication of electrochemical supercapacitors with high energy densities." *Advance Energy Materials*. **4** (2014) 1300816.
17. Thomas Echelmeyer, Hinrich Wilhelm Meyer, Leo van Wüllen, "Novel ternary compoiste electrolytes: Li ion conducting in silica glass." *Chemistry of Materials*. **21** (2009) 2280-2285.
18. Marie-Alexandra Ne´ouze, Jean Le Bideau, Philippe Gaveau, Se´verine Bellayer, Andre´ Vioux, "Ionogels, new materials arising from the confinement of ionic liquids within silica-derived networks." *Chemistry of Materials*. **18** (2006) 3931-3936.
19. Marie-Alexandra Ne´ouze, Jean Le Bideau, Fabrice Lerouxb, Andre´ Vioux "A route to heat resistant solid membranes with performances of liquid electrolytes." *Chemical Communications*. (2005) 1082-1084.
20. J. Le Bideau, P. Gaveau, S. Bellayer, M.-A. Ne´ouze, A. Vioux, "Effect of confinement on ionic liquids dynamics in monolithic silica ionogels: 1H NMR study." *Physical Chemistry Chemical Physics*. **9** (2007) 5419-5422.
21. Carole V. Cerclier, Jean-Marc Zanotti, Jean Le Bideau, "Ionogel based on bioplymer-silica interpenetrated networks:Dynamics of confined ionic liquids with lithium salt." *Physical Chemistry Chemical Physics.* **17** (2015) 29707-29713.

22. K. J. Rao, N. Baskaran, P. A. Ramakrishnan, B. G. Ravi, A. Karthikeyan, "Structural and Lithium ion transport studies in sol-gel prepared lithium silicophosphate glasses." *Chemistry of Materials* **10** (1998) 3109-3123.
23. P. Muralidharan, N. Satyanarayana, M. Venkateswarlu, "Structural, ac conductivity and electric modulus studies of lithium based quaternary silicate glasses synthesized by the sol-gel route." *Physics and Chemistry of Glasses*. **46** (2005) 293-301.
24. Munesh Rathore, Anshuman Dalvi, Anil Kumar, W. Ślubowska, J.L. Nowinski "Ionic Liquid Dispersed Li+ Ion Oxide Glasses and Glass-Ceramics: Assessment of Electrical Transport and Thermal Stability." *Solid State Ionics* **282** (2015) 76-81.
25. Ali Karout, Alain C. Pierre, "Silica Gelation Catalysis by Ionic Liquids." *Catalysis Communications* **10** (2009) 359-361.
26. Nerea Gil-González, T. Akyazi, E. Castaňoa, F. Benito-Lopez, Maria C. Morant-Miňana, "Elucidating the Role of the Ionic Liquids in the Actuation Behavior of Thermo-Responsive Ionogels." *Sensors and Actuators B: Chemical* 260 (2017) 380-387.
27. Jean Le Bideau, Lydie Viaub, André Vioux, "Ionogels, Ionic Liquid Based Hybrid Materials." *Chemical Society Reviews* 40 (2011) 907-925.
28. Rajinder Shivran, S. C. Sivasubramanian, Anshuman Dalvi. "Sol-gel Synthesized Ionic Liquid Incorporated Novel Glassy Ionic System", in "*Energy Storage and Conversion: Materials and Devices"* Ed: Ashok Kumar, Narosa Publications India (2017) 143-147.
29. Masayuki Yamane, Hiroshi Kawazoe, Atsuo Yasumori, Toshikazu Takahashi. "Preparation of Pb-Containing Glass by the Sol-Gel Process – Reduction of Pb Migration during Drying", *Journal of Non-Crystalline Solids* **99** (1988) 160-167.
30. Anthony L. B. Maçon, Manon Jacquemin, Samuel J. Page, Siwei Li, Sergio Bertazzo, Molly M. Stevens, John V. Hanna, Julian R. Jones, "Lithium-silicate sol-gel bioactive glass and the effect of lithium precursor on structure-property relationships", *Journal of Sol-Gel Science and Technology* **81** (2017) 84–94.

31. Maria Lucia Ruiz, Ileana Daniela Lick, Marta Isabel Ponzi, Enrique Rodríguez Castellón, Antonio Jiménez-López, Esther Natalia Ponzi, "Thermal decomposition of supported lithium nitrate catalysts". *Thermochimica Acta* **499** (2010) 21–26.

32. Kikuko Hayamizu, Yuichi Aihara, Hiroe Nakagawa, Toshiyuki Nukuda, William S. Price, "Ionic Conduction and Ion Diffusion in Binary Room-Temperature Ionic Liquids Composed of [EMIM][BF_4] and $LiBF_4$", *Journal of Physical Chemistry* ***B*** **108** (2004) 19527-19532.

33. Brian A. Rosen, Wei Zhu, Gaurav Kaul, Amin Salehi-Khojin, Richard I. Masel, "Water Enhancement of CO_2 Conversion on Silver in 1-Ethyl-3-Methylimidazolium Tetrafluoroborate", *Journal of the Electrochemical Society* **160** (2013) H138-H14.

34. Mara G. Freire, Catarina M. S. S. Neves, Isabel M. Marrucho, Joa˜o A. P. Coutinho, Ana M. Fernandes, "Hydrolysis of Tetrafluoroborate and Hexafluorophosphate Counter Ions in Imidazolium-Based Ionic Liquids", *Journal of Physical Chemistry* ***A*** **114** (2010) 3744–3749.

35. P. Raghunathan, S. C. Sivasubramanian, "Magnetic resonance lineshapes in powdered and amorphous systems", *Proceedings of the Indian Academy of Sciences (Chemical Science)* **96** (1986) 565-580.

36. P. Raghunathan, S. C. Sivasubramanian, "X-ray Diffraction, Electron Paramagnetic Resonance, and Electron Spin Echo Modulation Studies of the PbO-$PbCl_2$,-$CuCl_2$, Ternary Glass System", *Journal of Physical Chemistry*, **95** (1991) 6346-6351.

37. P. Raghunathan, S.C. Sivasubramanian, "Structural Characterization of Some Novel Ternary PbO-$PbCl_2$-$CuCl_2$ Glasses by X-Ray Pair Distribution Functions, Thermal Analysis and Electron Paramagnetic Resonance", *Journal of Non-Crystalline Solids* **136** (1991) 14-26.

38. Larry L Hench, Jon K West, "The Sol-Gel Process", *Chemical Review* **90** (1990) 33-72.

39. Abhishek Kumar Gupta, Manish Pratap Singh, Rajendra Kumar Singh, Suresh Chandra, "Low Density Ionogels Obtained by Rapid Gellification of Tetraethyl Orthosilane Assisted by Ionic Liquids", *Dalton Transactions* **41**(2012) 6263-6271.

40. S. Musić, N. Filipović-Vinceković, L. Sekovanić, "Precipitation Of Amorphous SiO_2 Particles and their Properties", *Brazilian Journal of Chemical Engineering* **28** (2011) 89 – 94.

41. S. A. Katsyuba, Zvereva E. E., Vidiš A., Dyson P. J., "Application of Density Functional Theory and Vibrational Spectroscopy toward the Rational Design of Ionic Liquids", *The Journal of Physical Chemistry A* **111** (2007) 352-370.

42. R. Bruckner., "Properties and structure of vitreous silica", *Journal of Non-Crystalline Solids*, **5** (1970) 123-175.

43. V. M. Fokin, M. L.F. Nascimento, E. D. Zanotto., "Correlation between maximum crystal growth rate and glass transition temperature of silicate glasses." *Journal of Non-Crystalline Solids* **351** (2005) 789–794.

44. A. K. Gupta, Y. L. Verma, R. K. Singh, S. Chandra., "Studies on an ionic liquid confined in silica nanopores: Change in T_g and evidence of organic-inorganic linkage at the pore wall surface", *Journal of Physical Chemistry C* **118** (2014) 1530−1539.

45. Hayri E. A., M. Greenblatt., "The preparation and ionic conductivity of sol-gels in the Li_2O-P_2O_5-SiO_2 system", *Journal of Non-crystalline Solids* **94** (1987) 387-401.

46. Prashant Dabas, K. Hariharan, "Influence of an Ionic Liquid on the Conduction Characteristics of Lithium Niobophosphate Glass", *AIP Conference Proceedings*. **1512** (2013) 584-585.

47. Akitoshi Hayashi, Masahiro Yoshizawa, C. Austen Angell, Fuminori Mizuno, Tsutomu Minami, Masahiro Tatsumisago, "High Conductivity of Superionic-Glass-in-Ionic-Liquid Solutions", *Electrochemical and Solid-State Letters* **6** (2003) E19-E22.

48. Akitoshi Hayashi, Hideki Morishima, Kiyoharu Tadanaga, Masahiro Tatsumisago, "Characterization of Solid Electrolytes Prepared from Ionic Glass and Ionic Liquid for All-Solid-State Lithium Batteries", *Solid State Ionics* **192** (2011) 126-129.

49. F. Wohde, R. Bhandary, J.M. Moldrickx, J. Sundermeyer, M. Schönhoff, B. Roling., "Li^+ ion transport in ionic liquid-based electrolytes and the influence of sulfonate-based zwitterion additives", *Solid State Ionics*. **284** (2016) 37-44

50. Justin B. Haskins; William R. Bennett; James J. Wu; Dionne M. Hernández; Oleg Borodin; Joshua D. Monk; Charles W. Bauschlicher, Jr.; John W. Lawson, "Computational and Experimental Investigation of Li-Doped Ionic Liquid Electrolytes: [pyr14][TFSI], [pyr13][FSI], and [EMIM][BF_4]", *J. Phys. Chem. B*, 118 (2014) 11295−11309.

51. M. Rathore; Dalvi A., "Effect of Conditional Glass Former Variation on Electrical Transport in Li_2O–P_2O_5 Glassy and Glass-Ceramic Ionic System." *Solid State Ionics* 263 (2014) 119-124.

52. R. Baskaran, S. Selvasekarapandian, N. Kuwata, J. Kawamura, T. Hattori., "Conductivity and thermal studies of blend polymer electrolytes based on PVAc-PMMA", *Solid State Ionics*. **177** (2006) 2679–2682.

53. C. Cramer, M. Buscher., "Complete conductivity spectra of fast ion conducting silver iodide/silver selenite glasses", *Solid State Ionics*. **105** (1998) 109–120.

54. A. Ghosh, Pan A., "Scaling of the conductivity spectra in ionic glasses: dependence on the structure", *Physical Review Letters*. **84** (2000) 2188-2190.

55. B. Roling, Happe A., Funke K., Ingram M., "Carrier concentrations and relaxation spectroscopy: new information from scaling properties of conductivity spectra in ionically conducting glasses", *Physical Review Letters* **78** (1997) 2160-2163.

56. G. Govindaraj, Mariappan C., "Synthesis, characterization and ion dynamic studies of NASICON type glasses", *Solid State Ionics.* **147** (2002) 49-59.

57. M. Ganguli and K. J. Rao., "Structural role of PbO in Li_2O-PbO-B_2O_3 glasses", *Journal of Solid State Chemistry* **145** (1999) 65-76.

58. J. O. Isard, "The mixed alkali effect in glass", *Journal of Non-Crystalline Solids* **1** (1969) 235-261.

59. Delbert D. Day, "Mixed alkali glasses - their properties and uses", *Journal of Non-Crystalline Solids* **21** (1976) 343-372.

60. Jan Swenson, Stefan Adams, "Mixed Alkali Effect in Glasses", *Physical Review Letters* **90** (2003) 155507-1-4.

61. B. Vessal, G. N. Greaves, P. T. Marten, A. V. Chadwick, R. Mole, S. Houde-Walter, "Cation micro-segregation and ionic mobility in mixed alkali glasses", *Nature* **356** (1992) 504-506.

62. Junko Habasaki, Kia L. Ngaib, "The mixed alkali effect in ionically conducting glasses revisited: A study by molecular dynamics simulation", *Physical Chemistry Chemical Physics* **9** (2007) 4673–4689.

63. E. R. Talaty, S. Raja, V. J. Storhaug, A. Dolle, W. R. Carper., "Raman and infrared spectra and ab initio calculations of $C_{2\text{-}4}$MIM imidazolium hexafluorophosphate ionic liquids", *Journal of Physical Chemistry B.* **108** (2004) 13177-13184.

64. M. Rathore; Dalvi A., "Electrical Transport In Li_2SO_4– Li_2O–P_2O_5 Ionic Glasses and Glass-Ceramic Composites: A Comparative Study." *Solid State Ionics* 239 (2013) 50-55.

65. Christopher P. Fredlake, Jacob M. Crosthwaite, Daniel G. Hert, Sudhir N. V. K. Aki, Joan F. Brennecke, "Thermophysical Properties of Imidazolium-Based Ionic Liquids", *Journal of Chemical and Engineering Data* **49** (2004) 954-964.

66. H. C. Chang, T. C. Hung, H. S. Wang, T. Y. Chen, "Local structures of ionic liquids in the presence of gold under high pressures" *AIP Advances* **3** (2013) 032147-1 – 032147-10.

67. Jaanus Kruusma, Arvo Tõnisoo, Rainer Pärna, Ergo Nõmmiste, Enn Lust, "In Situ X-ray Photoelectron Spectroscopic and Electrochemical Studies of the Bromide Anions Dissolved in 1-Ethyl-3-Methyl Imidazolium Tetrafluoroborate." *Nanomaterials* **9** (2019) 304 (1-27).

68. A. Sharma, H. Jain, A. C. Miller, "Surface modification of a silicate glass during XPS experiments" *Surface and Interface Analysis* **31** (2001) 369–374